Steven J. Lambert
Department of Meteorology
Ph.D. Thesis

Short Title

A STUDY OF PLANETARY WAVE ERRORS IN A SPECTRAL NWP MODEL

A STUDY OF PLANETARY WAVE ERRORS IN A SPECTRAL NUMERICAL WEATHER PREDICTION MODEL

by

Steven J. Lambert

A thesis submitted to the Faculty of Graduate Studies and Research in partial fulfilment of the requirements for the degree of Doctor of Philosophy.

Department of Meteorology
McGill University
Montréal, Canada

March, 1977

ABSTRACT

A series of fifteen 96 hour forecasts was made with a spectral primitive equations numerical weather prediction model to investigate errors in the planetary waves. The amplitudes and phases of the geopotential errors are studied as functions of zonal wavenumber, spherical harmonic coefficient, time, pressure height, and latitude.

The geographic and synoptic character of the planetary wave errors is also studied.

The major contributor to the short range (less than 48 hour) forecast error is identified as an external mode. The improvement in the forecasts of five cases, resulting from the removal of the external mode is shown.

The medium range forecast error (96 hours) is internal in character and strongly resembles the errors studied in the vertical resolution experiments of Nakamura (1976) and Desmarais (1977).

Based on the similarity of the errors, it is hypothesized that the major cause of planetary wave errors is an inadequate vertical structure of the waves.

RÉSUMÉ

Une série de quinze prévisions à échéance de 96 heures a été effectuée à l'aide d'un modèle spectral de prévision numérique du temps à équations générales afin d'étudier les erreurs dans les ondes planétaires. Les amplitudes et les phases des erreurs du géopotentiel sont analysées en tant que fonctions du nombre d'onde zonal, du coefficient d'harmonique sphérique, du temps, du niveau de pression ainsi que de la latitude.

Le caractère géographique et synoptique des erreurs dans les ondes planétaires est également étudié.

Le principal facteur qui contribue à l'erreur de prévision à courte échéance (moins de 48 heures) est un mode externe. L'amélioration relevée dans les prévisions de cinq cas, provenant de la suppression du mode externe est demontrée. L'erreur dans la prévision à moyenne échéance (96 heures) est interne quant au caractère et s'apparente fortement aux erreurs étudiées dans les expériences sur la résolution verticale de Nakamura (1976) et Desmarais (1977).

Si on se base sur la ressemblance des erreurs on peut déduire hypothétiquement que la principale cause d'erreurs dans les ondes planétaires provient d'une structure imparfaite des ondes dans la verticale.

ACKNOWLEDGEMENTS

I wish to thank Dr. P. E. Merilees, who not only supervised the research but also suggested the topic of this study.

I gratefully acknowledge the assistance of Dr. R. Daley, who provided the author with the model used for this thesis, and Mr. J. Henderson, who provided advice necessary for modification of the model's computer program.

The figures were expertly draughted by Mrs. Sandra Yip and the French version of the abstract was provided by Mr. J. Benmurgui.

Mr. J.-G. Desmarais graciously provided the author with some results of his vertical resolution experiments.

I especially wish to thank my wife, Joy, who typed the draft and final copies of the manuscript and who proof-read the thesis.

I wish to thank the people of Canada for their financial support while I was on Education Leave from the Atmospheric Environment Service of the Department of the Environment.

LIST OF FIGURES

		Page
1.1	The positions of a ridge for zonal wavenumbers one to four for a period of 40 days. From Eliasen (1958).	2
3.1	Graph of total error (15 cases) against zonal wavenumber for the 1000 mb height field at 50° N. Figures adjacent to each of the curves give the length of the forecast in hours.	18
3.2	Same as Figure (3.1) except for the 850 mb height field at 50° N.	18
3.3	Same as Figure (3.1) except for the 700 mb height field at 50° N.	19
3.4	Same as Figure (3.1) except for the 500 mb height field at 50° N.	19
3.5	Same as Figure (3.1) except for the 300 mb height field at 50° N.	20
3.6	Same as Figure (3.1) except for the 200 mb height field at 50° N.	20
3.7	Same as Figure (3.1) except for the 100 mb height field at 50° N.	21
3.8	The normalized error as a function of zonal wavenumber at 500 mb and 50° N for forecasts of 12, 24, and 36 hours.	23
3.9	The total persistence error as a function of wavenumber compared to the total forecast error for 36 hours at 500 mb and 40° N.	23
3.10	Same as Figure (3.1) except for the 500 mb height field at 40° N.	21
3.11	Same as Figure (3.1) except for the 500 mb height field at 60° N.	24
3.12	Same as Figure (3.1) except for the 500 mb height field at 70° N.	24
3.13	The 36 hour error phases (position of a ridge) at 50° N as a function of pressure height for zonal wavenumber one. Small figures at the top of each profile refer to the case number given in Table (2.1).	26
3.14	Same as Figure (3.13) except for zonal wavenumber two.	27
3.15	Same as Figure (3.13) except for zonal wavenumber three.	28
3.16	Same as Figure (3.13) except for zonal wavenumber four.	29
3.17	Same as Figure (3.13) except for zonal wavenumber five.	30

Page

3.18 The 36 hour error phases at 500 mb as a function of latitude for zonal wavenumber one. Small figures at the top of each profile refer to the case number. 31

3.19 Same as Figure (3.18) except for zonal wavenumber two. 31

3.20 Same as Figure (3.18) except for zonal wavenumber three. 32

3.21 Same as Figure (3.18) except for zonal wavenumber four. 32

3.22 Same as Figure (3.18) except for zonal wavenumber five. 33

3.23 A comparison of the total 36 hour 500 mb error at 50° N and the 1000 mb to 500 mb total thickness error at 50° N as a function of zonal wavenumber. 34

3.24 The normalized error of the spherical harmonic coefficients of the 500 mb height field of zonal wavenumber one as a function of time. 37

3.25 Same as Figure (3.24) except for zonal wavenumber two. 37

3.26 Same as Figure (3.24) except for zonal wavenumber three. 38

3.27 Same as Figure (3.24) except for zonal wavenumber four. 38

3.28 Same as Figure (3.24) except for zonal wavenumber five. 39

3.29 Same as Figure (3.24) except for zonal wavenumber six. 39

3.30 Same as Figure (3.24) except for zonal wavenumber seven. 40

3.31 Same as Figure (3.24) except for zonal wavenumber eight. 40

4.1 The 36 hour systematic planetary wave error at 1000 mb displayed on a map with unequal latitude and longitude spacing. 43

4.2 Same as Figure (4.1) except for the 500 mb height field. 44

4.3 Same as Figure (4.1) except for the 1000 mb to 500 mb thickness field. 45

4.4 The 36 hour planetary wave error at 500 mb superimposed on the verifying 500 mb analysis. 47

4.5 A comparison of the long wave error at 500 mb and 40° N between the control and the surface pressure substitution forecasts. 50

Page

4.6 Same as Figure (4.5) except for the 1000 mb to 500 mb thickness at 40° N. 50

4.7 The initial 500 mb analysis for Case 5. 51

4.8 The 36 hour 500 mb verifying analysis for Case 5. 52

4.9 The 36 hour unaltered forecast 500 mb chart for Case 5. 53

4.10 The 36 hour forecast 500 mb chart for Case 5 with surface pressure substitution. 54

5.1 A simple schematic harmonic dial. 56

5.2 A complex schematic harmonic dial of three transient waves with periods in a ratio of 1:-2:8 and amplitudes in a ratio of 1:2:5 respectively. 57

5.3 Harmonic dial of a typical forecast of spherical harmonic coefficient (1,1) of the 500 mb height field together with the verifying observations. Figures adjacent to the dots and crosses are the time in hours from the initial time. 59

5.4 Same as Figure (5.3) except for coefficient (2,2). 59

5.5 Same as Figure (5.3) except for coefficient (2,4). 60

5.6 Same as Figure (5.3) except for coefficient (3,3). 60

5.7 Same as Figure (5.3) except for coefficient (4,4). 61

5.8 High time resolution harmonic dial of Figure (5.3). Small dots are placed at intervals of 80 minutes. Figures adjacent to the large dots give the time in hours from the initial time. 62

5.9 The latitudinal structure of the three external modes of wavenumber one for Case 3 at 500 mb. The abscissa is labelled in degrees of latitude. 65

5.10 The vertical structure of the external Rossby mode. 66

5.11 Eigenfrequencies of the three lowest order symmetric free modes of Laplace's Tidal Equations for wavenumber one. The order of the modes increases with increasing (n-s). From Longuet-Higgins (1968). 69

Page

5.12 Same as Figure (5.11) except for zonal wavenumber three. 70

5.13 Latitudinal structure of the 36 hour and 96 hour total error for wavenumber one at 1000 mb. 73

5.14 The latitudinal structure of the 96 hour error phases for wavenumber one at 1000 mb. Figures above or below the profiles are the case numbers. 74

5.15 Vertical structure of the 36 hour and 96 hour error amplitudes for wavenumber one at 70° N. 75

5.16 Vertical structure of the 96 hour error phases for wavenumber one at 70° N. Figures above each profile are the case numbers. 76

5.17 A comparison between the observed and forecast stationary components of spherical harmonic coefficient (2,4) of the height fields of Case 3. 78

5.18 The behavior of the forecast transient component of spherical harmonic coefficient (1,1) of the 500 mb height field of Case 3. 79

5.19 High resolution structure (solid lines) of a forced planetary wave compared to the low resolution structure (dashed lines). From Nakamura (1976). 81

5.20 Evolution of a low vertical resolution model (dashed lines) supplied with the steady state solution (solid lines) of the corresponding high resolution or control model. From Nakamura (1976). 82

5.21 The 96 hour wavenumber one error structure from Desmarais' time-dependent vertical resolution experiments. The error amplitudes are in solid lines and the error phases in dash lines. 83

5.22 The seasonal dependence of the amplitudes of the 36 hour forecast error at 500 mb. 84

5.23 Mean summer and winter wind profiles with height. Heights are given in km. 86

LIST OF TABLES

		Page
1.1	Harmonic analysis of mean charts. Amplitudes are in geopotential meters and phases in degrees of longitude. From Eliasen (1958).	3
2.1	The initial time of each of the fifteen cases.	13
5.1	Approximate periods of the transient components of the spherical harmonic coefficients forecast with large error.	58
5.2	The periods and directions of propagation of the forecast transient components of spherical harmonic coefficients (1,1) and (2,2) of the 500 mb height field.	63

TABLE OF CONTENTS

		Page
ABSTRACT		ii
RÉSUMÉ		iii
ACKNOWLEDGEMENTS		iv
LIST OF FIGURES		v
LIST OF TABLES		ix
TABLE OF CONTENTS		x
CHAPTER		
1	INTRODUCTION	1
1.1	The Observed Structure of the Large Scale Waves	1
1.2	The Large Scale Waves and Numerical Models	5
1.3	The Scope of the Present Study	6
2	DESCRIPTION OF THE MODEL AND THE EXPERIMENTS	8
2.1	Introduction	8
2.2	The Model	8
2.3	The Experiments	12
3	THE SPECTRAL DISTRIBUTION OF THE ERRORS	15
3.1	Introduction	15
3.2	The Definition of Errors in the Zonal Waves	15
3.3	Results for the Zonal Waves	17

		Page
3.4	Definition of the Errors in the Spherical Harmonic Coefficients	25
3.5	Error Results for the Spherical Harmonic Coefficients	35
3.6	Summary	36
4	THE GEOGRAPHIC AND SYNOPTIC CHARACTER OF THE PLANETARY WAVE ERRORS	41
4.1	Introduction	41
4.2	Geographical Distribution of the Average Error	41
4.3	Synoptic Depiction of the Individual Case Errors	46
4.4	The Surface Pressure Substitution Experiments	46
4.5	Results of the Pressure Substitution	48
4.6	Summary	49
5	A DETAILED EXAMINATION OF THE PLANETARY WAVE ERRORS	55
5.1	Introduction	55
5.2	Errors in the Spherical Harmonic Coefficients of Low Meridional Wavenumber	58
5.3	Laplace's Tidal Equations	66
5.4	The Specific Nature of the External Modes	68
5.5	The Nature of the Medium Range Forecast Error	72
5.6	Behavior of the Forecast Stationary and Transient Components of the Planetary Waves	77
5.7	Vertical Resolution and the Planetary Waves	79
5.8	Seasonal Variation of the Planetary Wave Errors	82
5.9	Conclusions	85
6	SUMMARY AND CONCLUSIONS	88
6.1	Contributions to Knowledge	88

Page

6.2 Summary of the Error Character 88

6.3 Suggestions for Further Work 90

BIBLIOGRAPHY 91

CHAPTER 1

INTRODUCTION

1.1 The Observed Structure of the Large Scale Waves

The examination of mid-tropospheric analyses of geopotential height, time-averaged over one month periods, shows the existence of quasi-stationary waves of large horizontal scale. A study by Eliasen (1958) gave a harmonic analysis of average monthly 500 mb and 1000 mb charts as well as a daily harmonic analysis of a forty day series of data. Figure (1.1) gives the daily positions of a ridge for wavenumbers one to four during the period October 21, 1950, to November 30, 1950.

It can be seen that, in general, the large scale waves consist of a relatively large stationary component and smaller transient components. Studies by Charney and Eliassen (1949) and Smagorinsky (1953) indicate that the stationary part of the large scale waves is due to forcing by the earth's topography and land-sea temperature contrasts. Table (1.1) from Eliasen (1958) gives the amplitudes and phases (positions of a ridge) of the stationary components of wavenumbers one to three obtained from the average monthly analyses of January and July at 1000 mb and 500 mb.

Eliasen's study also showed that wavenumbers one to four were quasi-stationary, that wavenumbers greater than or equal to six showed a

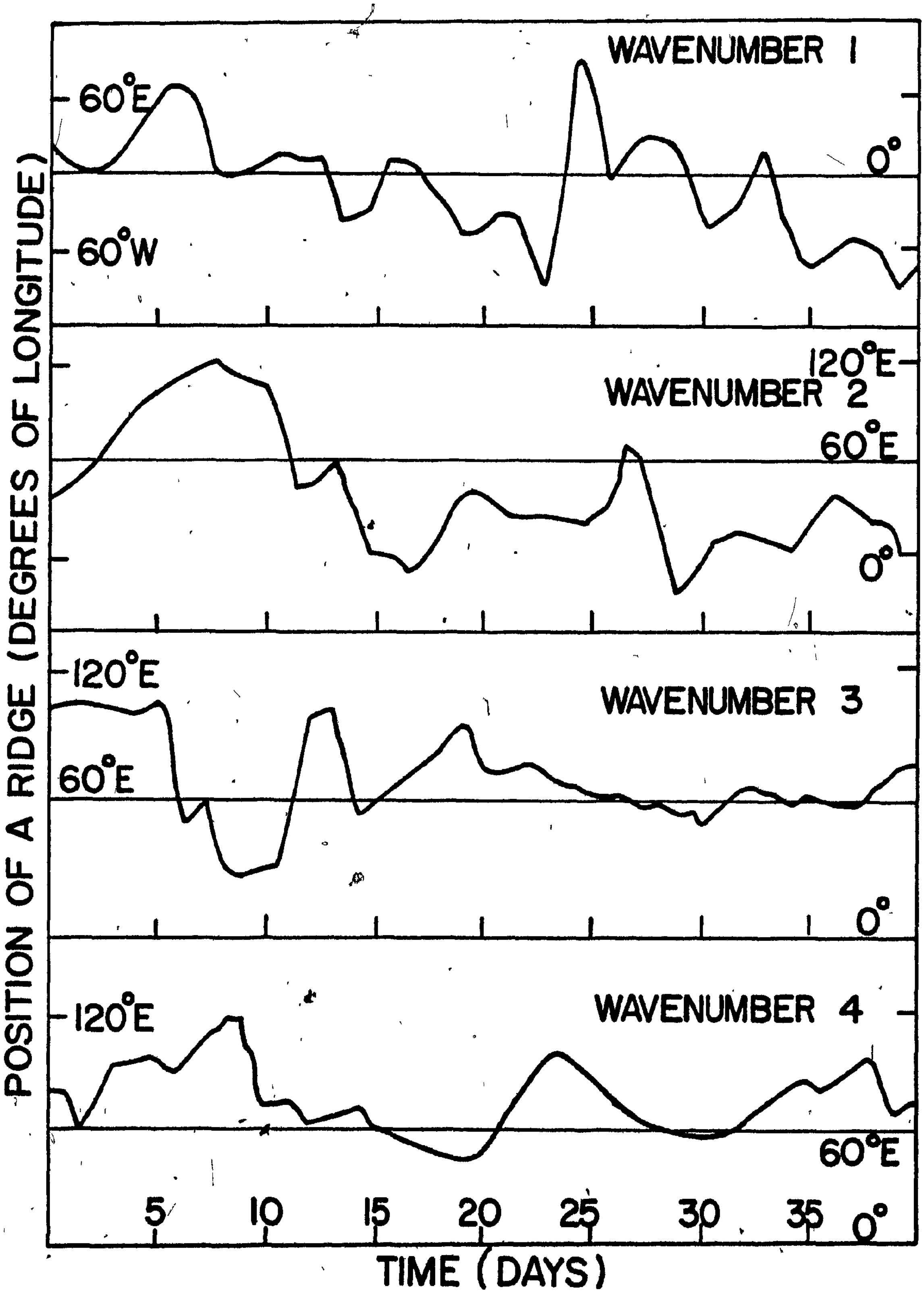

FIGURE (1.1) The positions of a ridge for zonal wavenumbers one to four for a period of 40 days. From Eliasen (1958).

Lat.	Zonal Wave-number	January				July			
		500 mb		1000 mb		500 mb		1000 mb	
		Amp.	Phase	Amp.	Phase	Amp.	Phase	Amp.	Phase
30° N	1	59	-68	16	351	41	-48	79	-104
	2	10	145	16	110	16	175	53	165
	3	28	83	17	102	4	17	21	77
40° N	1	84	-34	39	46	38	-28	66	-98
	2	34	42	48	89	12	77	48	179
	3	64	98	32	108	12	79	22	83
50° N	1	84	6	76	66	32	22	38	-89
	2	79	43	83	85	43	73	32	14
	3	80	106	33	2	22	111	12	93
60° N	1	62	40	71	114	35	73	17	-101
	2	100	33	64	79	42	58	19	30
	3	63	108	43	12	24	114	6	104
70° N	1	50	84	87	163	39	116	3	-86
	2	98	21	19	71	40	40	12	23
	3	40	108	18	3	14	101	2	110

TABLE (1.1) Harmonic analysis of mean charts. Amplitudes are in geopotential meters and phases are in degrees of longitude. From Eliasen (1958).

general eastward motion and that wavenumber five, while generally transient, showed a preference for certain positions of its ridges.

Subsequent studies of the properties of the large scale waves have concentrated on the transient components. In a study of January 1957 500 mb data, Eliasen and Machenhauer (1965) observed that the transient components of the large scale waves propagated westward with periods as short as a few days. Deland and Johnson (1968) showed that westward moving transient components of the large scale waves were present throughout the year. These authors also examined the vertical structure of the winter transient components and observed a general increase in amplitude with height and a weak westward tilt of the phases with height.

The rate of error growth in the various horizontal scales has been investigated by predictability experiments. These experiments usually consist of performing a forecast with a model and comparing these results to those obtained when the forecast is repeated with slightly different initial conditions. The differing initial conditions represent an error and the subsequent difference between the two forecasts represents the error resulting from the incorrectly specified initial conditions. The time taken for this error to reach some predetermined level, which can be compared for the various scales of motion, is a measure of predictability. Lorenz (1969), using a simple one-level model of incompressible unbounded flow, and Smagorinsky (1969), using a complex nine level hemispheric general circulation model, showed that the largest scale waves have the highest predictability and that the rate of error growth increases with decreasing scale of motion. This result, together with the quasi-stationary character of the large scale waves, suggests that forecasts of these scales of motion should meet with considerable success. Curiously, such is not the case.

1.2 The Large Scale Waves and Numerical Models

Almost from the beginning of numerical weather prediction, the large scale waves have been a problem for atmospheric models. As soon as hemispheric forecasts with simple one-level barotropic models began, it was observed (Wolff (1958)) that the large scale waves retrogressed (moved westward) with approximately the Rossby-Haurwitz (Haurwitz (1940)) phase speed. Since this rapid retrogression was in violation of observed atmospheric behavior, it was controlled by holding the large scale waves stationary during a forecast or by using the "long-wave stabilization" term derived by Cressman (1958).

The systematic error in large scale wave forecasts with a one-level hemispheric barotropic model with topography was determined by Martin (1958). His results showed that a strong geographical bias existed, causing the 500 mb geopotential heights to be forecast too high off the east coast of Asia and too low in the mid-Atlantic. Fourier analysis showed that the model's systematic errors were caused by incorrect forecasts of wavenumbers one to four.

Investigations of large scale wave forecast errors in more advanced numerical weather prediction models were slow to appear in the literature. Most verification of such models is performed synoptically or by computing skill scores or root mean square errors and usually no attempt is made to assign forecast error to the various horizontal scales. The quality of forecasts made with advanced models was steadily improving and visual inspection of forecast weather maps showed that the major quasi-stationary trough and ridge patterns were generally correctly forecast in position. These facts could lead one to believe that significant large scale wave errors no longer existed in advanced numerical weather prediction models.

However, it soon became apparent that the problem of large scale wave errors still existed and studies were undertaken in an attempt to find their causes. Miyakoda et al. (1971) observed that the waves in the westerlies were forecast with insufficient amplitudes and that cut-off lows were seldom produced. In this paper, the authors studied the effects of horizontal resolution on forecasts of the large scale waves. Their results showed that these waves were not satisfactorily forecast; and, while increased horizontal resolution improved forecasts of the order of ten days, it did not improve 36 to 48 hour forecasts of large scale waves.

Further evidence of large scale wave errors came from Leith (1974). In a series of 36 hour forecasts at 500 mb with a spectral one-level barotropic model, the error was computed as a function of wavenumber. These experiments showed that the smallest error was present at wavenumber six and that the error increased in the shorter and longer waves.

1.3 The Scope of the Present Study

The aim of this thesis is to investigate forecast errors in the planetary waves and is an extension to a baroclinic model of Leith's barotropic study. The collective term planetary waves will henceforth refer to zonal wavenumbers one to five since these waves possess both a quasi-stationary nature and a large horizontal scale; and, the collective term long waves will refer to wavenumbers one to eight. Chapter 2 will describe the experimental procedure and the errors will be documented in Chapter 3. Chapter 4 will give the geographical and synoptic character of the planetary wave errors. The detailed nature of these errors will be presented in Chapter 5 along with a hypothesis of their cause and suggestions of methods of their elimination.

CHAPTER 2

DESCRIPTION OF THE MODEL AND THE EXPERIMENTS

2.1 Introduction

For investigation of forecast errors in terms of wavenumber, it is very convenient to employ a spectral model. An advanced global baroclinic primitive equation spectral model developed at the Division de Recherche en Prévision Numérique of the Atmospheric Environment Service was made available to the author.

2.2 The Model

The model used for this study was that of Daley et al. (1976) with minor modifications. The model uses sigma (σ) co-ordinates (Phillips (1957)) and has five levels equally spaced in σ. The model's horizontal spectral representation possesses a rhomboidal truncation (Ellsaesser (1966)) and finite-differencing is used in the vertical.

The governing equations are

$$\frac{\partial Q}{\partial t} = -\nabla\cdot(Q+f)\vec{V} - \vec{k}\cdot\nabla\times\left(RT\nabla q + \dot{\sigma}\frac{\partial \vec{V}}{\partial \sigma} - F\right), \qquad 2.1$$

$$\frac{\partial D}{\partial t} = \vec{k}\cdot\nabla\times(Q+f)\vec{V} - \nabla\cdot\left(RT\nabla q + \dot{\sigma}\frac{\partial \vec{V}}{\partial \sigma} - F\right) - \nabla^2\left(\Phi + \frac{1}{2}\vec{V}\cdot\vec{V}\right), \qquad 2.2$$

$$\frac{\partial T}{\partial t} = -\nabla\cdot\vec{V}T + TD + \dot{\sigma}\gamma - \frac{RT}{C_p}\left(D + \frac{\partial\dot{\sigma}}{\partial\sigma}\right) + H_T, \qquad 2.3$$

$$\frac{\partial q}{\partial t} = -\overline{D} - \overline{\vec{V}}\cdot\nabla q, \qquad 2.4$$

$$\sigma\frac{\partial\Phi}{\partial\sigma} = -RT, \qquad 2.5$$

where f = Coriolis parameter,

Q = vertical component of vorticity,

$\vec{V}$ = horizontal wind vector,

D = horizontal divergence,

T = temperature,

q = natural logarithm of the surface pressure,

γ = static stability $\left(\frac{RT}{\sigma C_p} - \frac{\partial T}{\partial\sigma}\right)$

$\dot{\sigma}$ = vertical velocity in sigma co-ordinates,

$= (\sigma-1)(\overline{D} + \overline{\vec{V}}\cdot\nabla q) + \overline{D}^{\sigma} + \overline{\vec{V}}^{\sigma}\cdot\nabla q$

Φ = geopotential height,

F = horizontal friction force per unit mass,

H_T = diabatic heating,

R = gas constant for dry air,

C_p = specific heat for dry air at constant pressure,

and

$$(\overline{\quad}) = \int_0^1 (\quad)\, d\sigma, \qquad 2.6$$

$$\overline{(\ )}^{\sigma} = \int_{\sigma}^{1} (\ )\, d\sigma \quad . \qquad 2.7$$

Global and hemispheric forecasts can be made with the model. When the model is used hemispherically, the following quantities, D , Φ , T , q , and the zonal component of the wind are required to be symmetric about the equator; and, the quantities Q and the meridional component of the wind are anti-symmetric about the equator in order to be consistent with the governing equations (2.1) to (2.5).

The semi-implicit method of Robert et al. (1972), which is incorporated in the model, allows relatively long time steps to be used. To control numerical instability introduced by the dissipative terms in the boundary layer parameterization a weak time filter (Robert (1966)) is needed.

The version of the model used does not incorporate radiation or moisture calculations but does include the effects of topography, heating from warm oceans, surface friction, and dry convective adjustment.

The data input to the model is the temperature, geopotential, and streamfunction field defined on a 2805 point polar stereographic grid with a grid spacing of 381 km at 60° N on seven standard pressure levels 1000 mb, 850 mb, 700 mb, 500 mb, 300 mb, 200 mb, and 100 mb. The streamfunctions were obtained from the geopotentials by solution of the balance equation

$$\nabla^2\left[\Phi + \frac{1}{2}(\nabla\psi)^2\right] = \nabla\cdot\left[(f+\nabla^2\psi)\nabla\psi\right], \qquad 2.8$$

where f = Coriolis parameter,
ψ = streamfunction,
Φ = geopotential.

There are a number of transformations of the data required before it is in a form suitable for integration. First, they are bi-cubically interpolated on each of the seven pressure levels from the polar stereographic grid to a transform grid (Orszag (1970)) which consists of equally spaced longitudes and almost equally spaced Gaussian latitudes. This procedure requires extrapolation south of 15° N to the equator. The symmetric fields have the average around the latitude circle at 15° N extended to the equator and the departure from this average at a given longitude decays linearily to zero at the equator. For the anti-symmetric fields, both the 15° N zonal average and the departure decay linearily to zero at the equator. Second, the data are vertically interpolated, using the surface topography, from the transform grids on the pressure surfaces to the transform grids on the sigma surfaces and finally, they are spectrally analyzed for use by the model. After a forecast has been completed, a reverse procedure yields the forecast spectral coefficients on the seven constant pressure surfaces.

The spectral representation in the model is in terms of spherical harmonics of the form

$$Y_n^m = P_n^m(\sin\phi)e^{im\lambda}, \qquad 2.9$$

where Y_n^m = spherical harmonic,
P_n^m = associated Legendre function of the first kind,

ϕ = latitude,

λ = longitude,

m = zonal wavenumber,

$n-m$ = meridional wavenumber.

A given field χ is represented by a truncated series consisting of a linear combination of spherical harmonics

$$\chi(\phi,\lambda) = \sum_{m=-R}^{R}\ \sum_{n=|m|}^{|m|+R} \chi(m,n)\, Y_n^m(\phi,\lambda),$$

where R = rhomboidal resolution,

$\chi(m,n)$ = spherical harmonic coefficient.

In this study, a given spherical harmonic coefficient $\chi(m,n)$, of the variable χ, will be referred to as the coefficient (m, n) of the field χ.

The spherical harmonic coefficients of the symmetric fields (D, Φ, T, q, and the zonal component of the wind) will be non-zero only if (m-n) is even and the coefficients of the anti-symmetric (Q and the meridional component of the wind) fields will be non-zero only if (n-m) is odd.

2.3 The Experiments

A series of fifteen 96 hour hemispheric forecasts was made using the model described above. The model was used with a 20 wave resolution and a 40 minute time step. The output consisted of the spherical harmonic coefficients of the geopotential at intervals of 12 hours for each of the seven pressure surfaces. Of the fifteen cases, six were summer, i.e. between the vernal and autumnal equinoxes, and the remaining half year contained nine winter cases. The dates were chosen randomly with the restriction that each month must contain at least one case. Table (2.1) gives the initial times of each of the fifteen cases.

CASE	INITIAL TIME	
1	Dec. 31, 1974	00 GMT
2	Jan. 16, 1974	00 GMT
3	Jan. 21, 1975	12 GMT
4	Feb. 11, 1975	00 GMT
5	Mar. 1, 1975	00 GMT
6	Oct. 19, 1974	12 GMT
7	Nov. 21, 1974	12 GMT
8	Dec. 13, 1974	00 GMT
9	Mar. 14, 1975	00 GMT
10	Apr. 7, 1974	12 GMT
11	Aug. 25, 1974	12 GMT
12	June 11, 1974	00 GMT
13	May 18, 1974	12 GMT
14	July 4, 1974	12 GMT
15	Sep. 11, 1974	00 GMT

TABLE (2.1) The initial time of each of the fifteen cases.

The analyses used to verify each twelve hour period of the forecasts were available only as grid point values on the 2805 point polar stereographic grid. To obtain the required verifying spherical harmonic coefficients of the geopotentials, the model was initialized using the verifying analyses, a forecast of zero time length was made, and the coefficients of the geopotentials were produced for the seven pressure levels.

CHAPTER 3

THE SPECTRAL DISTRIBUTION OF THE LONG WAVE ERRORS

3.1 Introduction

In this chapter, detailed statistics of the errors produced by the experiments of the previous chapter will be presented. The spectral errors in both the geopotential height and thickness (vertically averaged temperature) will be given as functions of time, pressure height, and latitude. In addition to documenting the errors in each zonal wavenumber, the error statistics for the spherical harmonic coefficients will be given.

3.2 The Definition of the Errors in the Zonal Waves

A field obtained from observation can be written as

$$\Phi_o = \sum \sum \Phi_o(m,n)\, P_n^m e^{im\lambda}.$$

Similarly, a forecast field Φ_f , can be written

$$\Phi_f = \sum \sum \Phi_f(m,n)\, P_n^m e^{im\lambda}.$$

The difference between these two yields the forecast error field Φ_e i.e. $\Phi_e = \Phi_o - \Phi_f$

$$= \sum \sum \Phi_o(m,n)\, P_n^m e^{im\lambda} - \sum \sum \Phi_f(m,n)\, P_n^m e^{im\lambda},$$

$$= \sum \sum \left(\Phi_o(m,n) - \Phi_f(m,n) \right) P_n^m e^{im\lambda}.$$

With the definition $\Phi_e(m,n) = \Phi_o(m,n) - \Phi_f(m,n)$, the expression for the error field becomes

$$\Phi_e = \sum \sum \Phi_e(m,n) P_n^m e^{im\lambda}. \qquad (3.1)$$

The contribution of a given zonal wave "m" to the error field is

$$\Phi_e(m) = \sum \Phi_e(m,n) P_n^m e^{im\lambda} + \sum \Phi_e(-m,n) P_n^{-m} e^{-im\lambda}.$$

Using the relations

$$P_n^{-m} = (-1)^m P_n^m ,$$

and

$$\Phi_e(-m,n) = (-1)^m \overset{*}{\Phi}_e(m,n),$$

where $\overset{*}{\Phi}_e(m,n)$ is the complex conjugate of $\Phi_e(m,n)$. $\Phi_e(m)$ can be written in the form

$$\Phi_e(m) = A_e(m) \cos\left\{ m(\lambda - \delta_e(m)) \right\},$$

where

$$A_e(m) = 2\left[\left(\sum_{n=|m|}^{|m|+R} \mathrm{Re}\left\{ \Phi_e(m,n) \right\} P_n^m \right)^2 + \left(\sum_{n=|m|}^{|m|+R} \mathrm{Im}\left\{ \Phi_e(m,n) \right\} P_n^m \right)^2 \right]^{\frac{1}{2}},$$

$$\delta_e(m) = \frac{1}{m}\tan^{-1}\frac{-\sum \mathrm{Im}\{\Phi_e(m,n)\}P_n^m}{\sum \mathrm{Re}\{\Phi_e(m,n)\}P_n^m} .$$

The quantity $A_e(m)$ will be referred to as the error or error amplitude and the quantity $\delta_e(m)$ as the error phase. The sum of the $A_e(m)$'s for the fifteen cases will be referred to as the total zonal wave error.

3.3 Results for the Zonal Waves

Figures (3.1) to (3.7) give the total zonal wave error of the height field expressed in geopotential meters (gpm) as a function of time for seven pressure levels from 1000 mb to 100 mb at 50° N. An examination of the figures shows that the waves of smallest wavenumber have the largest total error at all pressure levels and at all times. Turning our attention to the character of the planetary wave errors, we can see, apart from the fact that they increase with height, that the errors possess very little vertical structure during the first 36 hours. On the average, the errors grow in time but not in a uniform manner.

At 96 hours, the planetary wave errors possess a noticeable vertical structure. In general, wavenumber one is most poorly forecast except at mid-tropospheric levels where wavenumbers two and three are dominant. Also, very noticeable on the 96 hour curves is the emergence of large errors in wavenumber five which has only a weak vertical structure.

Up to this point, only the absolute errors have been presented. Figure (3.8) gives the average error (total error divided by the number of

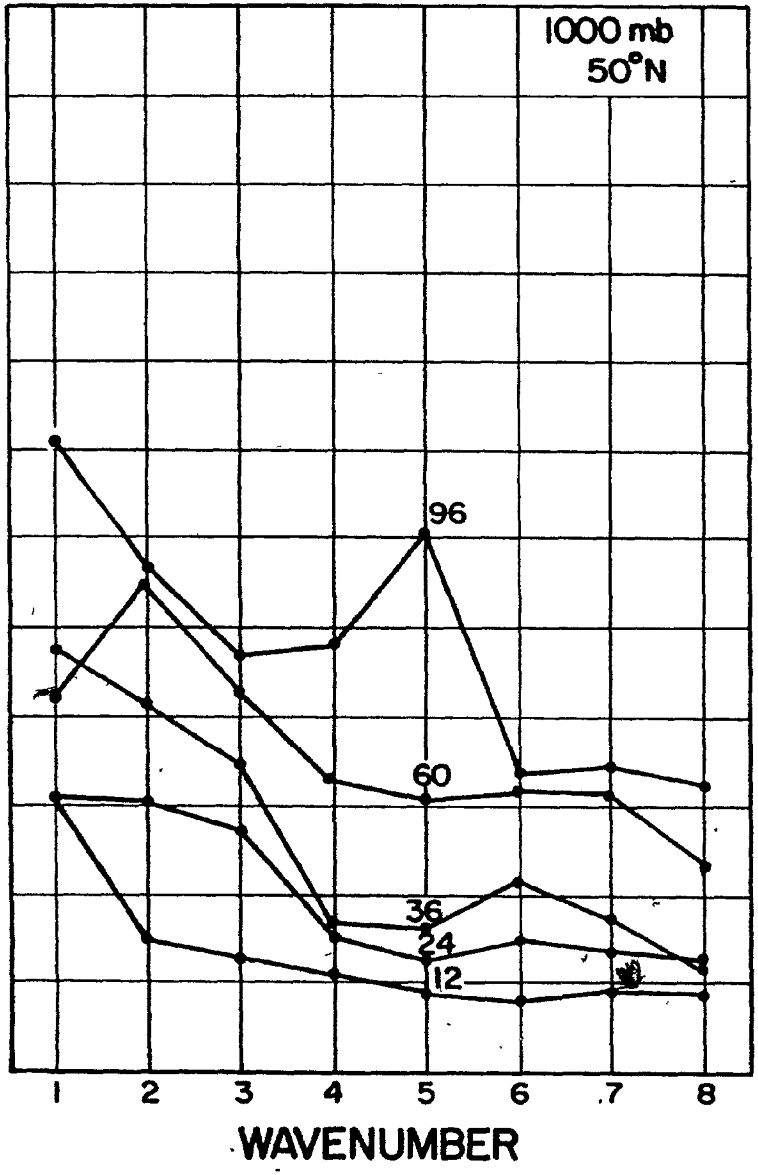

FIGURE (3.1) Graph of total error (15 cases) against wavenumber for the 1000 mb height field at 50° N. Figures adjacent to each of the curves give forecast length in hours.

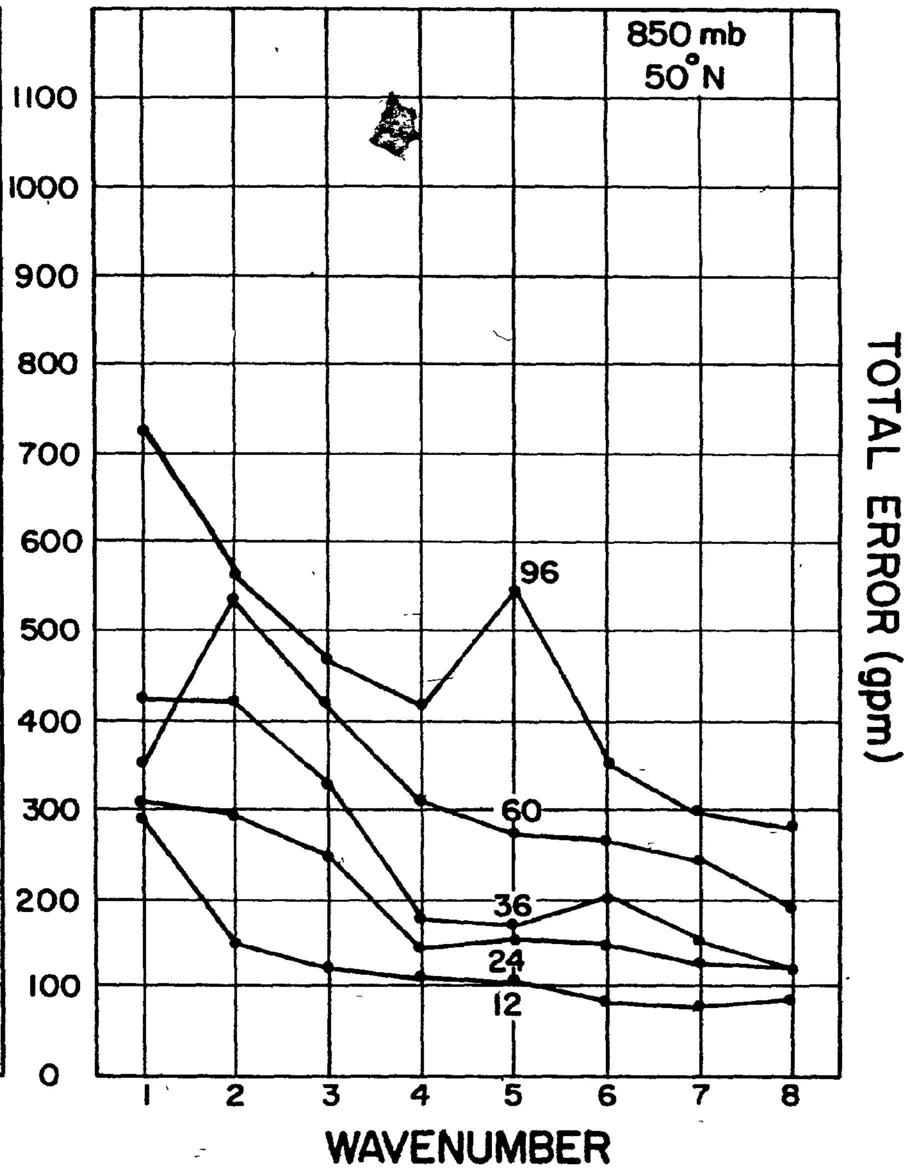

FIGURE (3.2) Same as Figure (3.1) except for the 850 mb height field at 50° N.

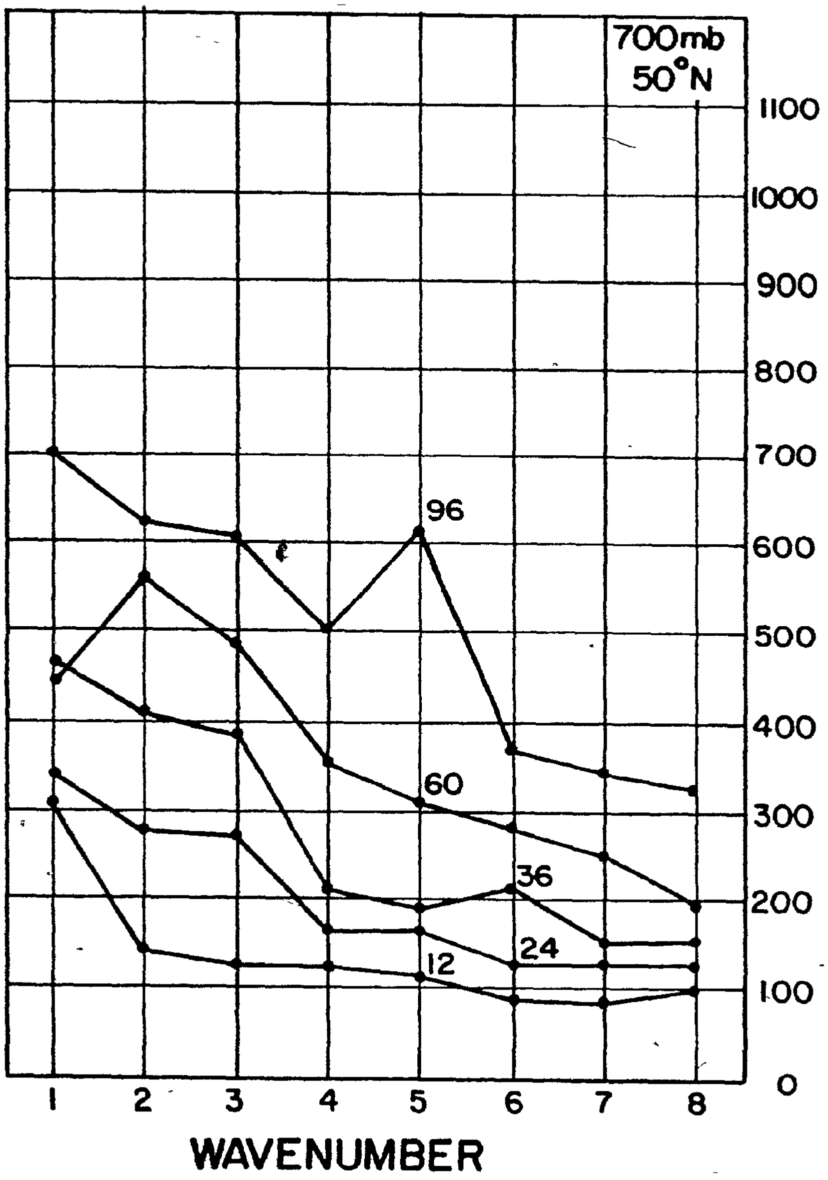

FIGURE (3.3) Same as Figure (3.1) except for the 700 mb height field at 50° N.

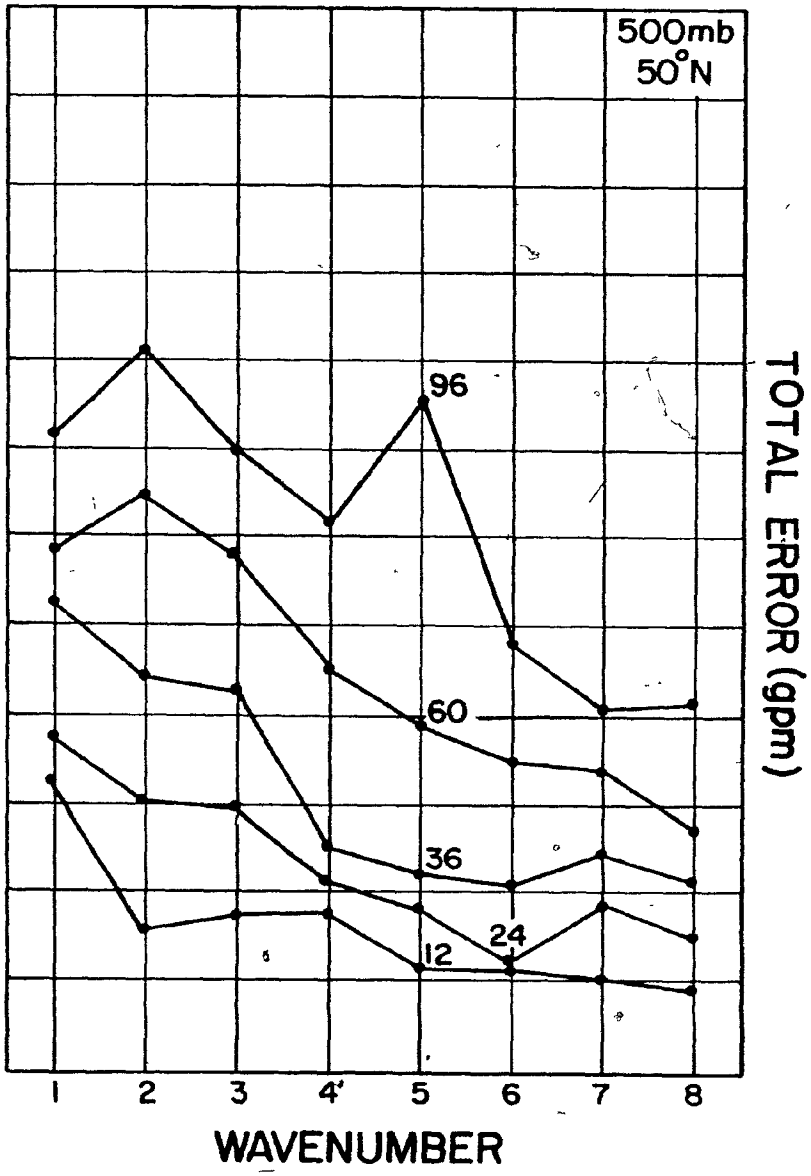

FIGURE (3.4) Same as Figure (3.1) except for the 500 mb height field at 50° N.

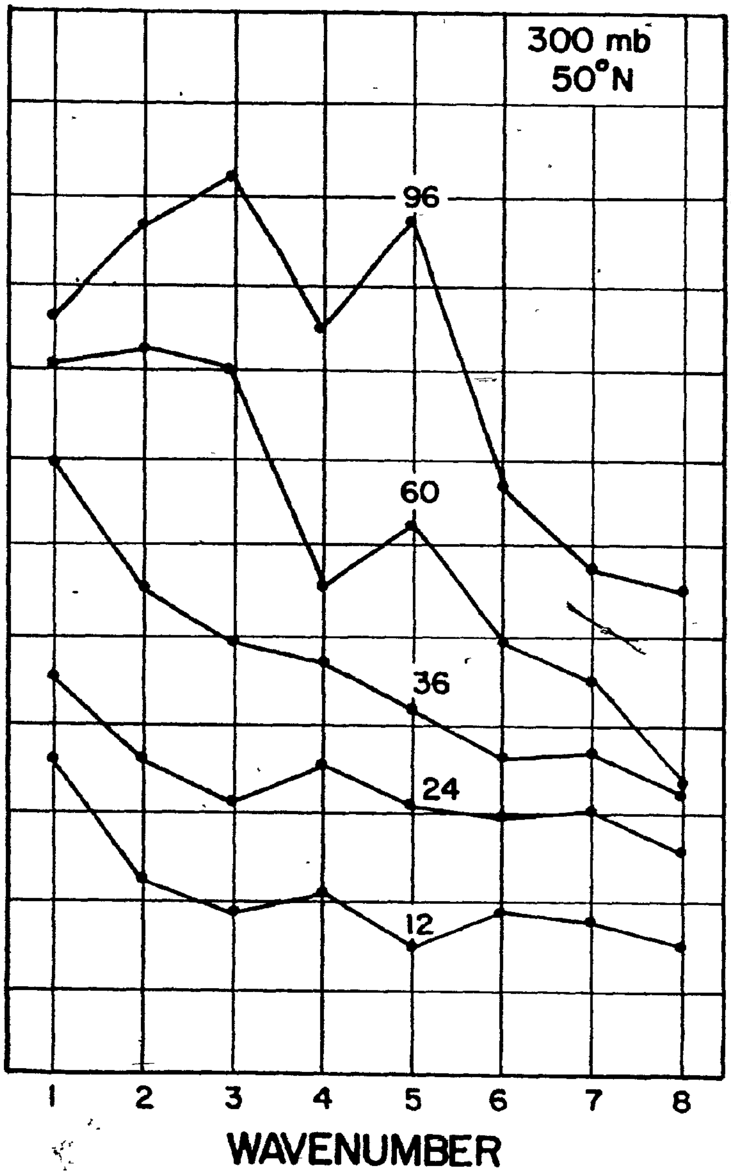

FIGURE (3.5) Same as Figure (3.1) except for the 300 mb height field at 50° N.

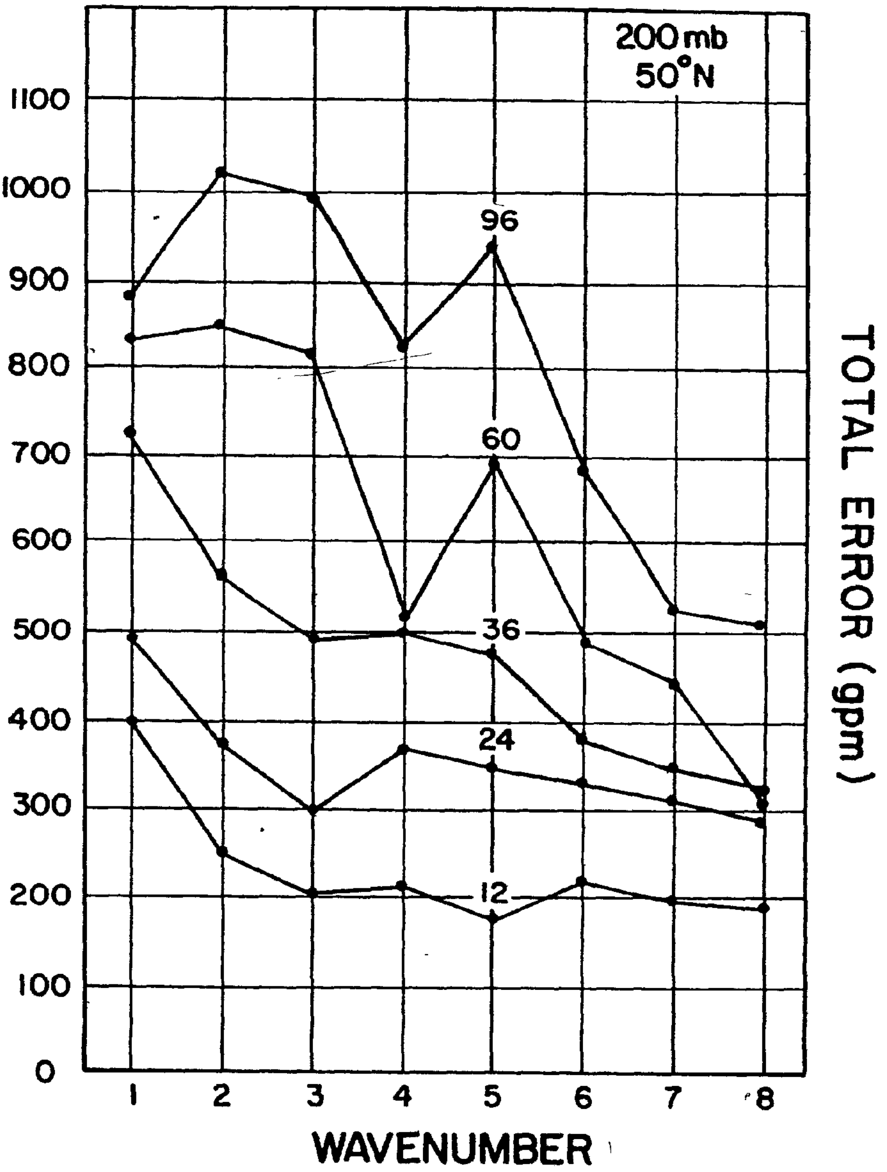

FIGURE (3.6) Same as Figure (3.1) except for the 200 mb height field at 50° N.

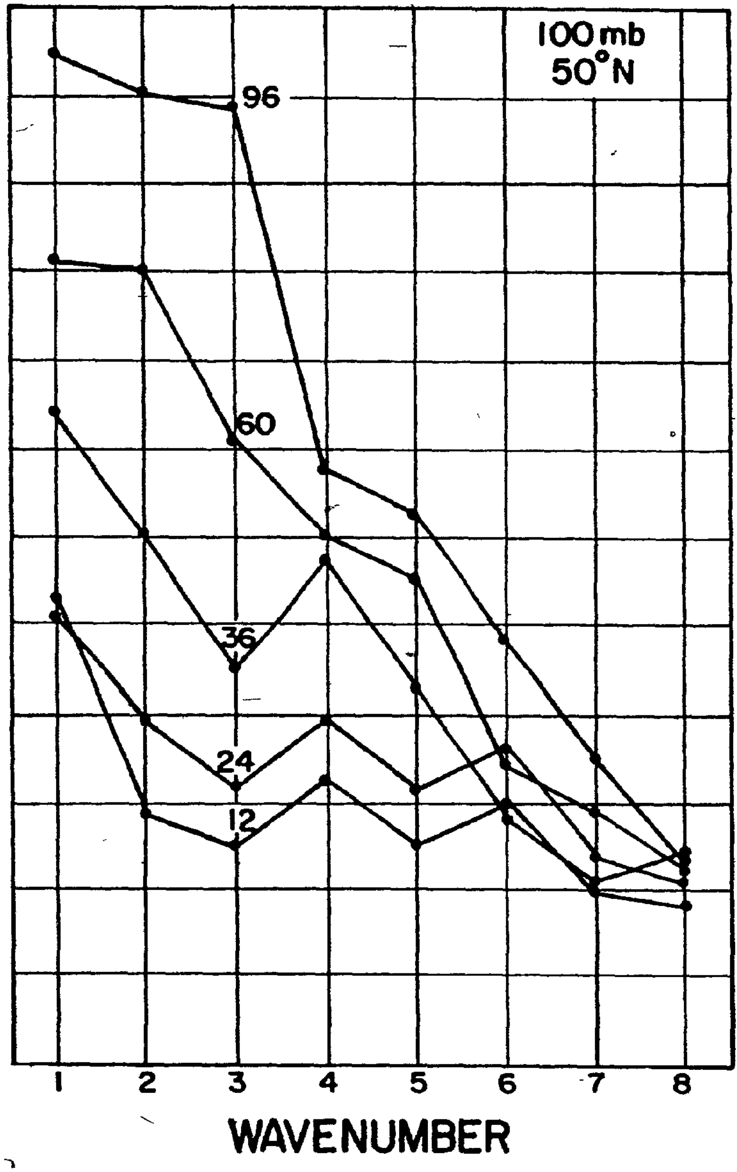

FIGURE (3.7) Same as Figure (3.1) except for the 100 mb height field at 50° N.

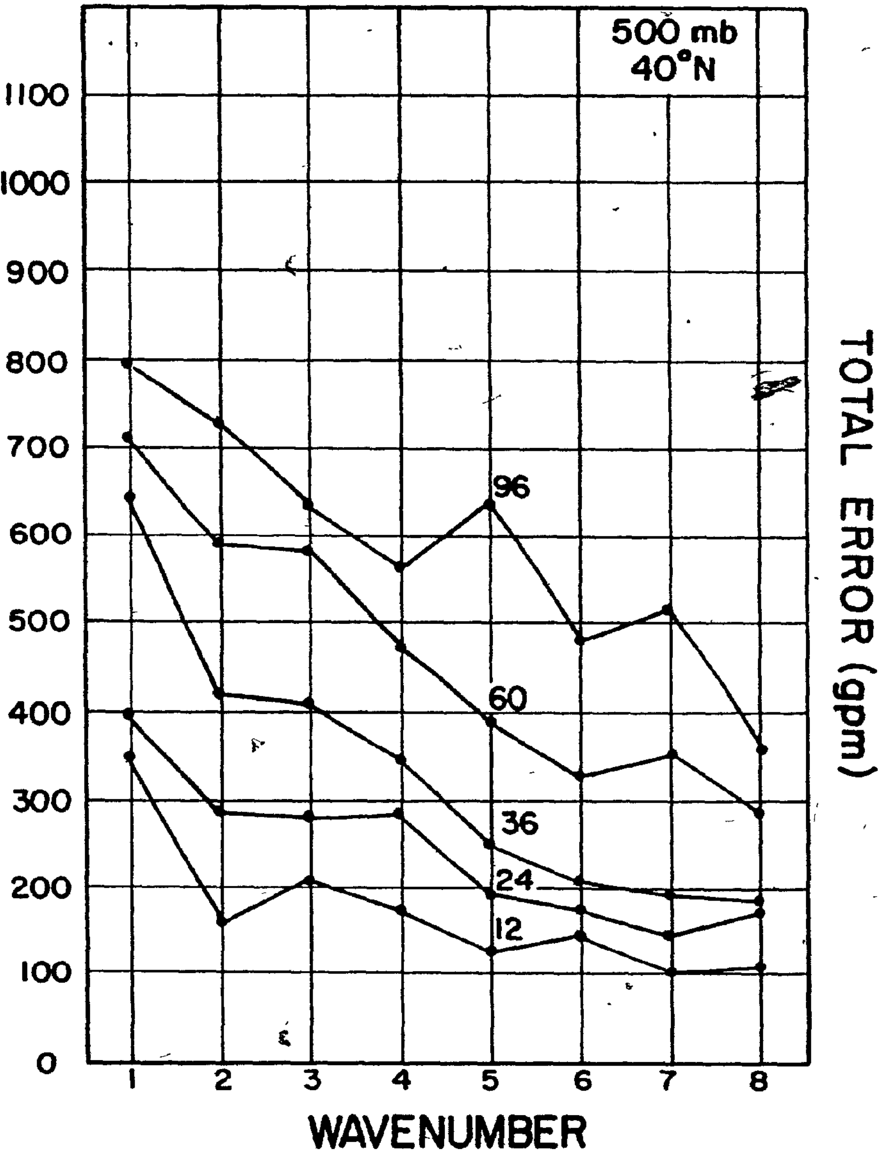

FIGURE (3.10) Same as Figure (3.1) except for the 500 mb height field at 40° N.

cases) normalized by the average amplitude of the zonal wave for 500 mb at 50 N for 12, 24, and 36 hours. The purpose of normalizing is to ensure that the errors are large not only in an absolute sense but also large in comparison to the amplitude of the wave. This diagram shows that in a "percentage error" sense the very long waves are still forecast with large errors. For a 36 hour forecast, there is a minimum at wavenumber four.

Figure (3.9) compares the model to persistence for a 36 hour forecast at 500 mb at 40° N. These results, which may not be significant because of the sample size, show that persistence is a better forecast than the model for wavenumbers one and three and that the model's best performance, using persistence as a standard, is at wavenumber seven.

Figures (3.10) to (3.12) give the latitudinal variation of the total error (absolute) for 500 mb. These diagrams show that, in general, there is a slight decrease in the amplitudes of the errors moving from 40° N to 70° N in the longest waves and a dramatic decrease in the errors in the shorter waves. It is felt that the decrease in the shorter wave errors is due to the fact that the data cannot resolve these short wavelengths at high latitudes.

The positions of the 36 hour error phases at 50° N, as a function of height for wavenumbers one to five, are given in Figures (3.13) to (3.17). From these, it is evident that the error phases have a tendency to cluster in longitude. Wavenumber one, for example, clusters at 25° W at 500 mb. Further inspection reveals that the error phases have their weakest dependence on height near the clustering points.

The latitudinal structure of the error phases at 500 mb for 36 hours is shown in Figures (3.18) to (3.22). It can be seen that the clustering

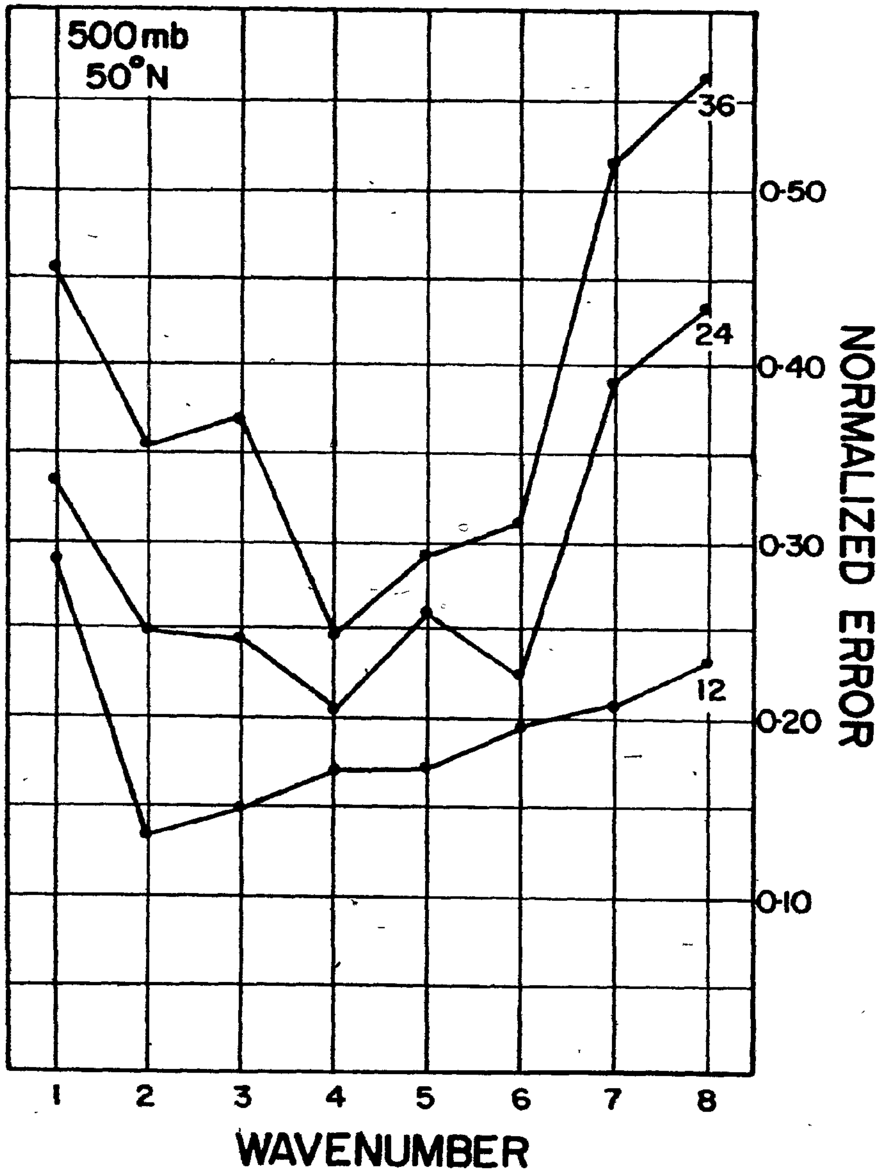

FIGURE (3.8) The normalized error as a function of zonal wavenumber at 500 mb and 50° N for forecasts of 12, 24, and 36 hours.

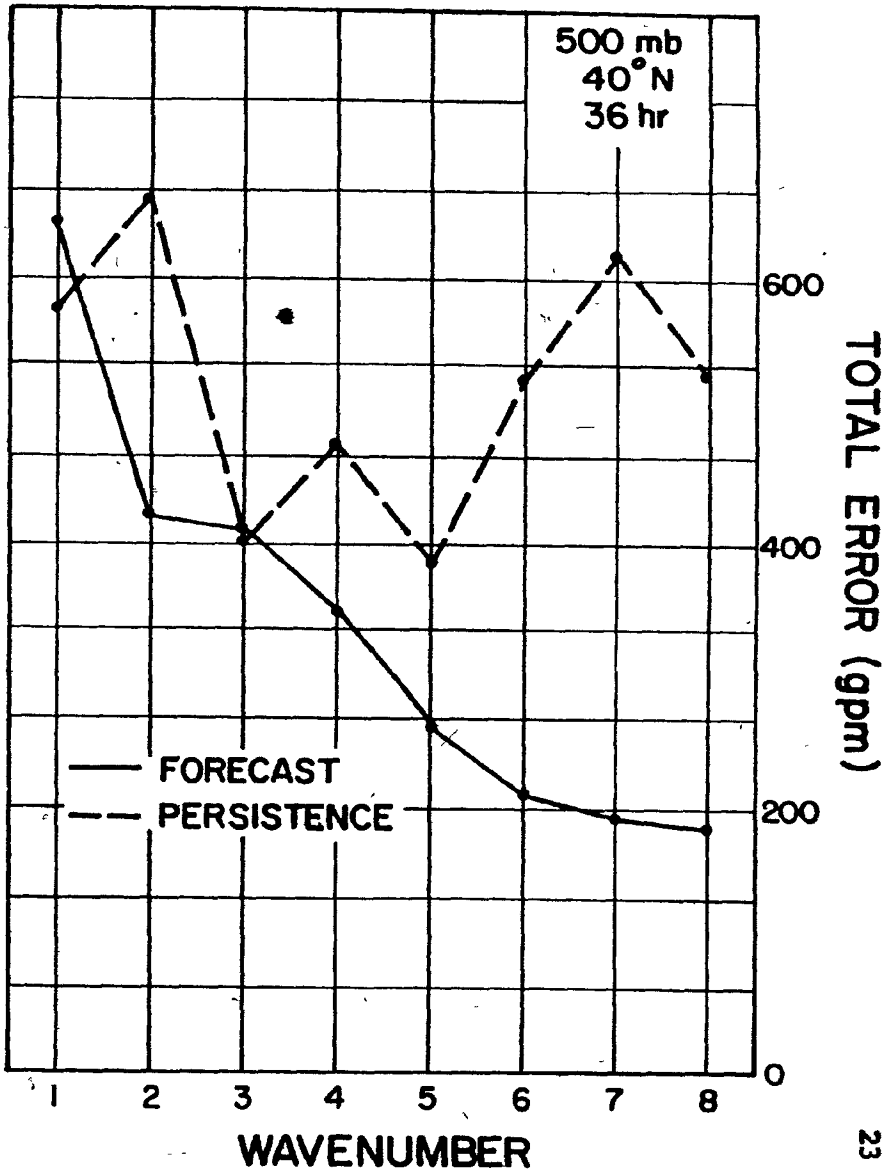

FIGURE (3.9) The total persistence error as a function of wavenumber compared to the total error for 36 hours at 500 mb and 40° N.

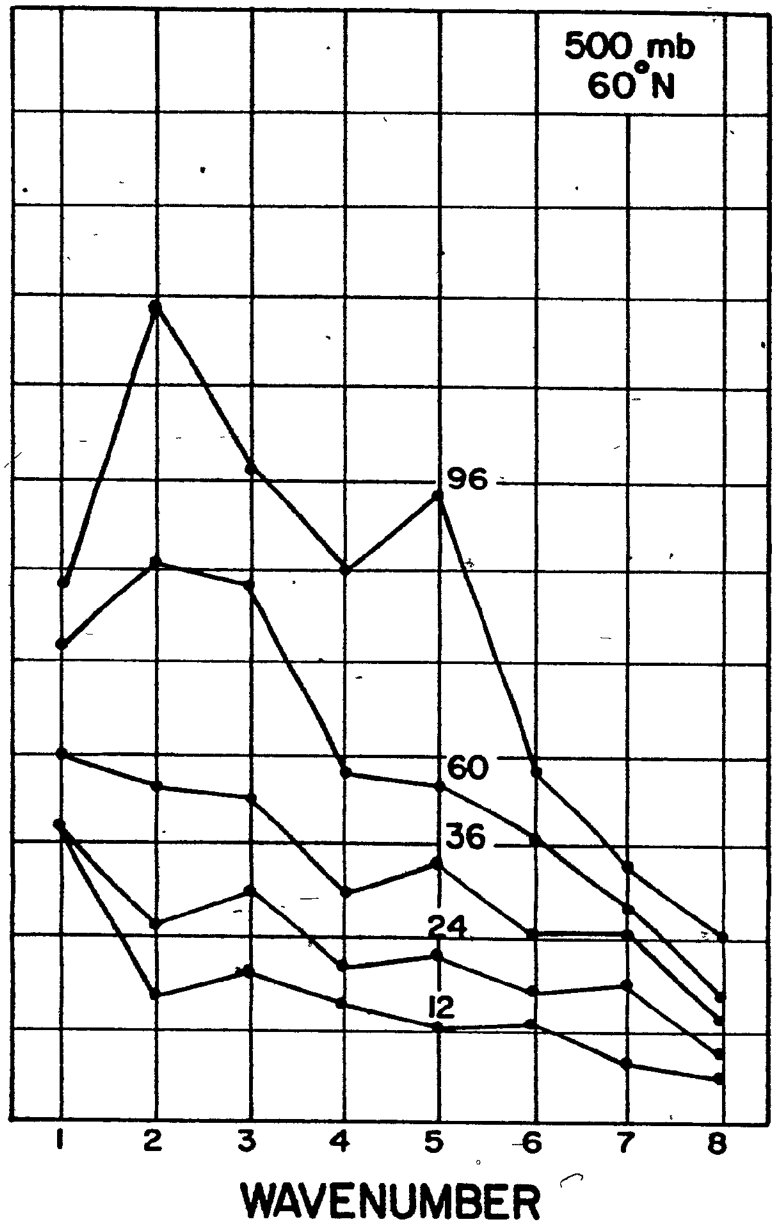

FIGURE (3.11) Same as Figure (3.1) except for the 500 mb height field at 60° N.

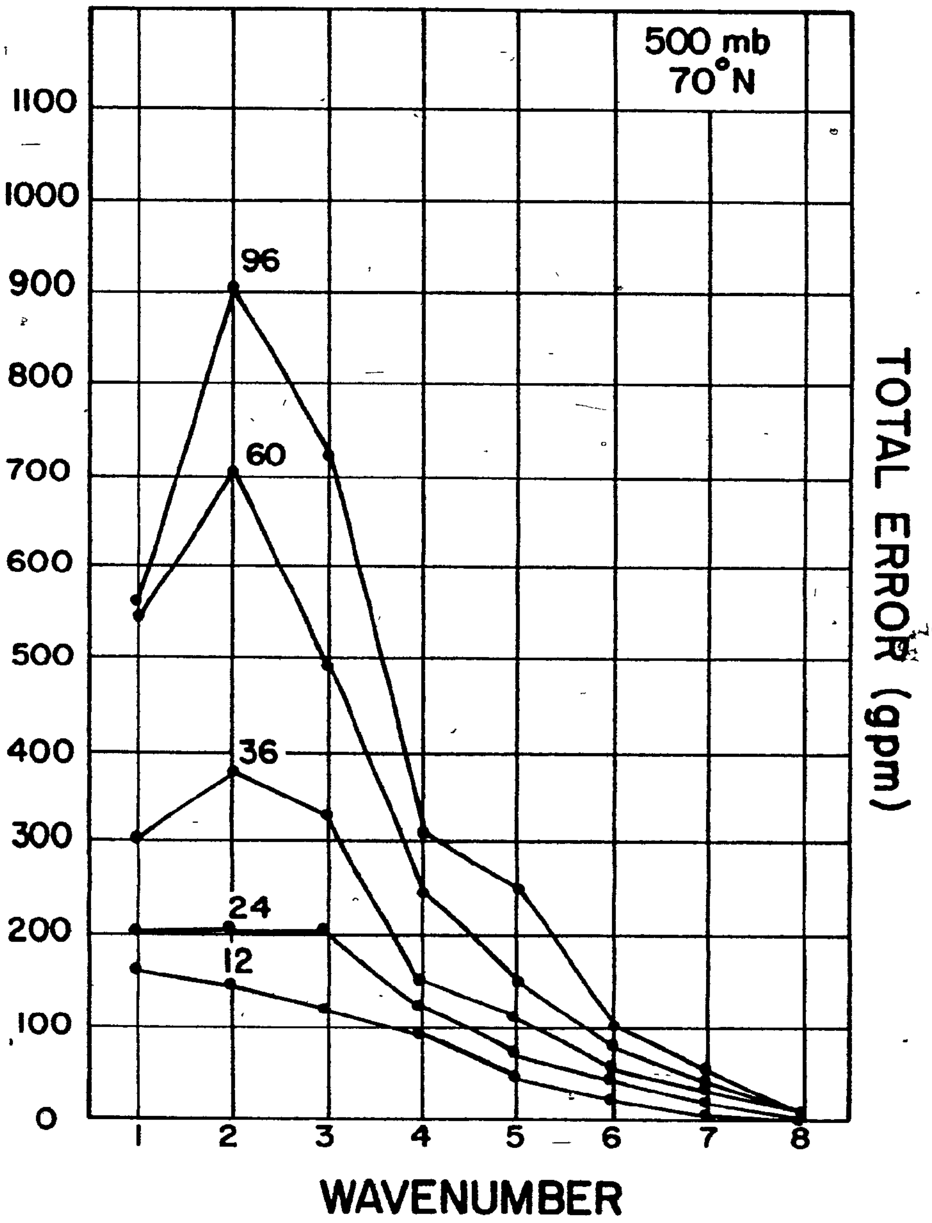

FIGURE (3.12) Same as Figure (3.1) except for the 500 mb height field at 70° N.

diminishes with increasing latitude. This fact makes it difficult to determine the latitudinal structure of the error phases; but, in lower latitudes, it appears to have the weakest dependence on latitude at the clustering points.

The weak vertical structure of the errors of the geopotential height at 36 hours implies that the planetary wave errors in the thickness pattern should be smaller. Figure (3.23) shows a comparison of the total 36 hour 1000 mb to 500 mb thickness error at 50° N and the 500 mb geopotential error at 50° N. It is noted that the wavenumber one errors are reduced by a factor of two and that the geopotential error curve and the thickness error curve become asymptotic at approximately wavenumber six. The thickness error phases for the planetary waves, like those of the geopotentials, show a clustering in longitude.

3.4 Definition of the Errors in the Spherical Harmonic Coefficients

The error field can be expressed as (Equation (3.1))

$$\Phi_e = \sum \sum \Phi_e(m,n) P_n^m e^{im\lambda}.$$

The contribution of a coefficient $\Phi_e(m,n)$ to the error is

$$E(m,n) = \Phi_e(m,n) P_n^m e^{im\lambda} + \Phi_e(-m,n) P_n^{-m} e^{-im\lambda}.$$

It is necessary to use the sum of the positive and negative order coefficients in order to obtain a real (as opposed to complex) contribution to the error. Following the development of Section (3.2), the above equation can be written in the form

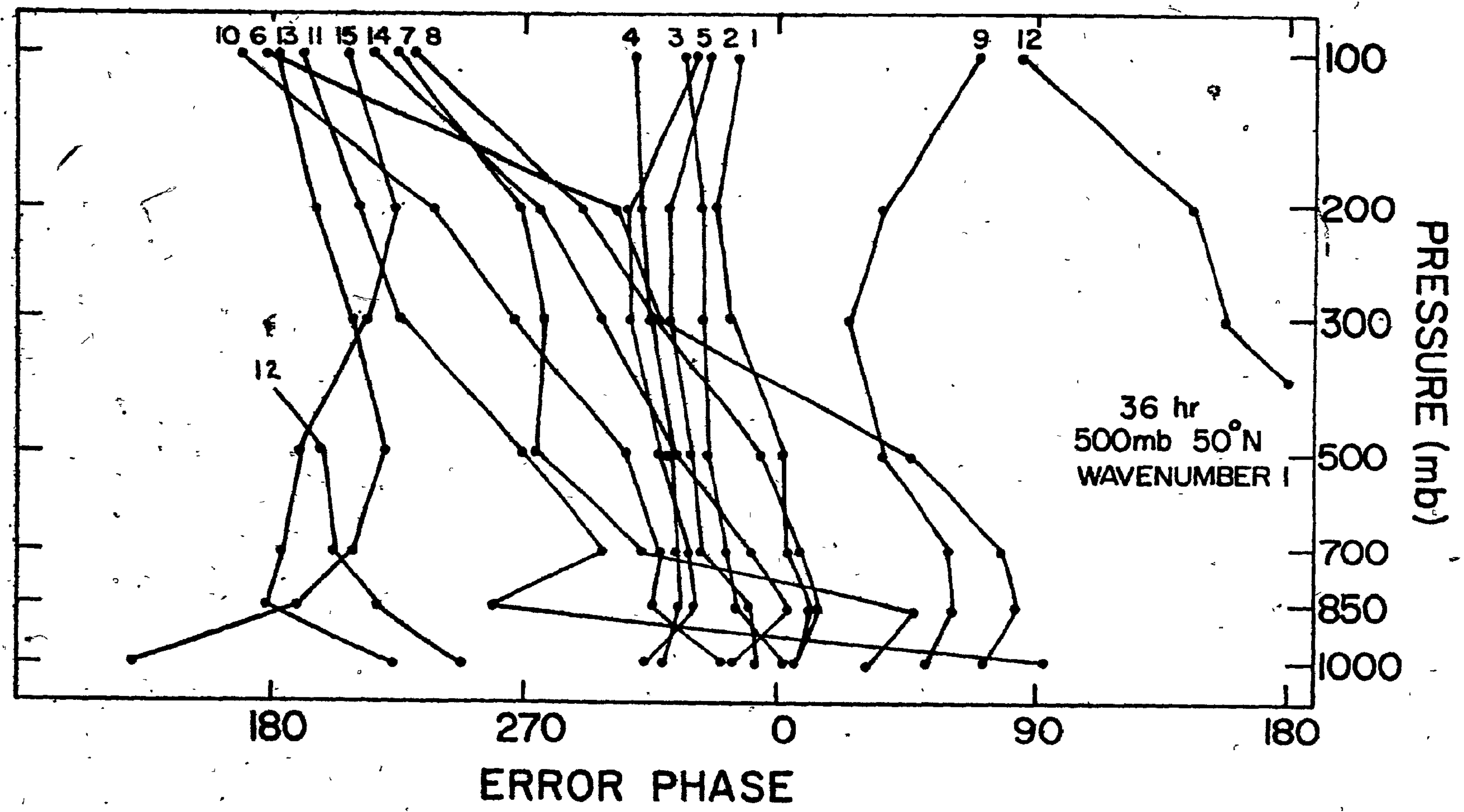

FIGURE (3.13) The 36 hour error phases (positions of a ridge) at 50° N as a function of pressure height for zonal wavenumber 1. Small figures at the top of each profile refer to the case number given in Table (2.1).

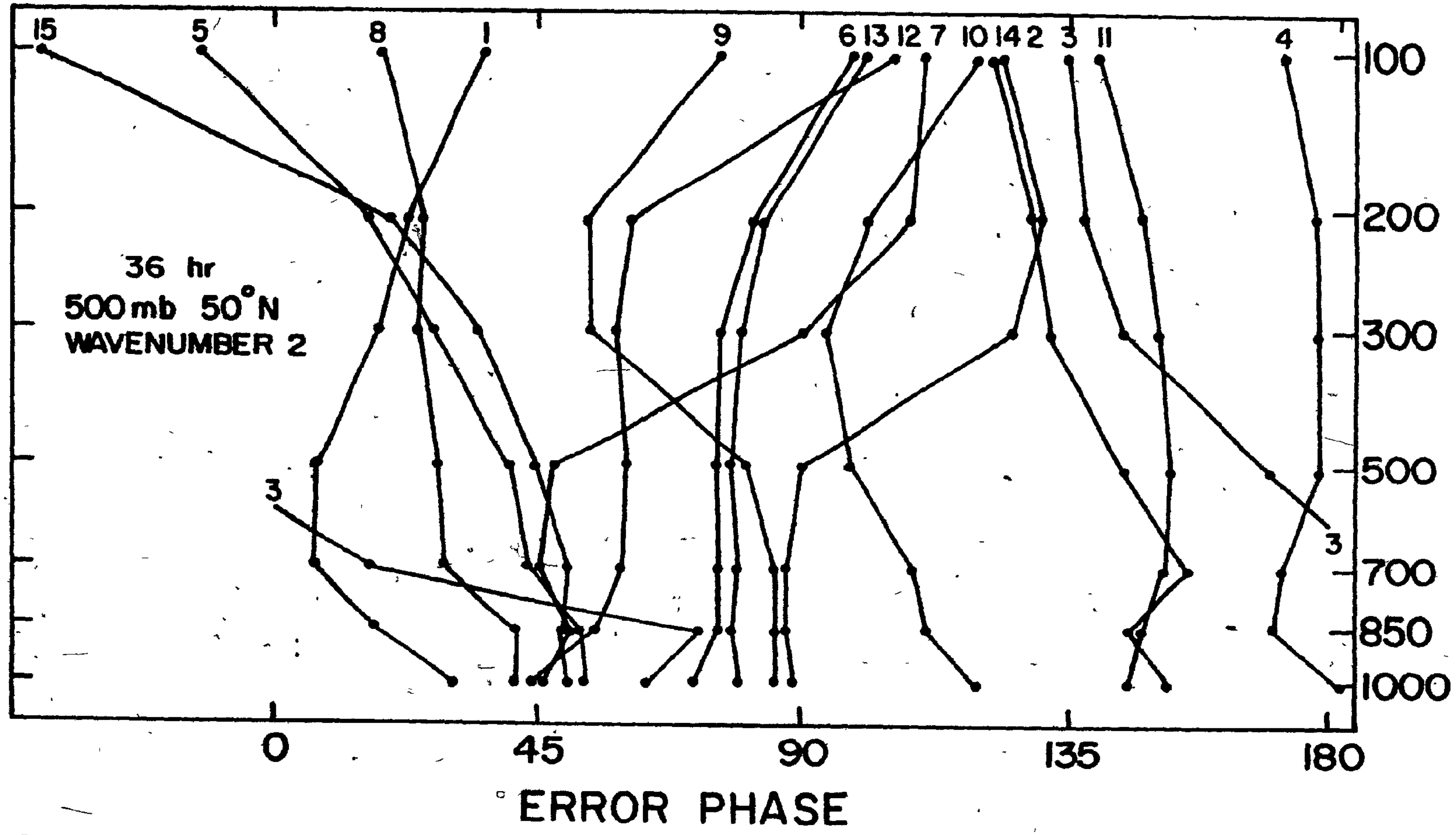

FIGURE (3.14) Same as Figure (3.13) except for zonal wavenumber 2.

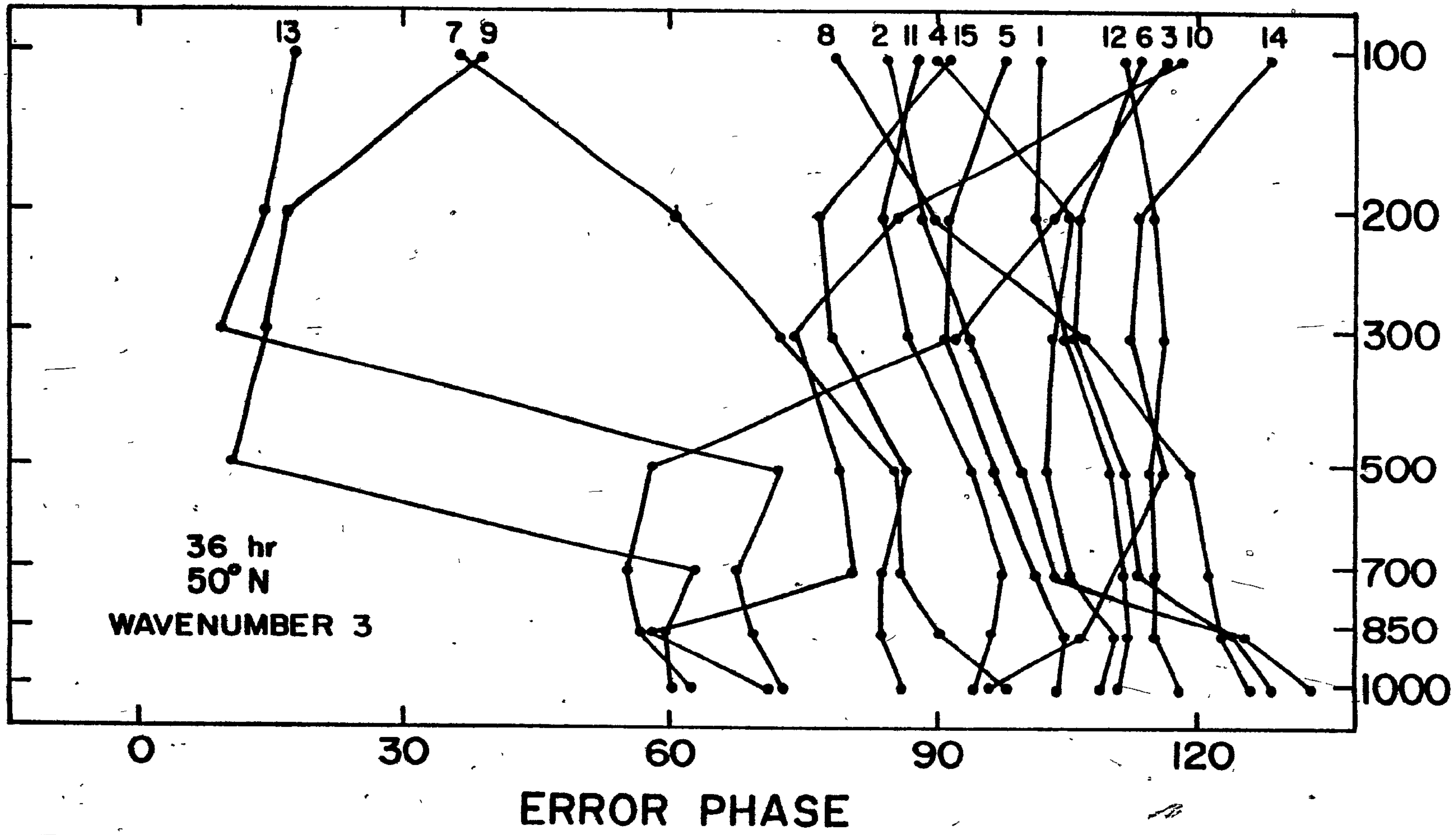

FIGURE (3.15) Same as Figure (3.13) except for zonal wavenumber 3.

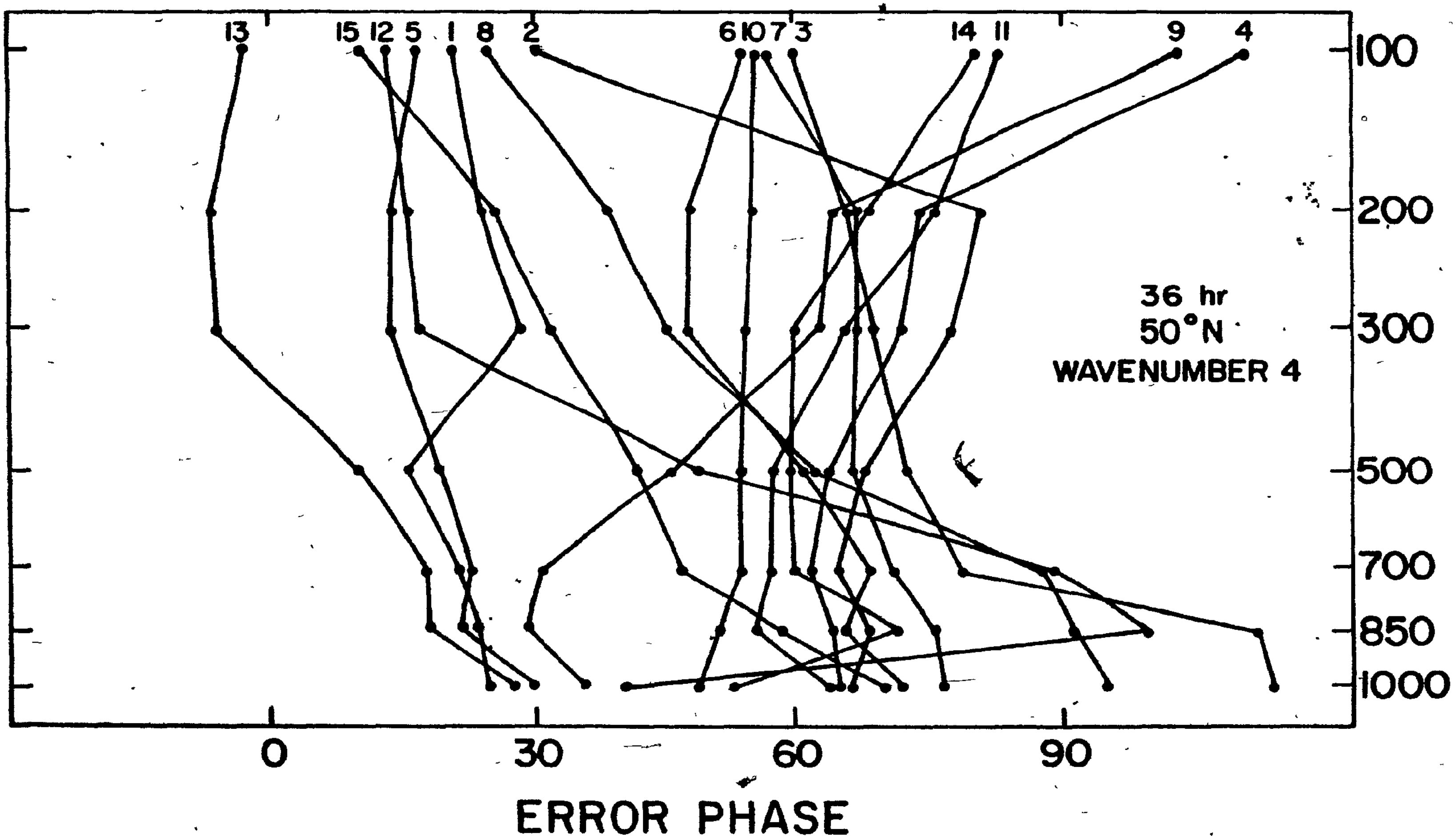

FIGURE (3.16) Same as Figure (3.13) except for zonal wavenumber 4.

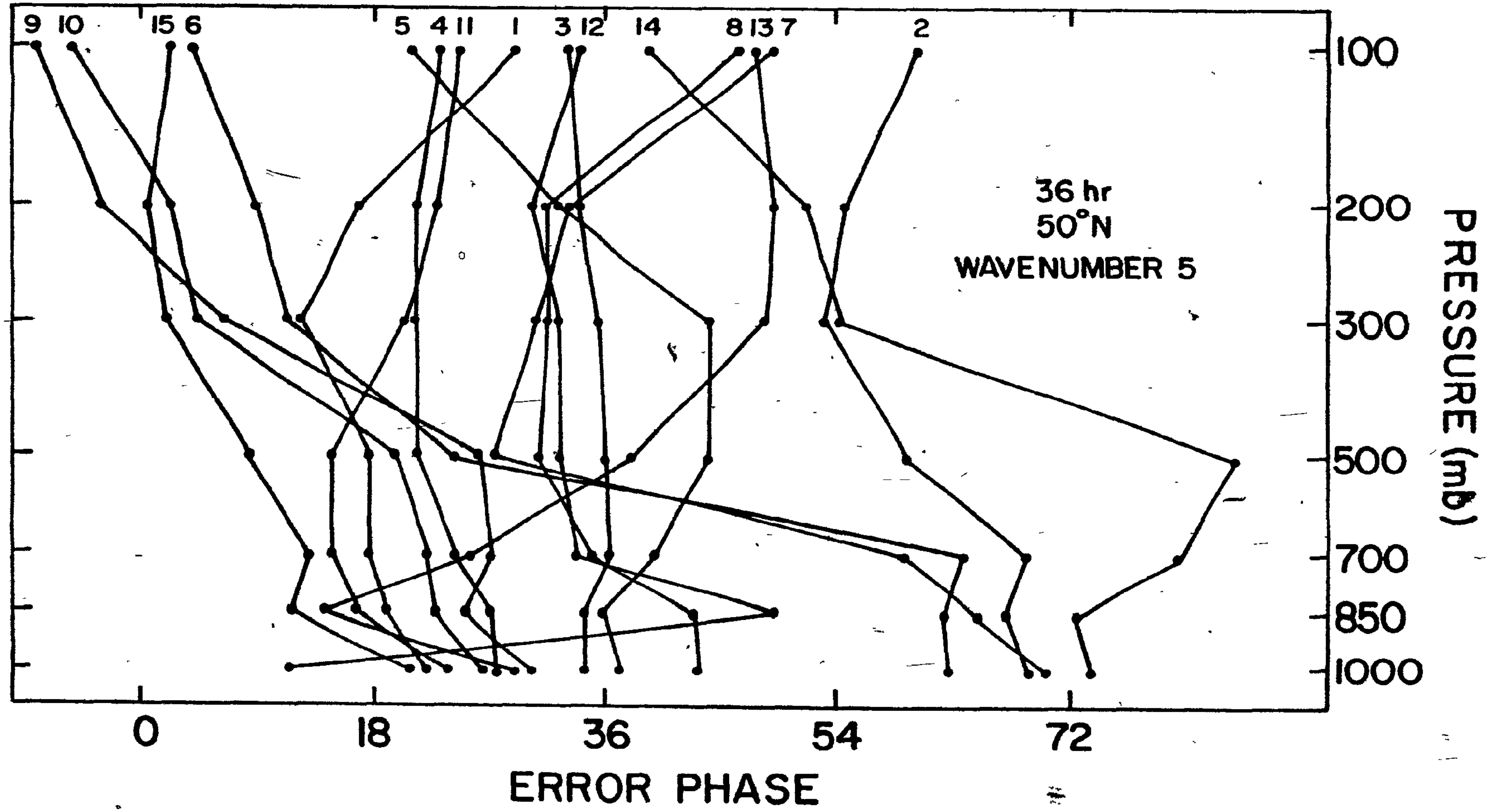

FIGURE (3.17) Same as Figure (3.13) except for zonal wavenumber 5.

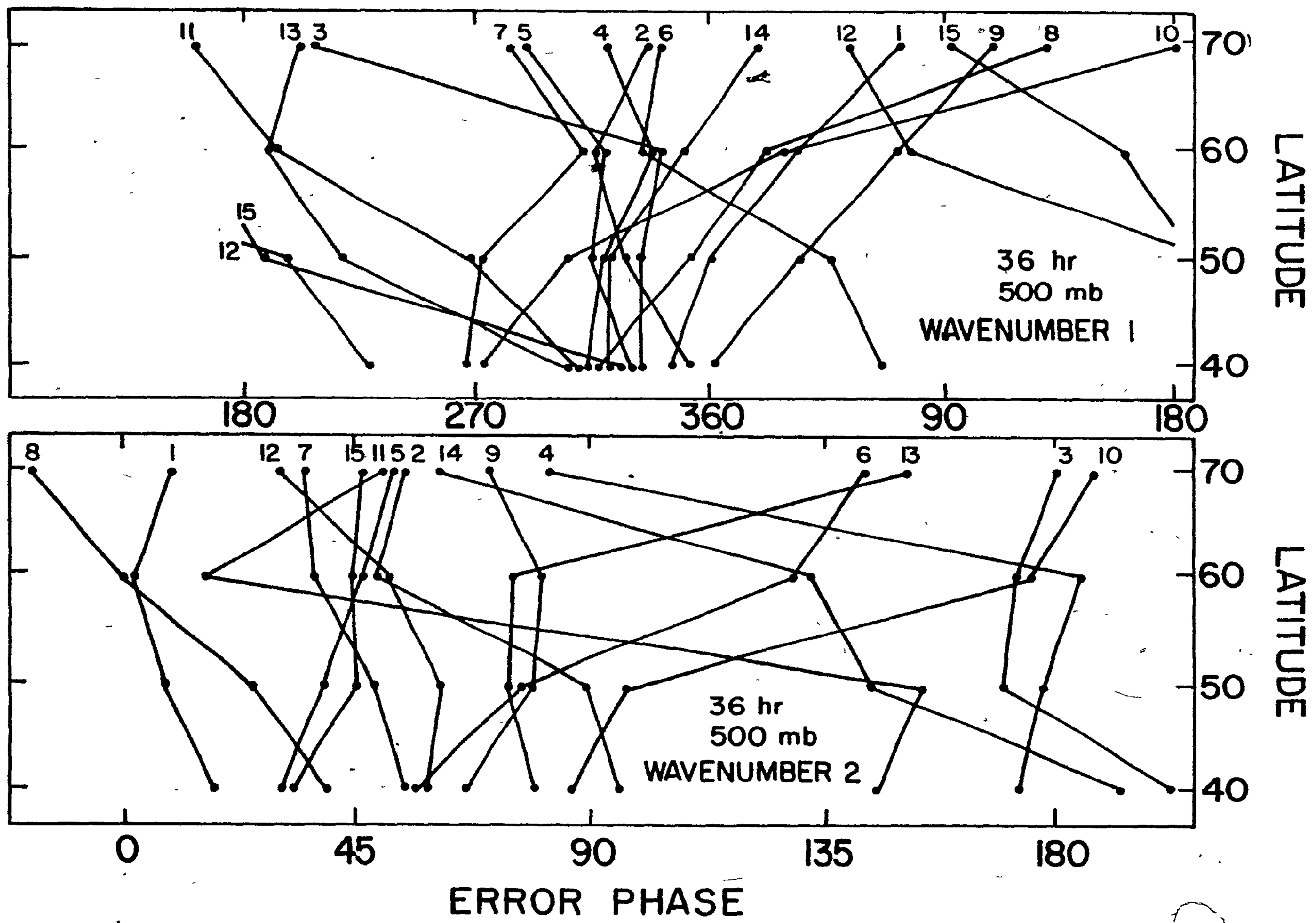

FIGURE (3.18) and FIGURE (3.19) The 36 hour error phases at 500 mb as a function of latitude for zonal wavenumbers 1 and 2. Small figures at the top of each profile refer to the case number.

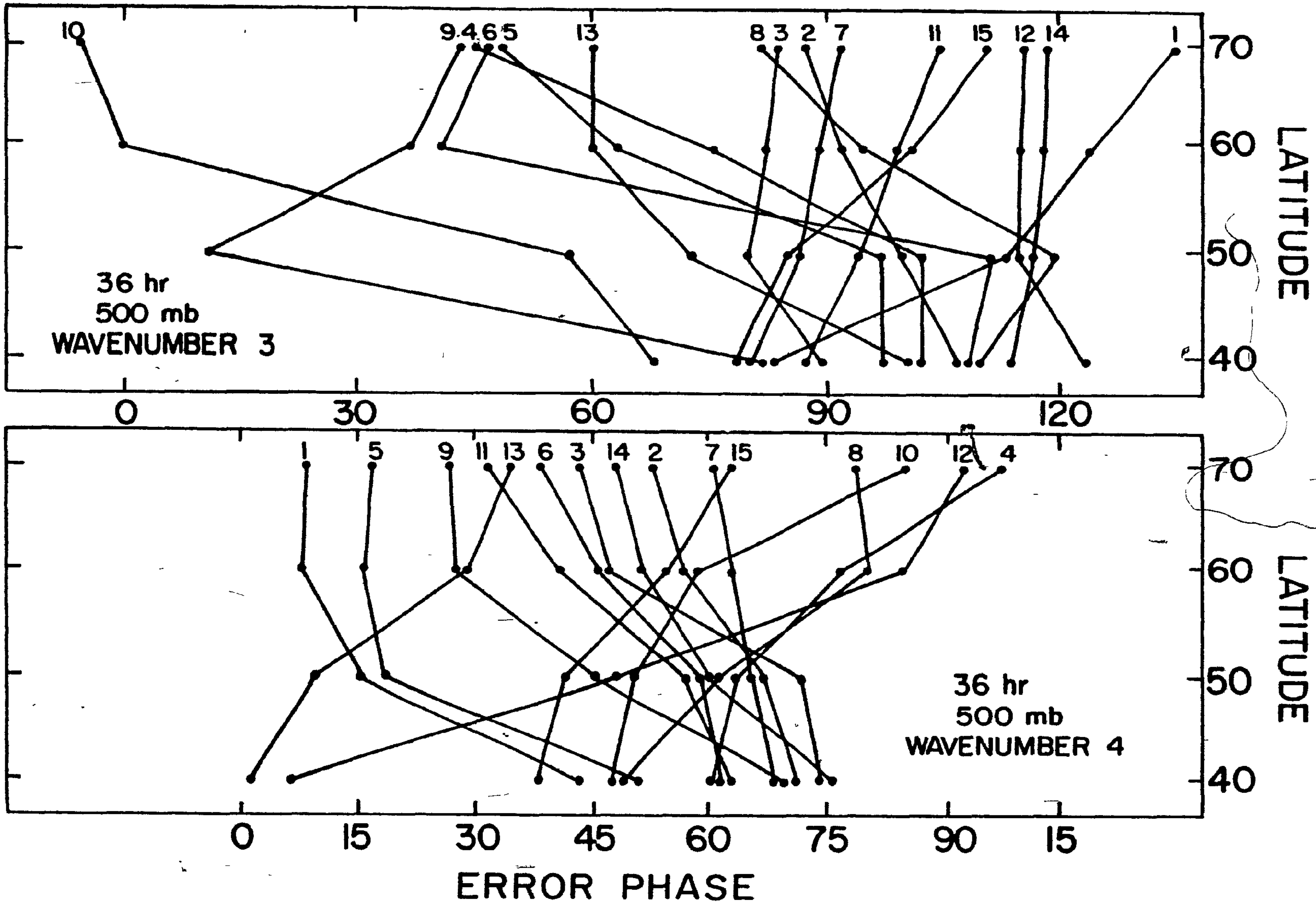

FIGURE (3.20) and FIGURE (3.21) Same as Figure (3.18) except for zonal wavenumbers 3 and 4.

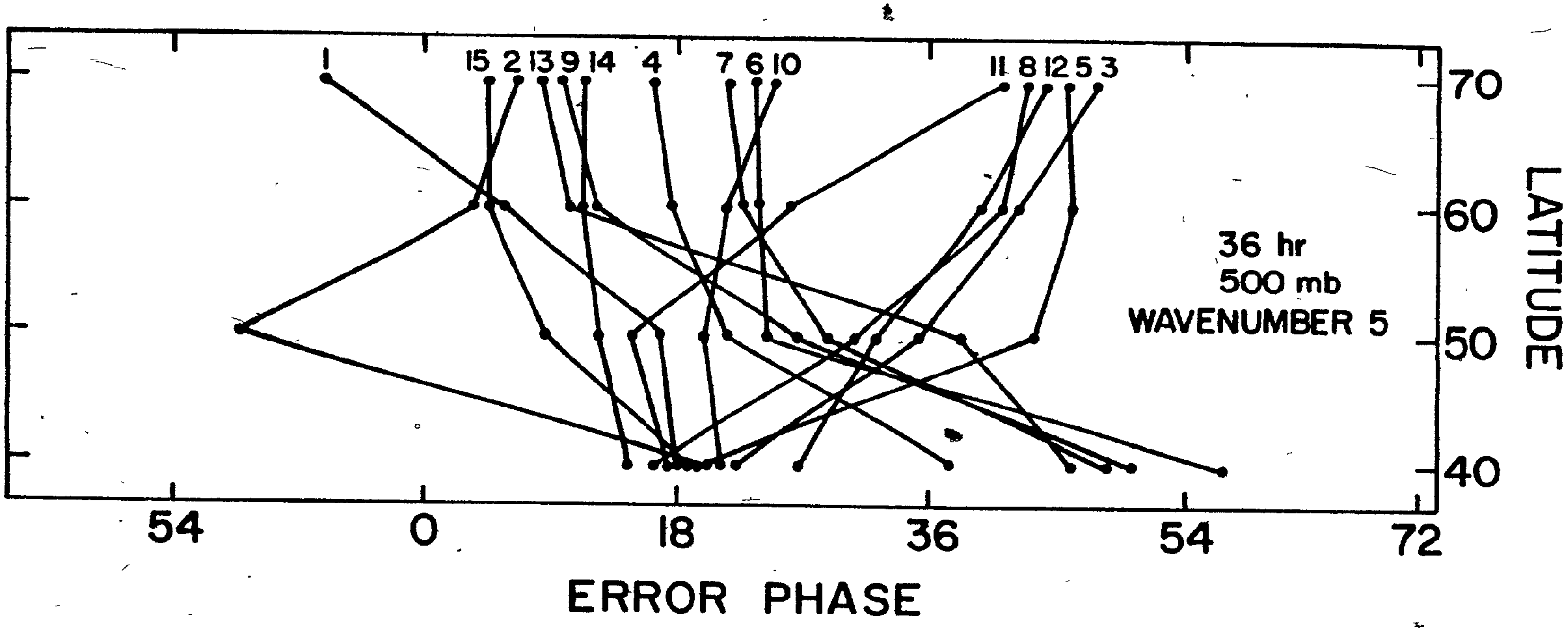

FIGURE (3.22) Same as Figure (3.18) except for zonal wavenumber 5.

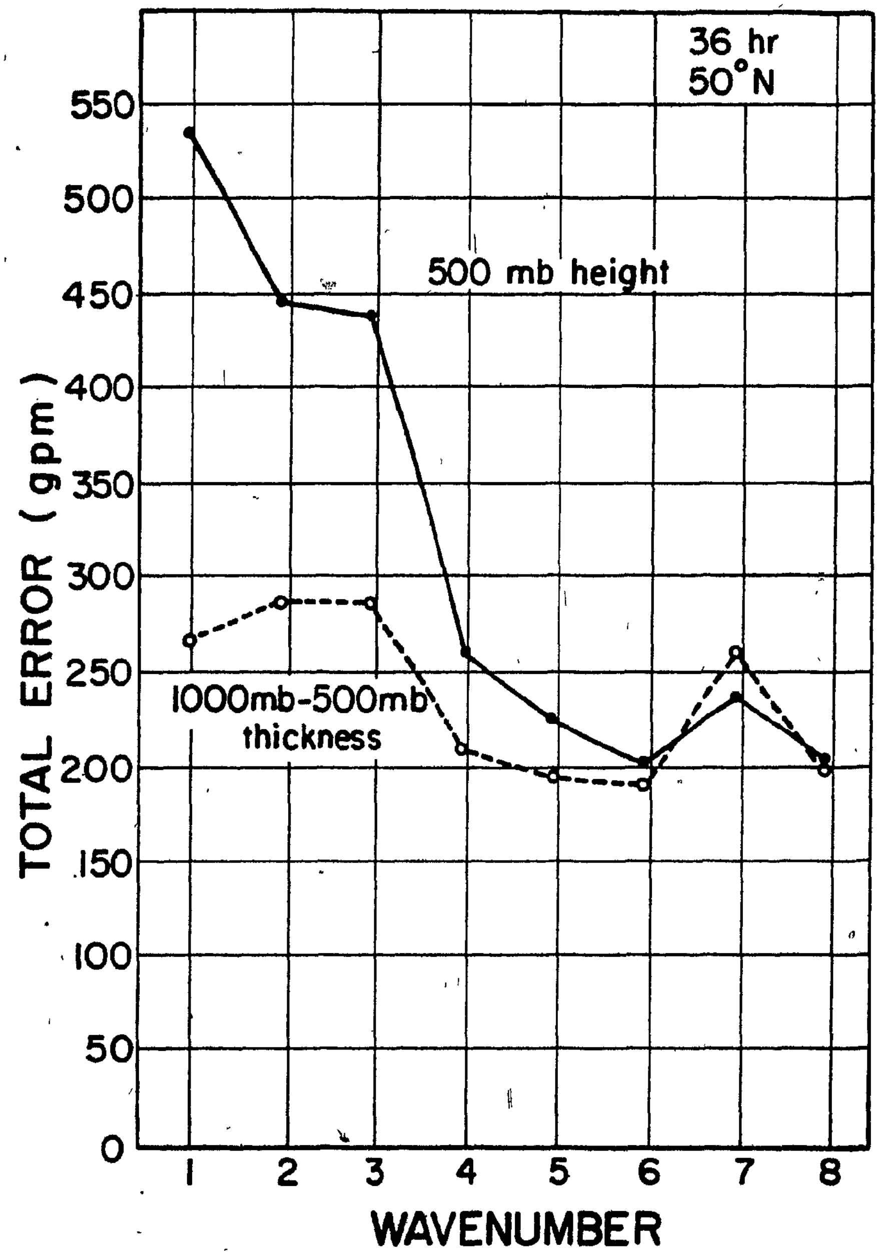

FIGURE (3.23) A comparison of the total 36 hour 500 mb error at 50° N and the 1000 mb to 500 mb total thickness error at 50° N as a function of zonal wavenumber.

$$E(m,n) = A_e(m,n)\, P_n^m \cos\left\{m\left(\lambda - \delta_e(m,n)\right)\right\},$$

where

$$A_e(m,n) = 2\left[Re^2\left\{\Phi_e(m,n)\right\} + Im^2\left\{\Phi_e(m,n)\right\}\right]^{\frac{1}{2}};$$

$$\delta_e(m,n) = \frac{1}{m}\tan^{-1}\frac{-Im\left\{\Phi_e(m,n)\right\}}{Re\left\{\Phi_e(m,n)\right\}}.$$

To remove the latitudinal dependence of the error given in the figures that follow, the associated Legendre function has been factored from the error amplitude. In the results that follow, the error amplitude $A_e(m,n)$ has been normalized by the average magnitude of the spherical harmonic coefficient, i.e. the average of

$$2\left[Re^2\left\{\Phi_o(m,n)\right\} + Im^2\left\{\Phi_o(m,n)\right\}\right]^{\frac{1}{2}}.$$

3.5 <u>Error Results for the Spherical Harmonic Coefficients</u>

Figures (3.24) to (3.31) give the normalized errors in the spherical harmonic coefficients of the 500 mb geopotentials as a function of time and zonal wavenumber: The errors in most of the components of each zonal wave grow at approximately the same rate. The rate of growth is slowest in the longer waves and most rapid in the shorter waves. The time taken for the normalized error to reach two-thirds in wavenumber one is about 96 hours; while in wavenumber eight, it is about 42 hours. There are, however, several coefficients whose rapid error growth does not conform to the above pattern.

These coefficients are (1,1), (2,2), (2,4), (3,3) and (4,4). It is reasonable to postulate that the above coefficients contribute significantly to the large errors in the planetary waves. It is interesting to note that these components possess both low meridional wavenumber and low zonal wavenumber. The character of the errors in these coefficients will be discussed more fully in Chapter 5.

3.6 Summary

Predictability experiments described in Section (1.1) suggest that forecast errors should have the smallest rate of growth in the largest scales of motion with an increasing rate of growth for decreasing scales. The height field forecast error in the present model has a minimum at approximately wavenumber four and increases with higher and lower wavenumbers. Although these results are not expected from predictability considerations, they are very similar to those of Leith's one-level barotropic study which showed an error minimum at wavenumber six.

The model's 1000 mb to 500 mb thickness (vertically averaged temperature) error dependence on wavenumber at 36 hours shows a monotonically increasing error with increasing wavenumber. The large errors in the lowest wavenumbers, which were present in the height field, do not exist in the thickness field. This result suggests that the 36 hour planetary wave error in the height field is barotropic in nature.

The error phases at 36 hours have a tendency to "cluster" in longitude showing that a significant time-averaged error exists.

When the zonal waves are decomposed into their component spherical harmonic coefficients, those coefficients possessing lowest meridional wavenumbers have the largest error in the short time range.

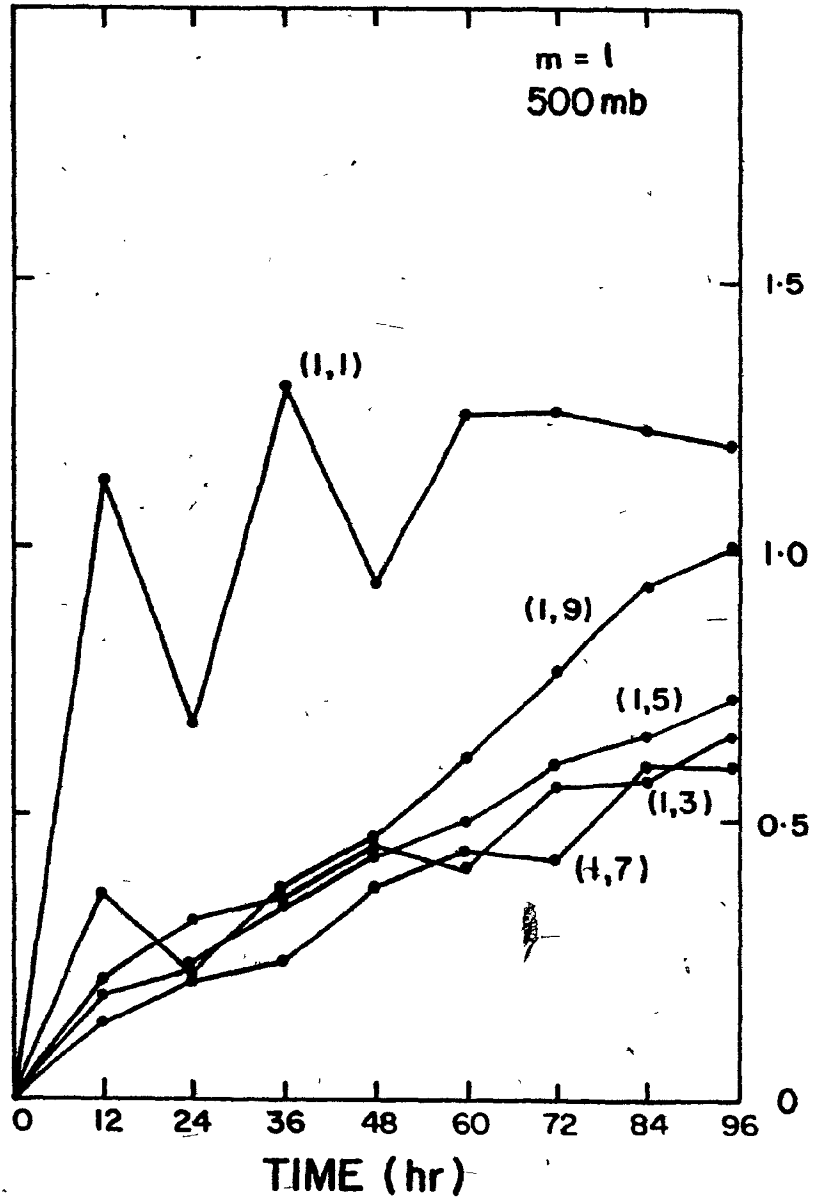

FIGURE (3.24) The normalized error of the spherical harmonic coefficients of the 500 mb height field of zonal wavenumber one as a function of time.

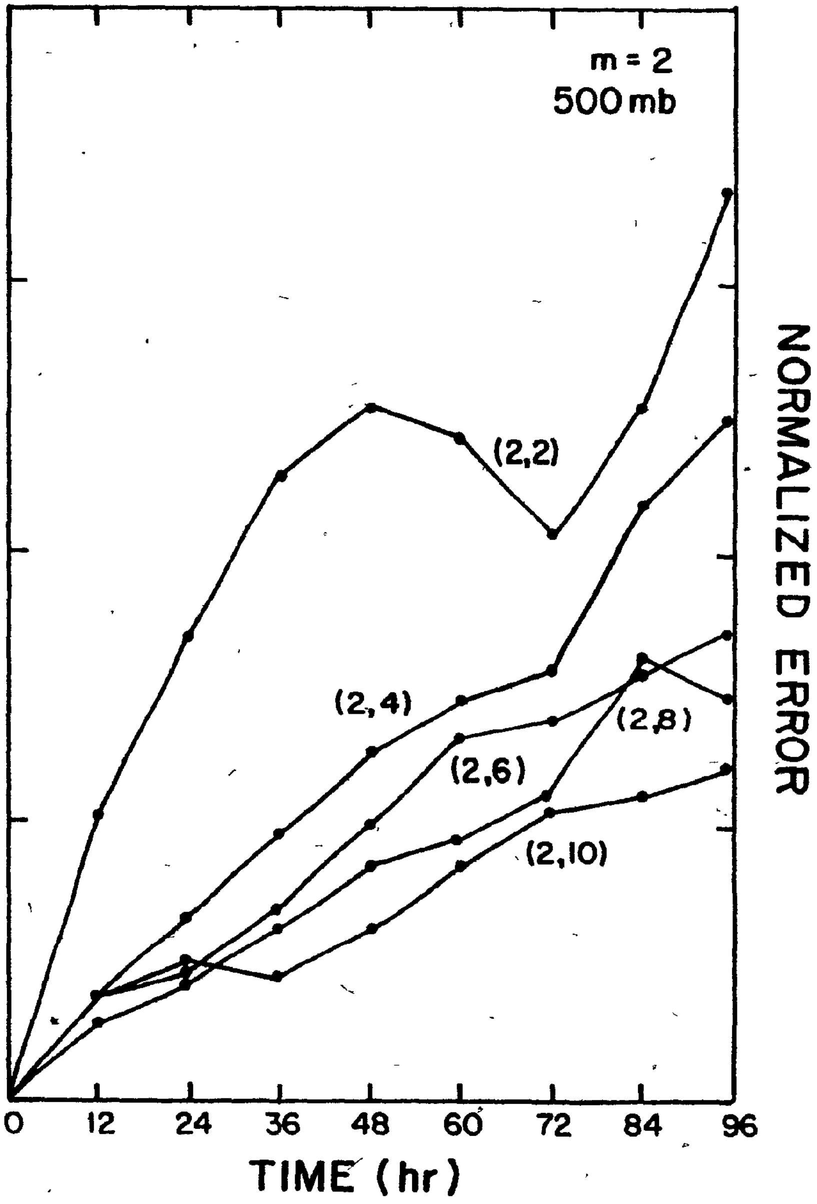

FIGURE (3.25) Same as Figure (3.24) except for zonal wavenumber two.

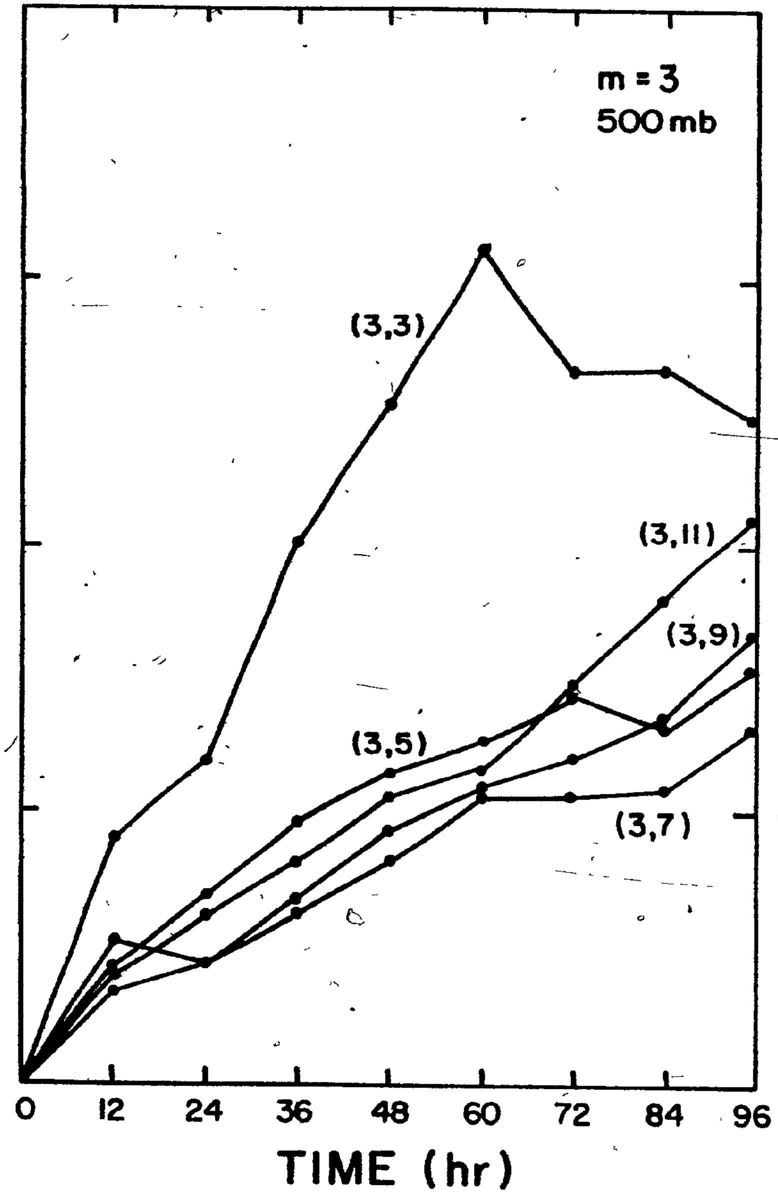

FIGURE (3.26) Same as Figure (3.24) except for zonal wavenumber three.

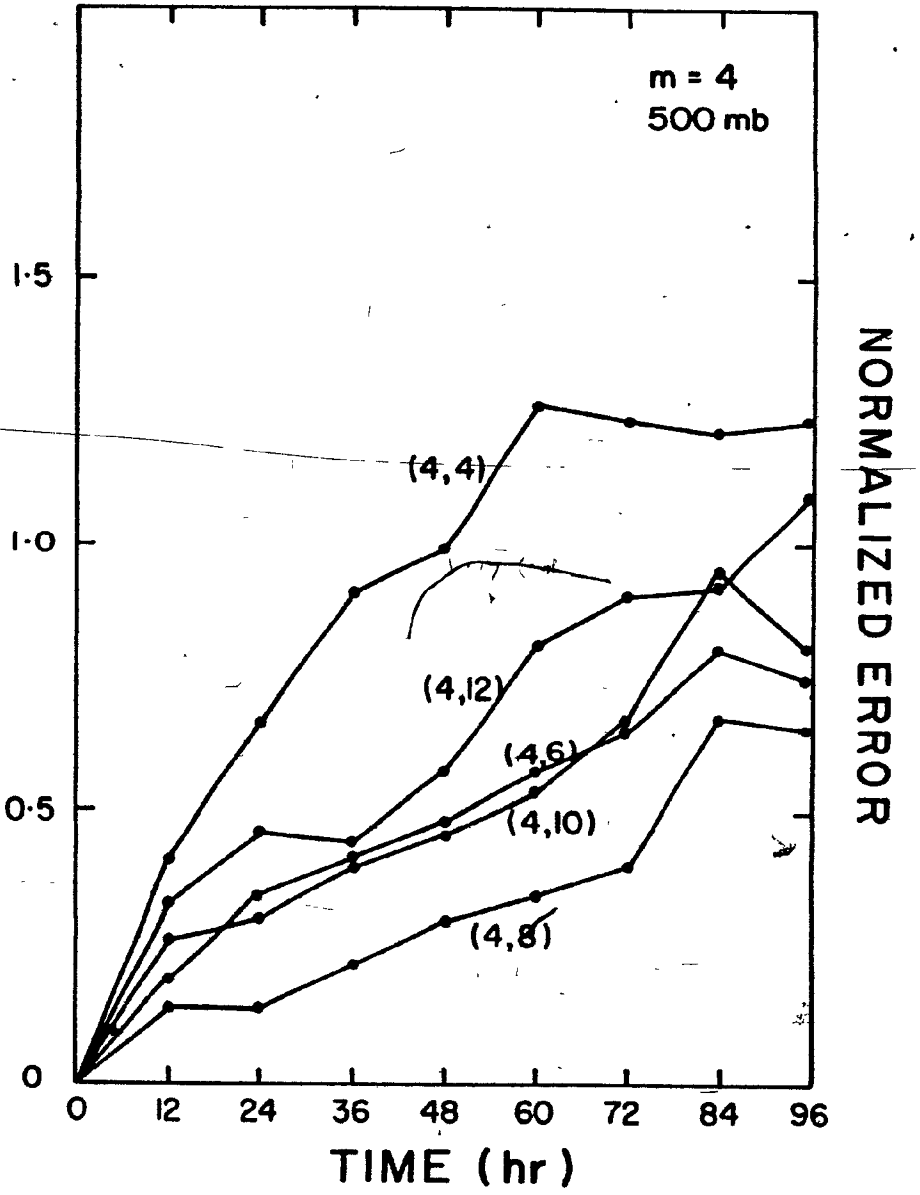

FIGURE (3.27) Same as Figure (3.24) except for zonal wavenumber four.

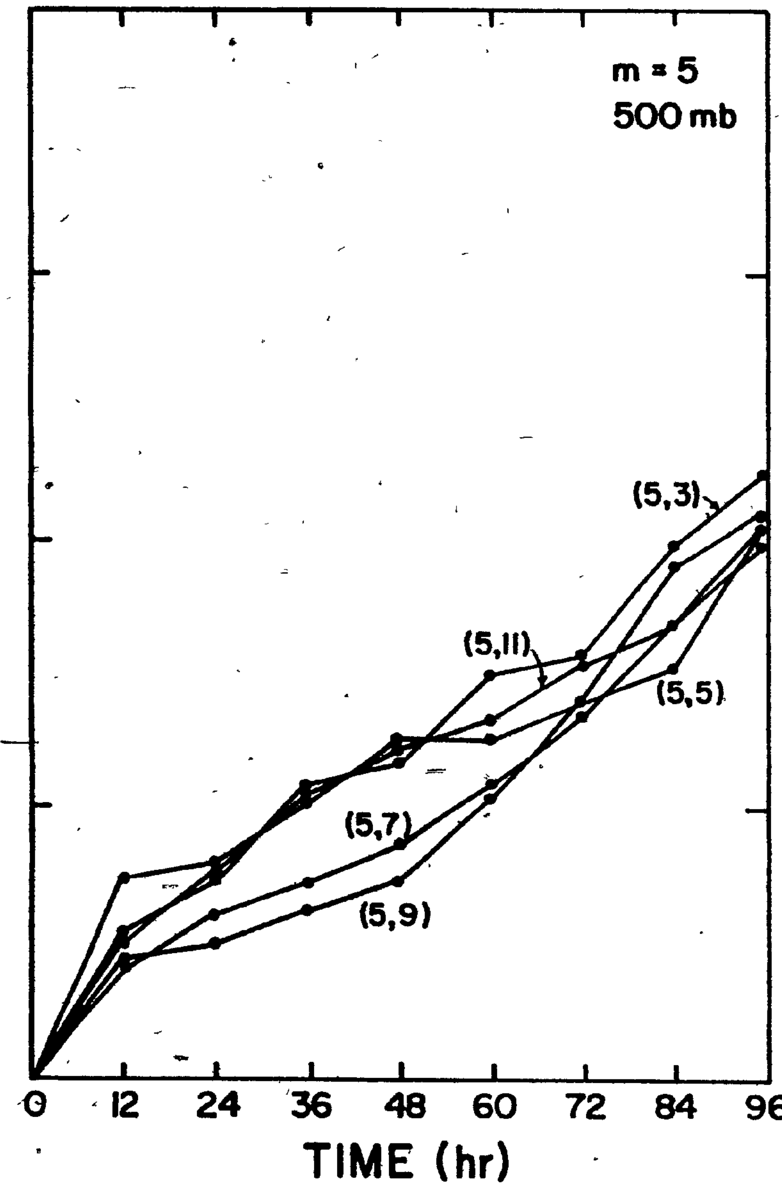

FIGURE (3.28) Same as Figure (3.24) except for zonal wavenumber five.

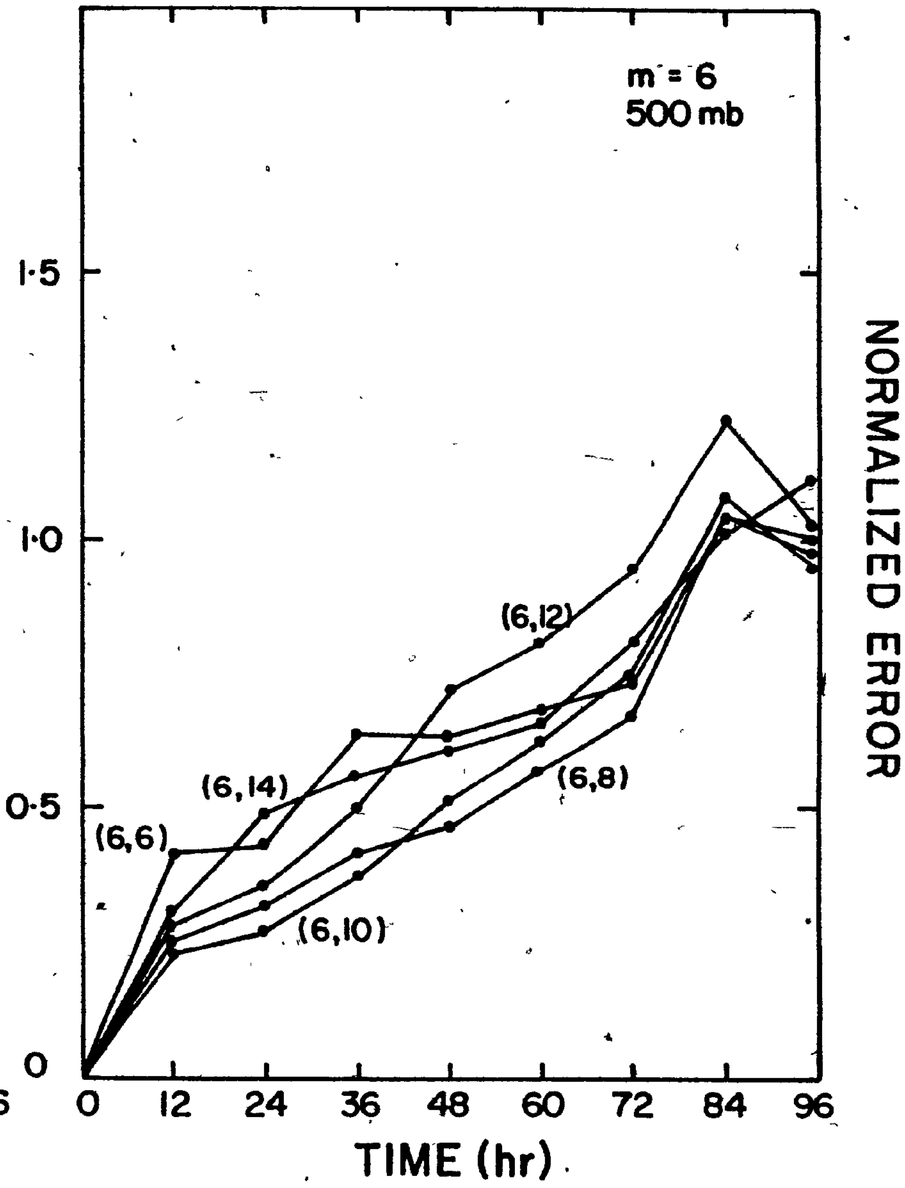

FIGURE (3.29) Same as Figure (3.24) except for zonal wavenumber six.

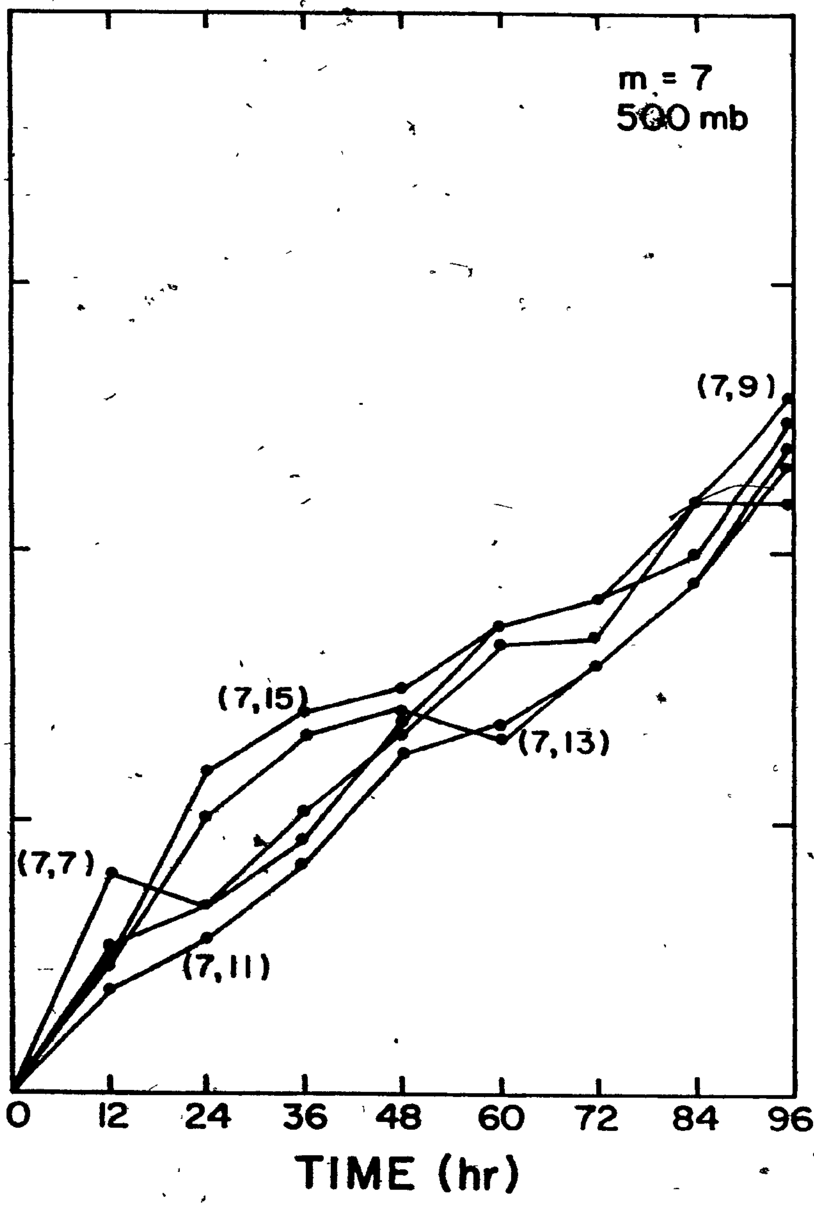

FIGURE (3.30) Same as Figure (3.24) except for zonal wavenumber seven.

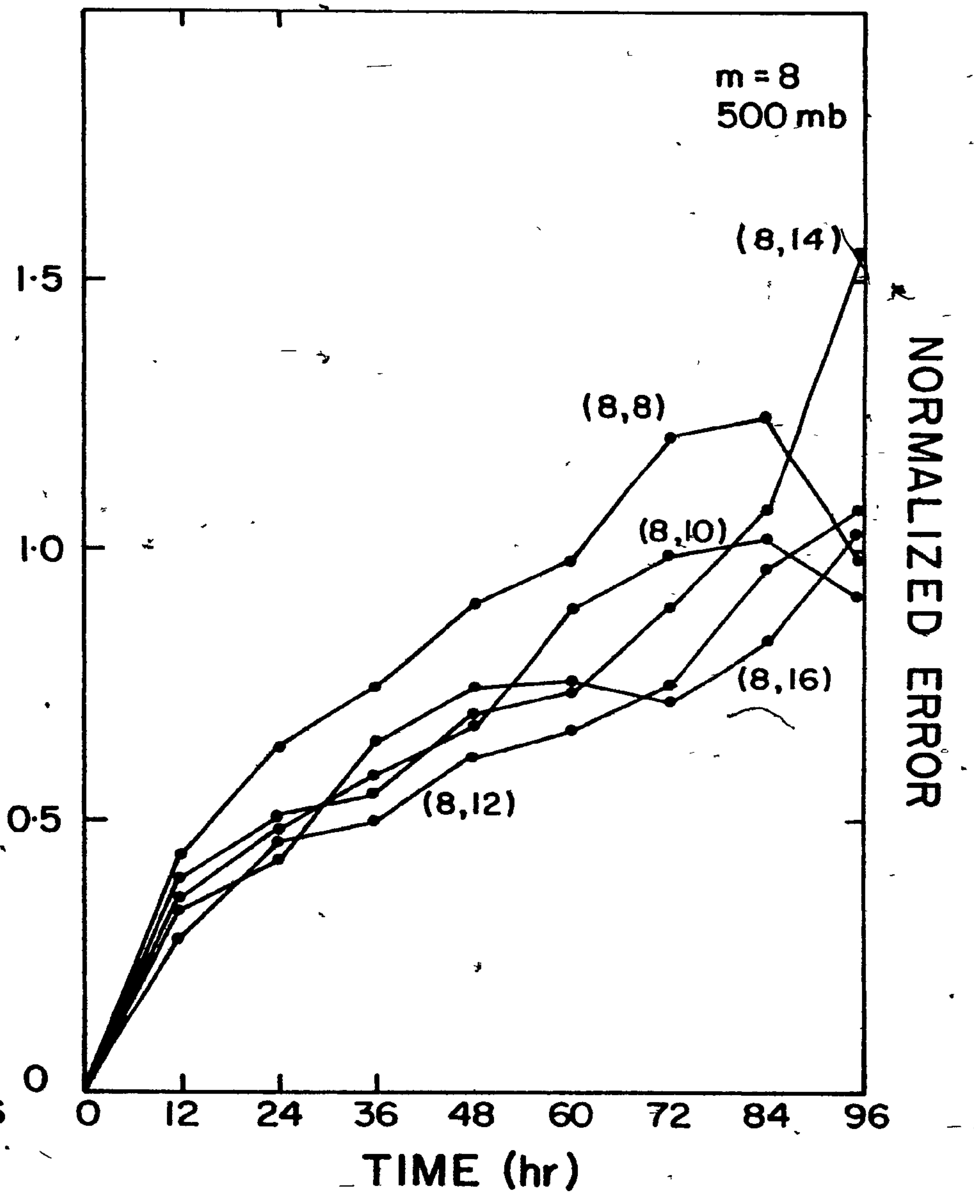

FIGURE (3.31) Same as Figure (3.24) except for zonal wavenumber eight.

CHAPTER 4

THE GEOGRAPHIC AND SYNOPTIC CHARACTER OF THE PLANETARY WAVE ERRORS

4.1 Introduction

It was shown in the previous chapter that the planetary waves possess a significant time-averaged or systematic error. In this chapter, the geographical bias of planetary wave forecasts will be shown. As well, the synoptic appearance of the errors will be presented.

The improvement in planetary wave forecasts, resulting from the removal of the barotropic component of the error by correction of the model's surface pressure, will be shown.

4.2 Geographical Distribution of the Average Error

The systematic nature of the planetary wave error pattern implies that a geographical bias exists in forecasts. To show this error, each of the spherical harmonic coefficients of the error field was averaged over the fifteen cases and the systematic error field was then produced using

$$\Phi_{SYS} = \sum_{m=-5}^{5} \sum_{n=|m|}^{|m|+8} \Phi_{SYS}(m,n)\, Y_n^m ,$$

where Φ_{SYS} = systematic error field,

Y_n^m = spherical harmonic,

$\Phi_{SYS}(m,n)$ = systematic error field coefficient,

and

$$\Phi_{SYS}(m,n) = \frac{1}{N} \sum_{i=1}^{N} \underset{i}{\Phi}_e(m,n) \ ,$$

where $\underset{i}{\Phi}_e(m,n)$ = error coefficient of the "i"th case,

N = number of cases (15).

Figures (4.1) to (4.3) give the 36 hour error field in the 1000 mb geopotential height, the 500 mb geopotential height, and the 1000 mb to 500 mb thicknesses. These charts display the systematic error Φ_{SYS} in the mid-latitude belt from 30° N to 75° N. At 1000 mb, the maximum errors occur in the southern portion of the belt off the east coast of Asia and in the Atlantic Ocean. In contrast, the northern portion of the map is relatively error free (in a systematic sense). The 1000 mb to 500 mb thickness pattern possesses smaller error values, as expected from the results of the previous chapter, with the largest errors occurring in the north near Baffin Island. The 500 mb error field, which is the sum of the previous two, shows that the errors are at a maximum around 40° N and that the phases of the error field are relatively independent of latitude except in the north. The magnitudes and positions of the 500 mb systematic errors agree remarkably well with those found by Martin (1958) in a one-level barotropic model. If the 500 mb systematic error field is compared to a 500 mb mean January map, it can be seen that the geopotential heights are systematically forecast low in mean ridges and high in mean troughs.

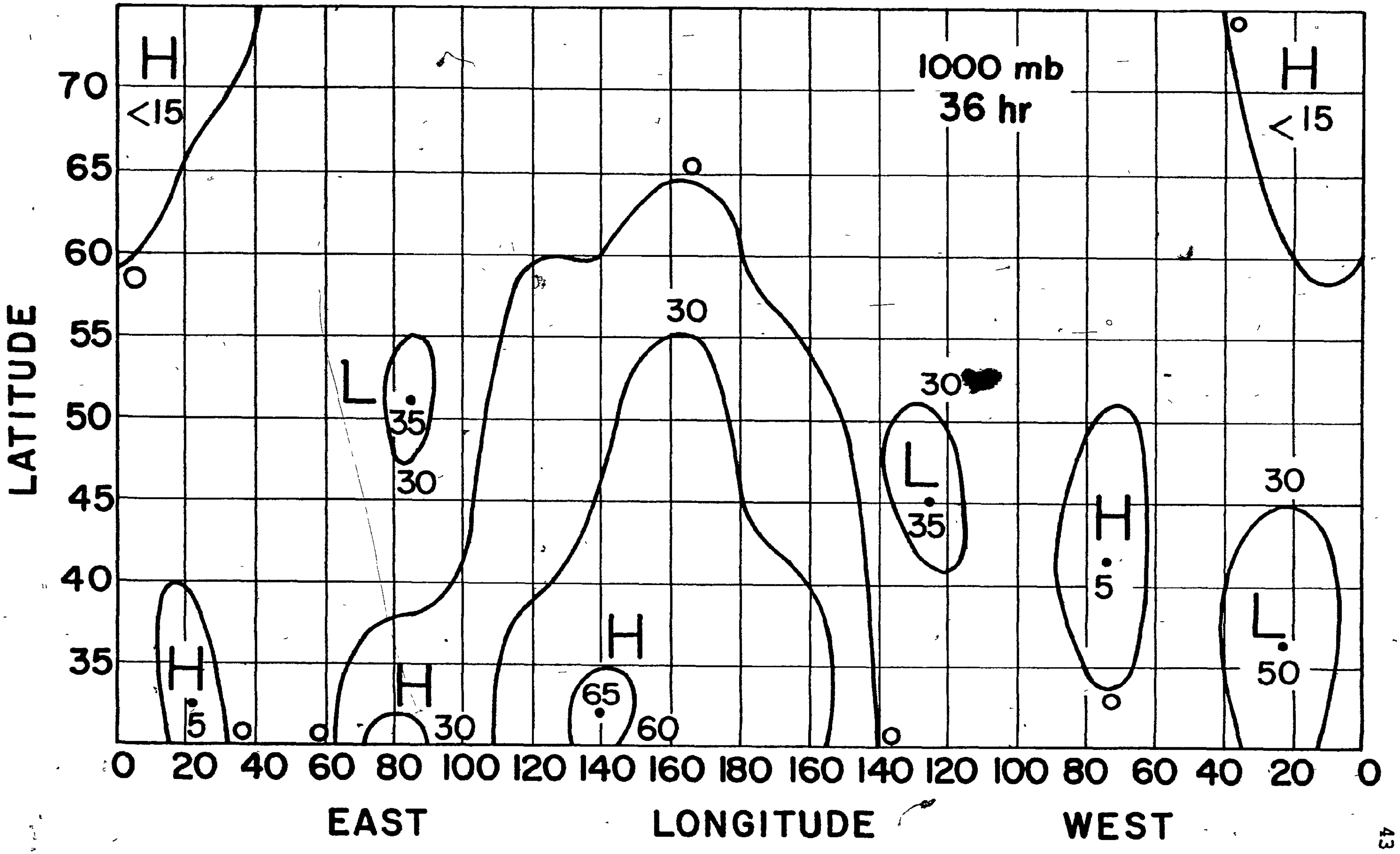

FIGURE (4.1) The 36 hour systematic planetary wave error at 1000 mb displayed on a map with unequal latitude and longitude scales.

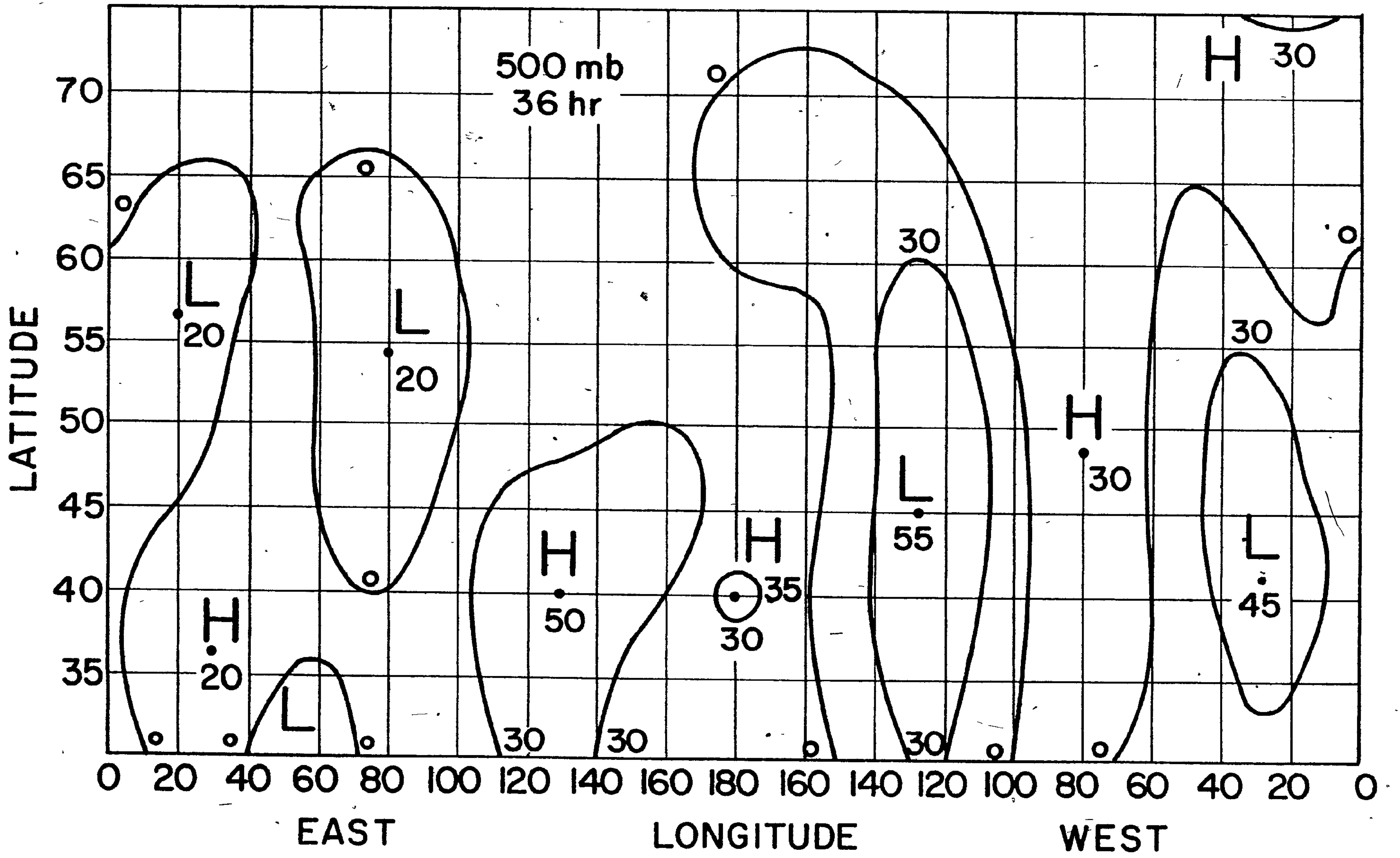

FIGURE (4.2) Same as Figure (4.1) except for the 500 mb height field.

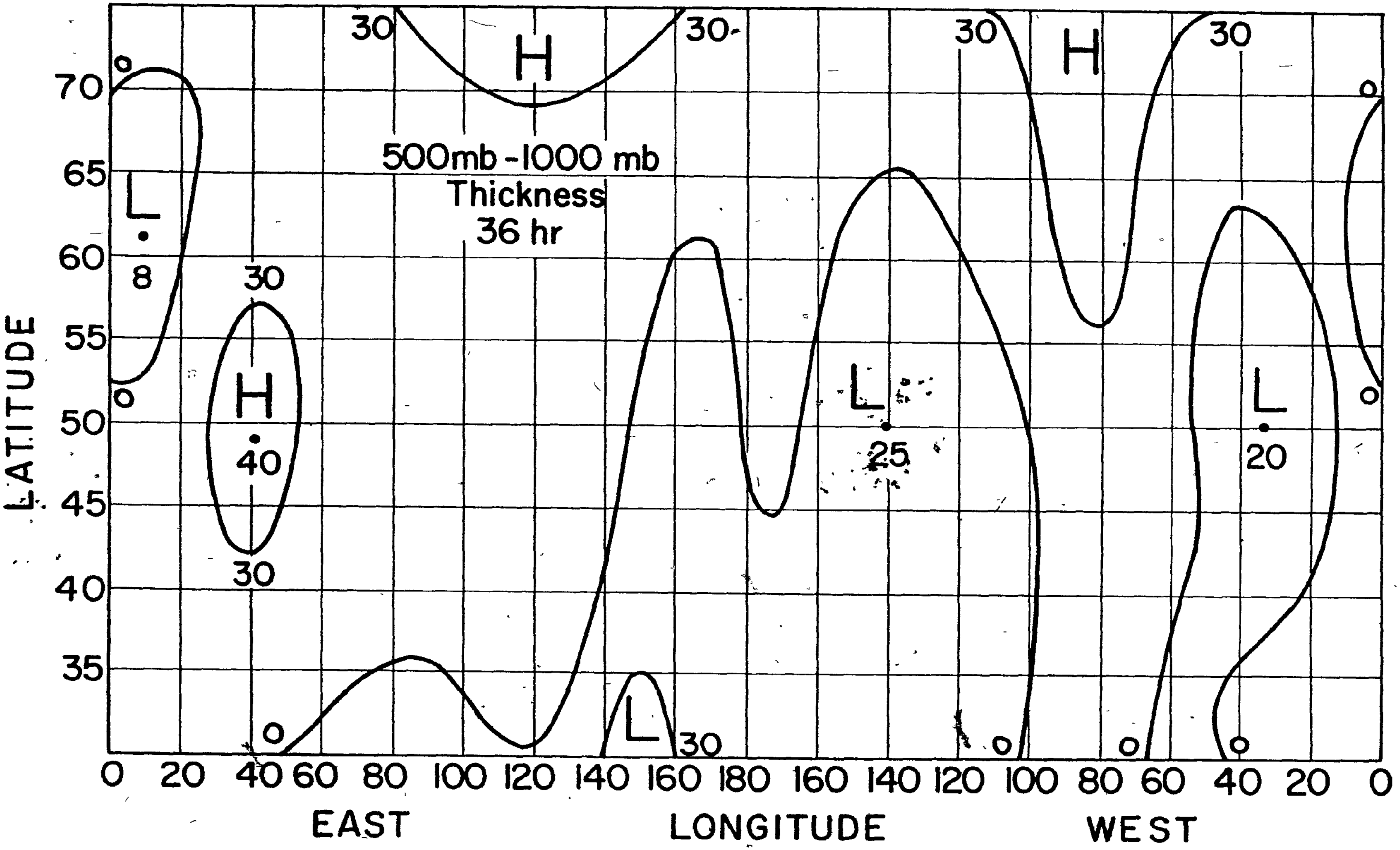

FIGURE (4.3) Same as Figure (4.1) except for the 1000 mb to 500 mb thickness field.

4.3 Synoptic Depiction of the Individual Case Errors

To see how the individual case errors in the planetary waves are manifested synoptically, the error field was compared to the verifying analysis for each of the fifteen cases. In constructing the error field and the corresponding verifying analysis, only the planetary waves were used. The fields were produced using

$$\Phi = \sum_{m=-5}^{5} \sum_{n=|m|}^{|m|+8} \Phi(m,n) Y_n^m ,$$

where $\Phi(m,n)$ = spherical harmonic coefficients of error field
or verifying analysis.

When the error field was superimposed on the 36 hour verifying analysis at 500 mb, a typical result as given in Figure (4.4) was produced. Over the chart as a whole, the individual errors are larger than the systematic errors given in the previous section. In the southern portion of the chart, the error centres lie on the trough and ridge lines indicating that the positions of the troughs and ridges are correct but the amplitudes are too small. In the northern portions of the chart, both the positions and amplitudes of the troughs and ridges are incorrect.

4.4 The Surface Pressure Substitution Experiments

To control a suspected barotropic mode, it was decided to substitute the observed planetary wave components of the surface pressure field for those components forecast during the running of the model. The surface pressure coefficients were substituted at every time step. Since the observed surface

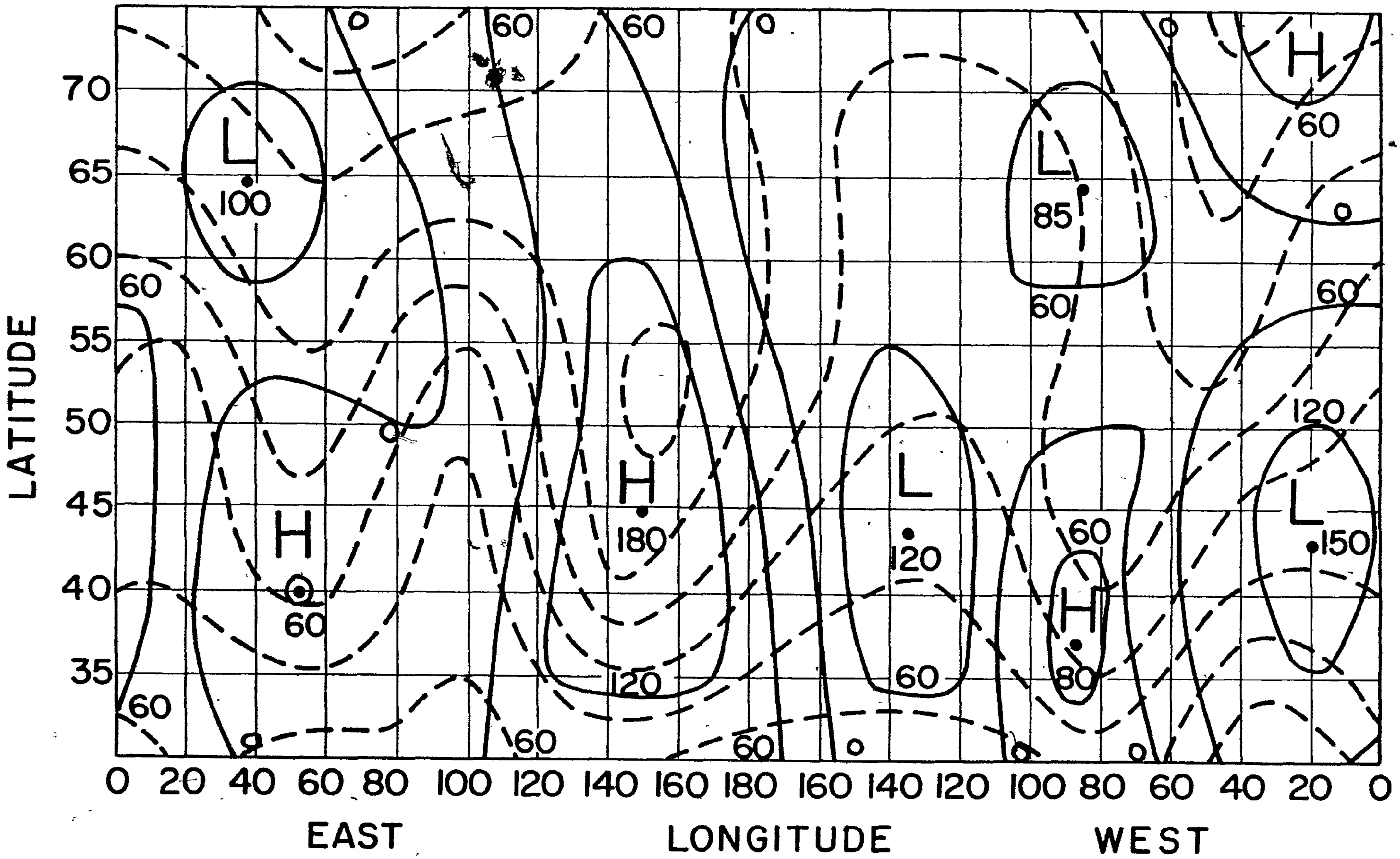

FIGURE (4.4) The 36 hour planetary wave error at 500 mb superimposed on the verifying 500 mb analysis.

pressure was available at 12 hour intervals only, linear interpolation was used to compute the intermediate values. During the first 12 hour period of a forecast, the interpolated surface pressures were obtained from

$$ {}^{N}q_n^m = {}^{0}q_n^m + \frac{N\Delta t}{12}\left[{}^{12}q_n^m - {}^{0}q_n^m \right], $$

where ${}^{N}q_n^m$ = surface pressure coefficient at the Nth time step,

${}^{0}q_n^m$ = observed initial surface pressure coefficient,

${}^{12}q_n^m$ = the observed surface pressure coefficient for 12 hours after the initial time,

Δt = time step in hours,

N = index of the time step.

A similar procedure was used for each of the succeeding 12 hour intervals. Only the first five non-zero spherical harmonic coefficients of zonal waves zero to five were substituted. These 30 coefficients represent less than one percent of the total prognostic coefficients in the model.

4.5 Results of the Pressure Substitution

The above experiment was performed on five cases, namely, cases 1, 3, 4, 5, and 11. The total absolute error for 36 hour forecasts of 500 mb geopotential and the 1000 mb to 500 mb thickness was obtained and compared to forecasts where no pressure substitution was made. The results for the 500 mb geopotential at 40° N versus wavenumber are given in Figure (4.5). With the exception of wavenumber four, all waves in the range of wavenumbers one to five have been substantially improved. In the range of wavenumbers from six to eight (where no substitution was made), a slight, though not convincing, improvement resulted. The results for the thickness are given in Figure (4.6) which shows little difference between the altered and unaltered forecasts.

The verifying analysis, the control (unaltered) forecast, and the altered forecast at 500 mb for each case were compared. In general, three improvements were noticeable. First, the amplitudes of troughs and ridges were increased but were still insufficient. Second, the position and depth of cold lows was improved and third, the occlusion process was improved although the centres of occluding cyclones were still too warm. Figures (4.7) to (4.10) give the maps for case 5 together with the initial 500 mb analysis.

4.6 Summary

From the results of this chapter, it can be seen that the planetary wave errors for a short range forecast are systematic. The systematic error pattern, resulting from the present model, is very similar to that obtained from a simple one-level barotropic model.

At mid-tropospheric levels, the effect of planetary wave error on synoptic charts is to give insufficient amplitudes to troughs and ridges. In addition, the pressure substitution experiments have shown that the planetary wave error has a marked barotropic character.

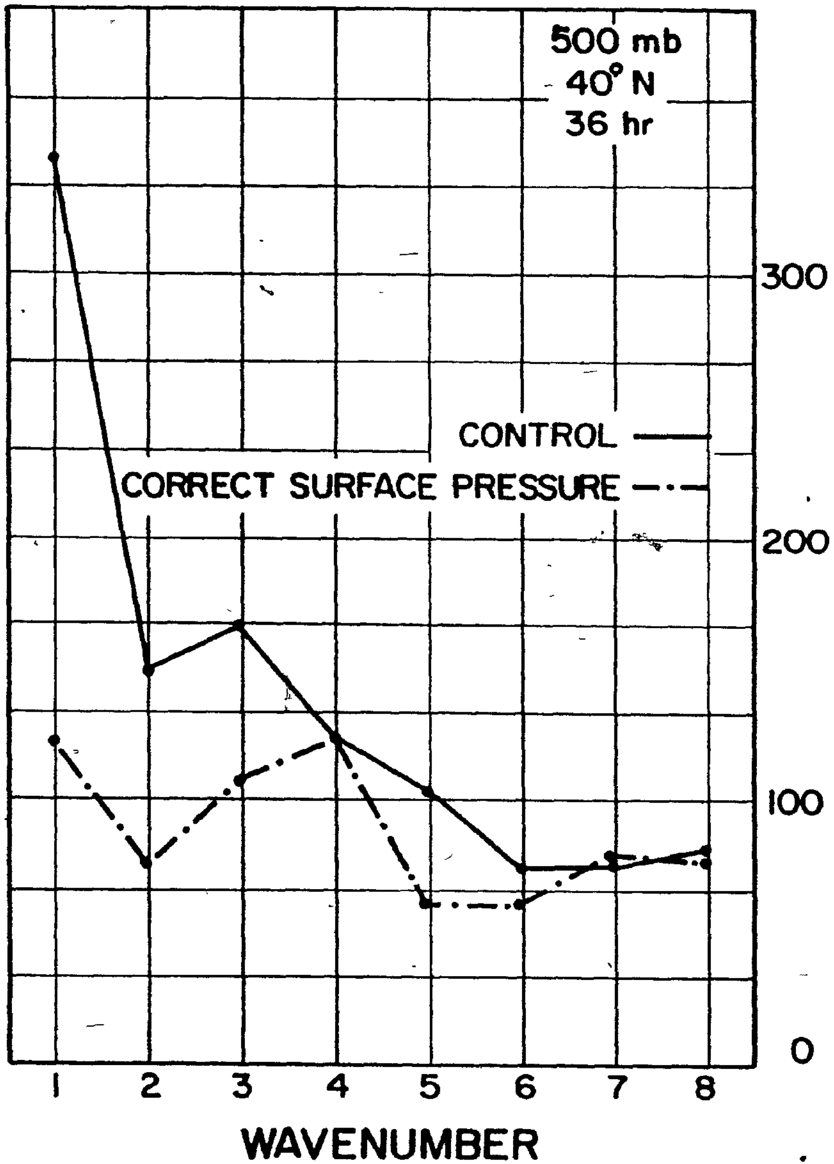

FIGURE (4.5) A comparison of the long wave error at 500 mb and 40° N between the control and surface pressure substitution forecasts.

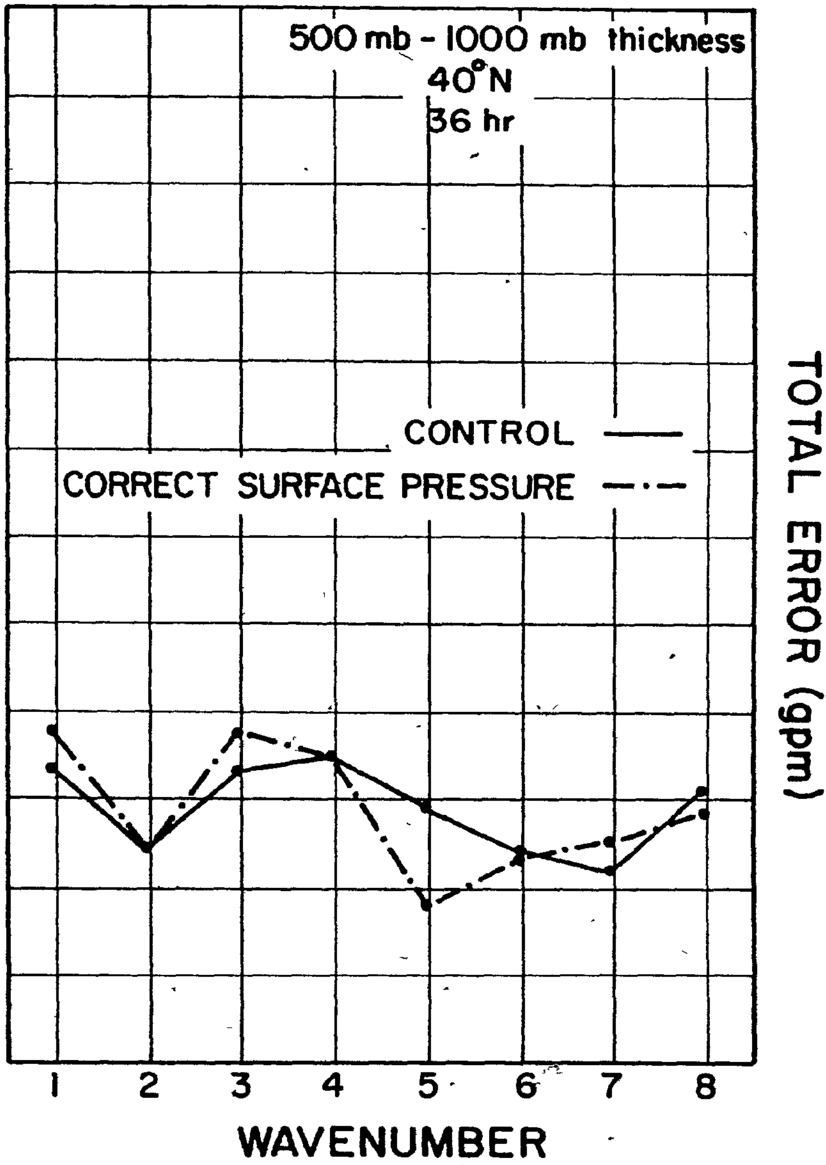

FIGURE (4.6) Same as Figure (4.5) except for the 500 mb to 1000 mb thickness at 40° N.

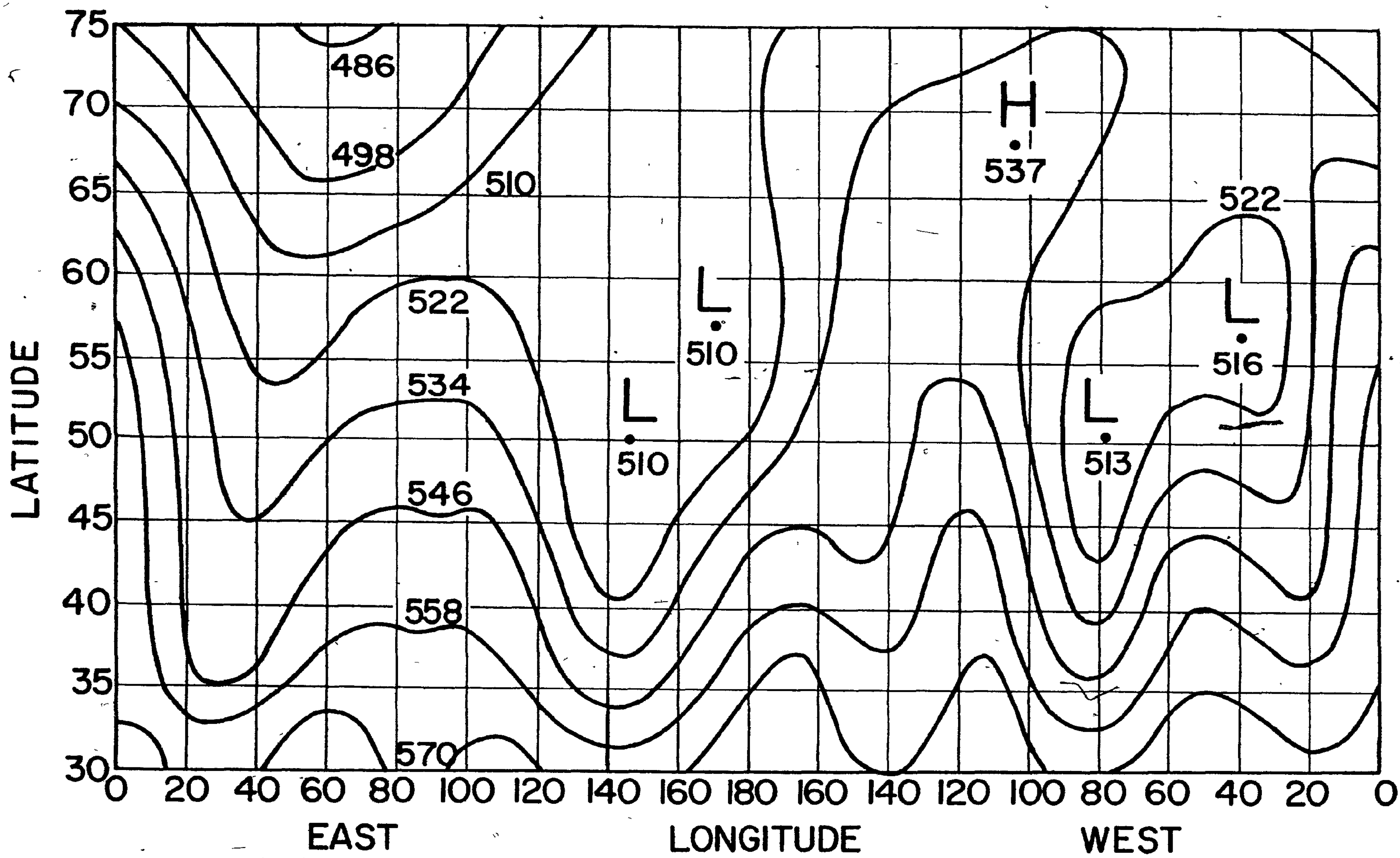

FIGURE (4.7) The initial 500 mb analysis for Case 5.

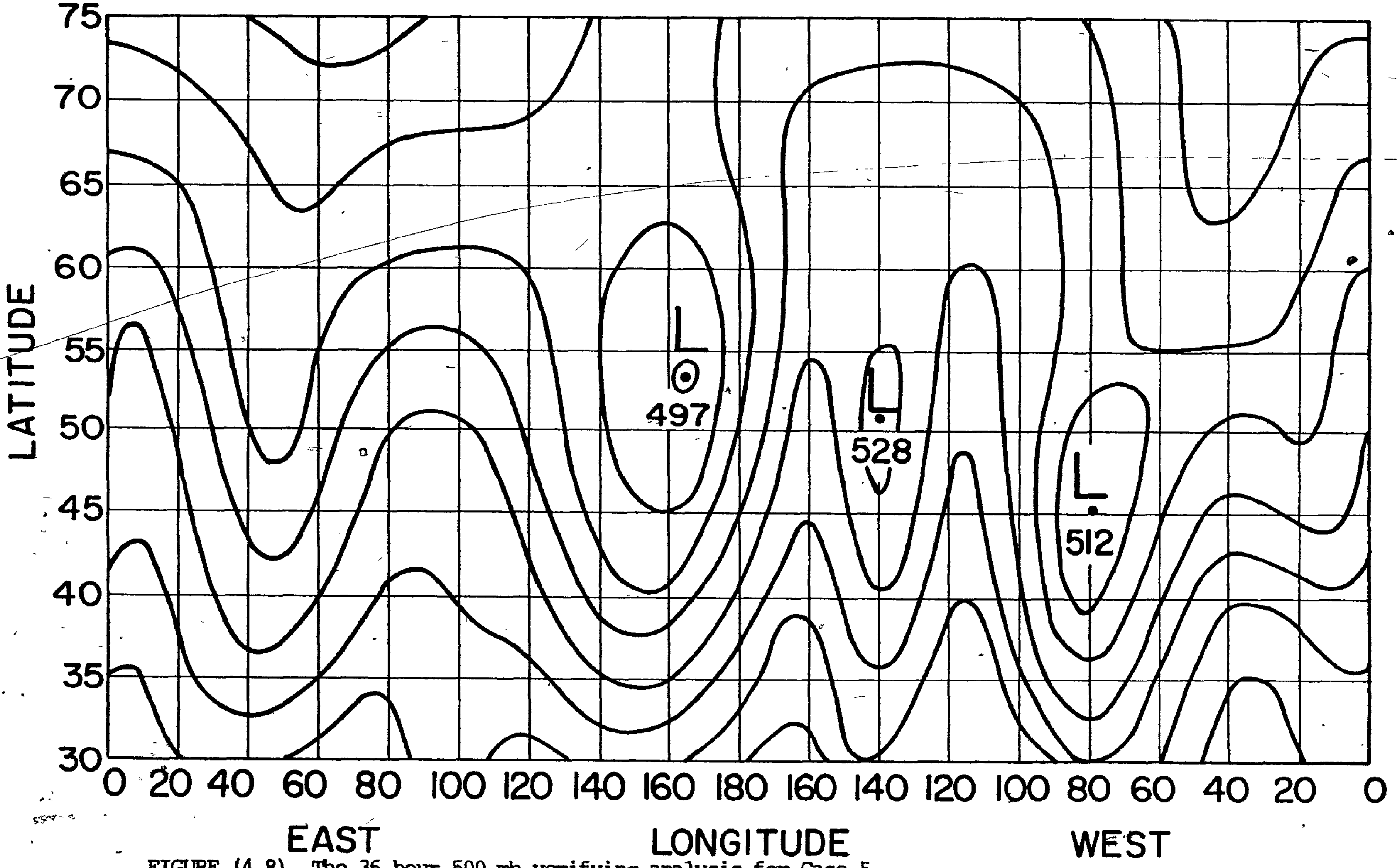

FIGURE (4.8) The 36 hour 500 mb verifying analysis for Case 5.

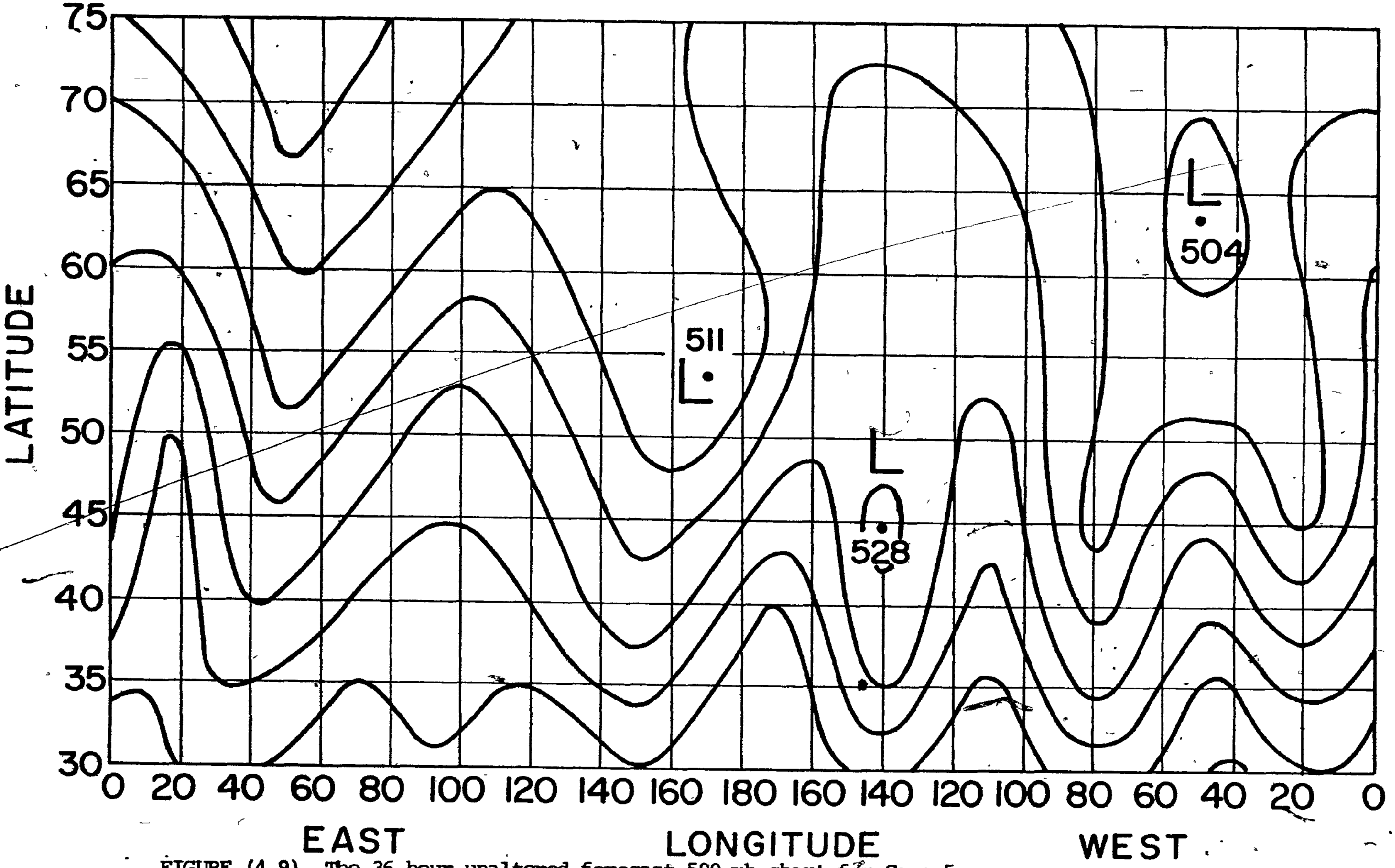

FIGURE (4.9) The 36 hour unaltered forecast 500 mb chart for Case 5.

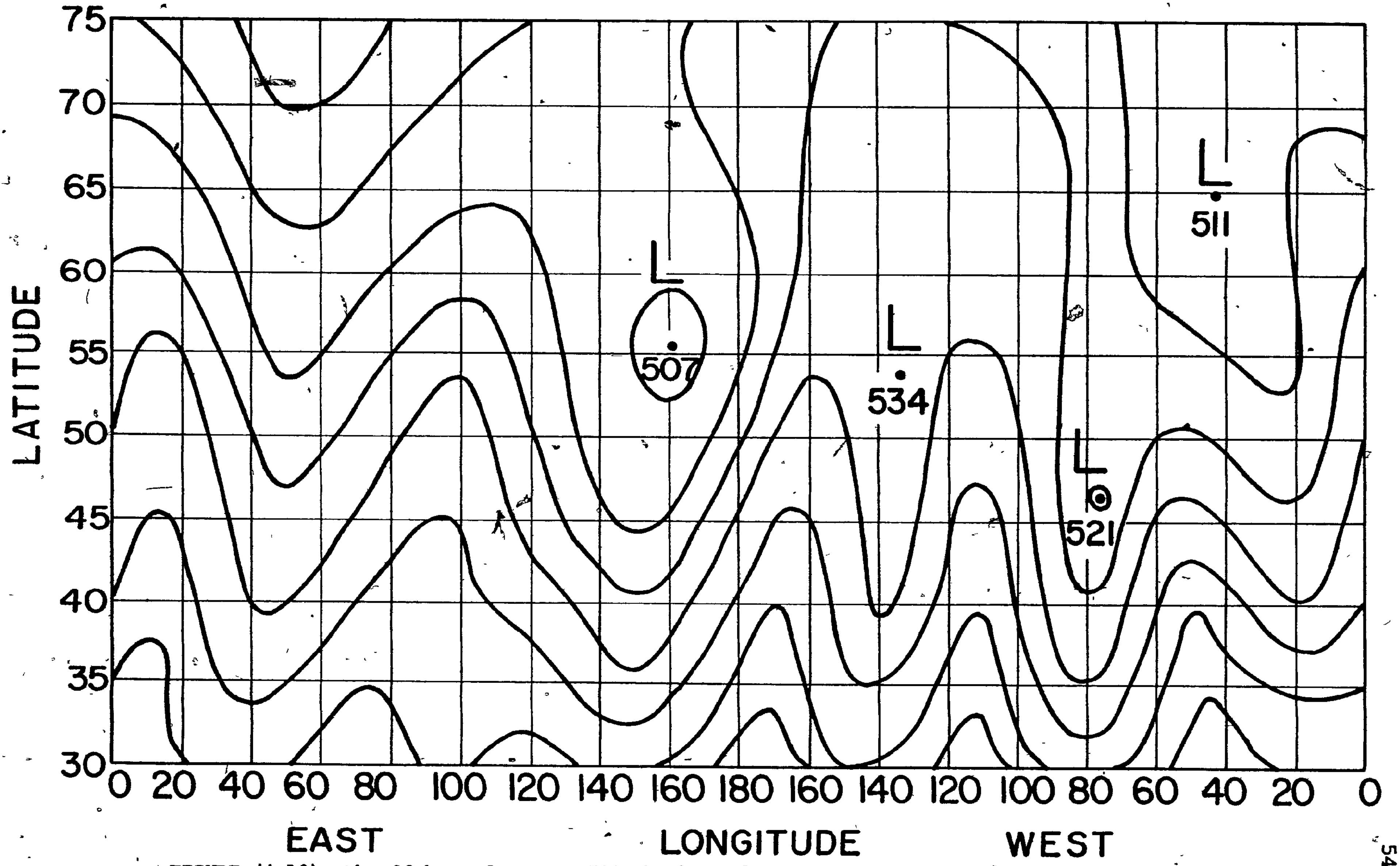

FIGURE (4.10) The 36 hour forecast 500 mb chart for Case 5 with surface pressure substitution.

CHAPTER 5

A DETAILED EXAMINATION OF THE PLANETARY WAVE ERRORS

5.1 Introduction

In this chapter, the planetary wave forecast error will be closely examined. A very convenient method of studying the properties of waves is by the use of a so-called "harmonic dial". Following the spirit of Section (3.4), the sum of a given spherical harmonic coefficient and its corresponding negative order can be written in the form

$$A(t)\cos\left\{m(\lambda-\delta(t))\right\} .$$

For the purpose of plotting a harmonic dial, $A(t)$ is the radius and $m\delta(t)$ is the angle in a polar co-ordinate system.

The line on which the polar angle equals zero represents the Greenwich Meridian and the polar angle increases to the east. If a given wave consists only of a stationary component; that is, if the amplitude and phase are independent of time, the wave will be represented as a single point on the harmonic dial. A wave that is completely transient in nature with constant amplitude and moving eastward at constant speed would be represented as a circle whose radius is equal to the wave amplitude and centered at the origin. If a wave consists of a combination of a transient and stationary part, it gives rise to a circle displaced from the origin. In this case, the co-ordinates of the centre of the circle represent the stationary components of the wave and the radius of the circle gives the amplitude of the transient part. The time taken for the transient part of the wave to complete one revolution of the circle is its period and clockwise motion is westward propagation and anti-clockwise motion is eastward propagation. Figure (5.1) displays this graphically (assuming "m" equals one). If a wave consists of more than one transient part, very complex patterns, difficult to interpret can result. Figure (5.2) shows a schematic harmonic dial of three transient waves with periods in a ratio of 1:-2:8 and amplitudes in a ratio of 1:2:5 respectively.

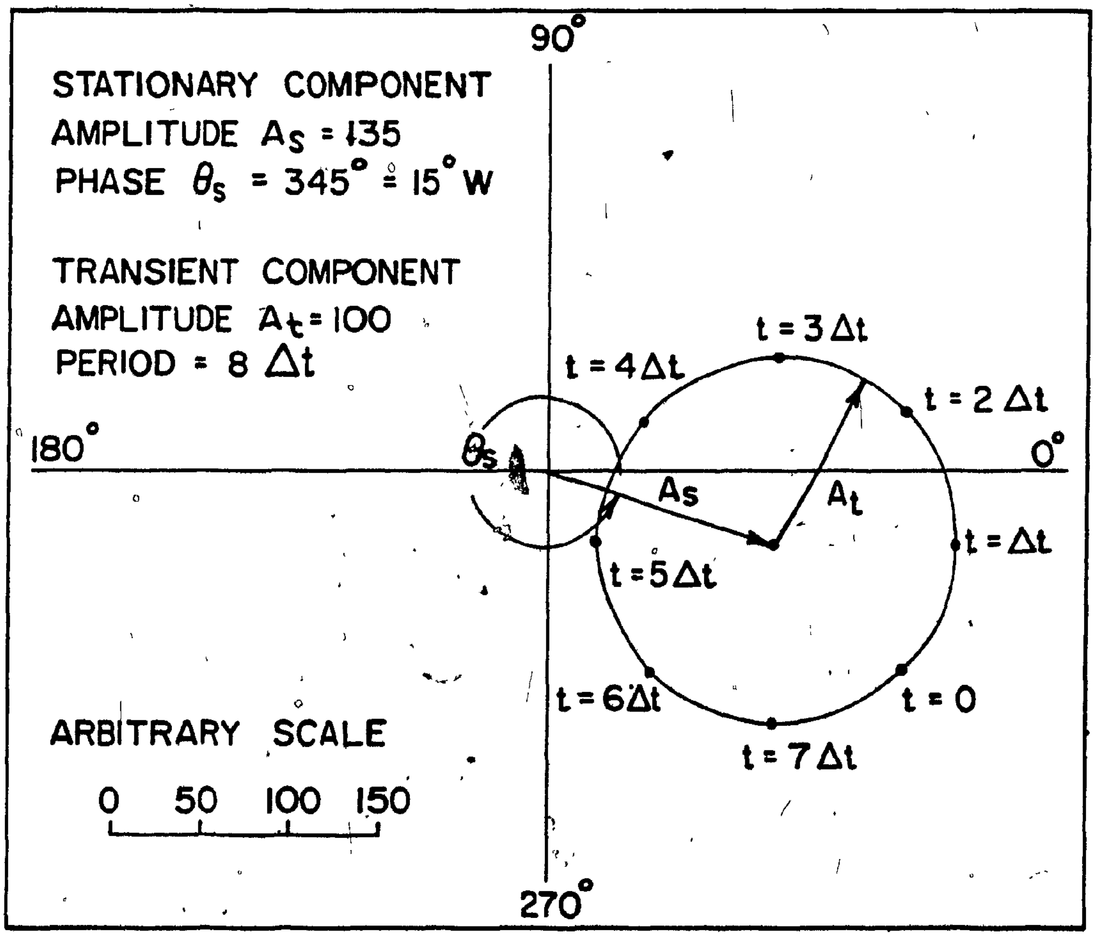

FIGURE (5.1) A simple schematic harmonic dial.

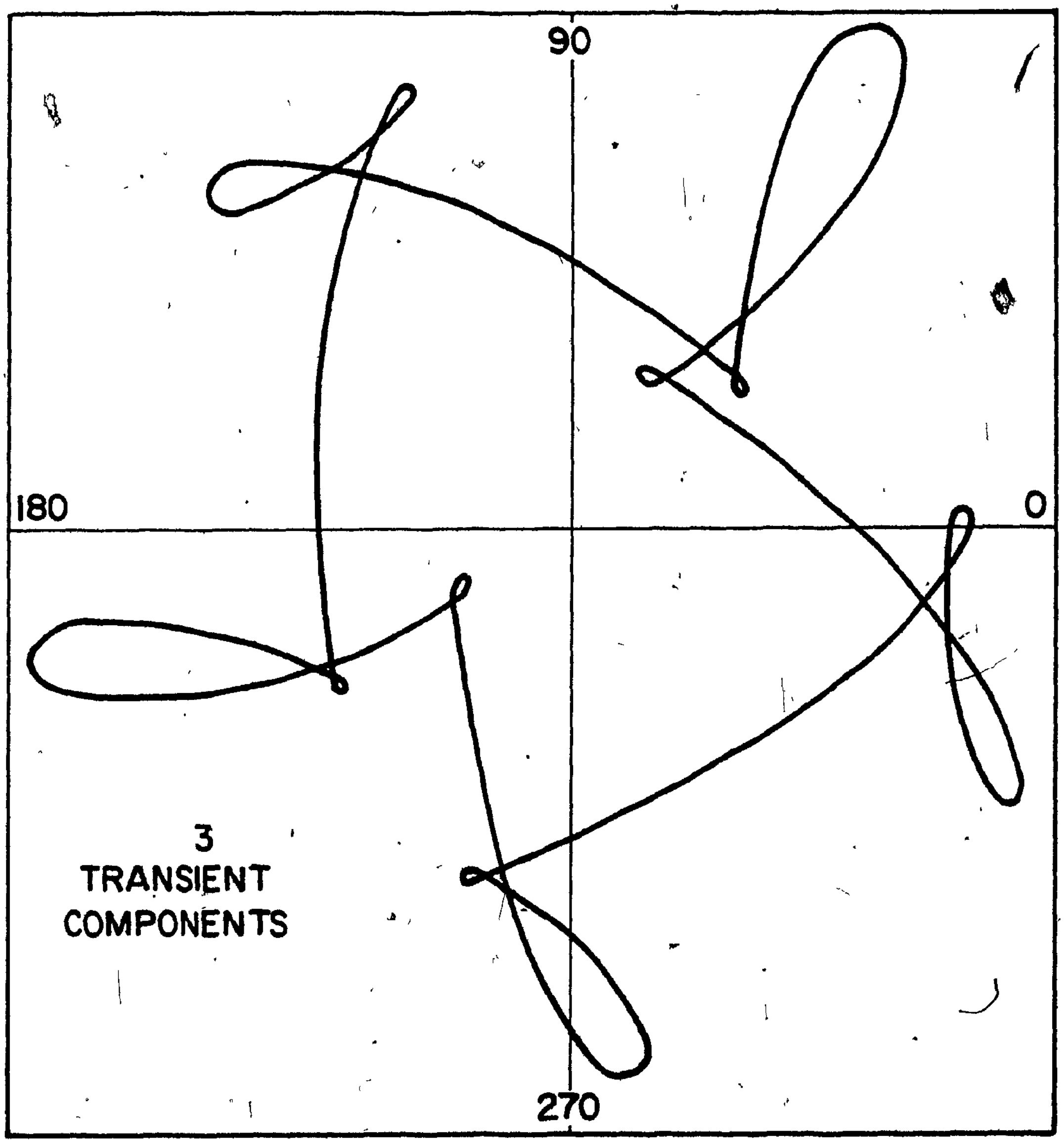

FIGURE (5.2) A complex schematic harmonic dial of three transient waves with periods in a ratio of 1:-2:8 and amplitudes in a ratio of 1:2:5 respectively.

5.2 Errors in the Spherical Harmonic Coefficients of Low Meridional Wavenumber

From the results of Section (3.5), it was noted that the coefficients (1,1), (2,2), (2,4), (3,3), and (4,4) of the geopotentials were not forecast in a satisfactory manner. Harmonic dials of the forecast spherical harmonic coefficients were plotted and it was noticed that the graphs of a given coefficient changed little from case to case. Figures (5.3) to (5.7) give the typical results for each of the above coefficients. The corresponding observations are included on the forecast harmonic dials. The observations showed little change from the initial position unlike the forecast which showed a large departure from the initial position.

It can be seen that the forecast waves consist of a stationary component and a westward moving transient component with a period of a few days. The approximate period of the transient part of each wave obtained by visual inspection is given in Table (5.1).

Height Field Coefficient	Period in Days
(1,1)	5
(2,2)	$3\frac{1}{2}$
(2,4)	$3\frac{1}{2}$
(3,3)	4
(4,4)	4

TABLE (5.1) Approximate periods of the transient components of the spherical harmonic coefficients of the 500 mb height field forecast with large error.

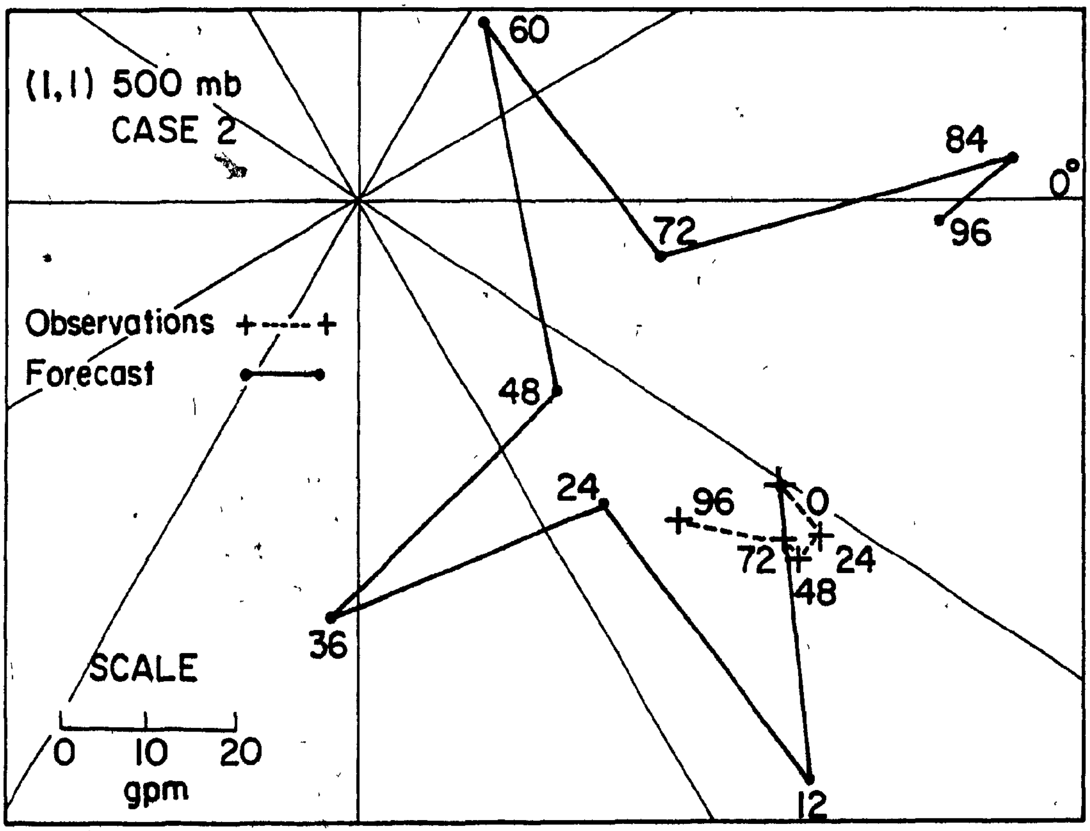

FIGURE (5.3) Harmonic dial of a typical forecast of spherical harmonic coefficient (1,1) of the 500 mb height field together with the verifying observations. Figures adjacent to the dots and crosses are the time in hours from the initial time.

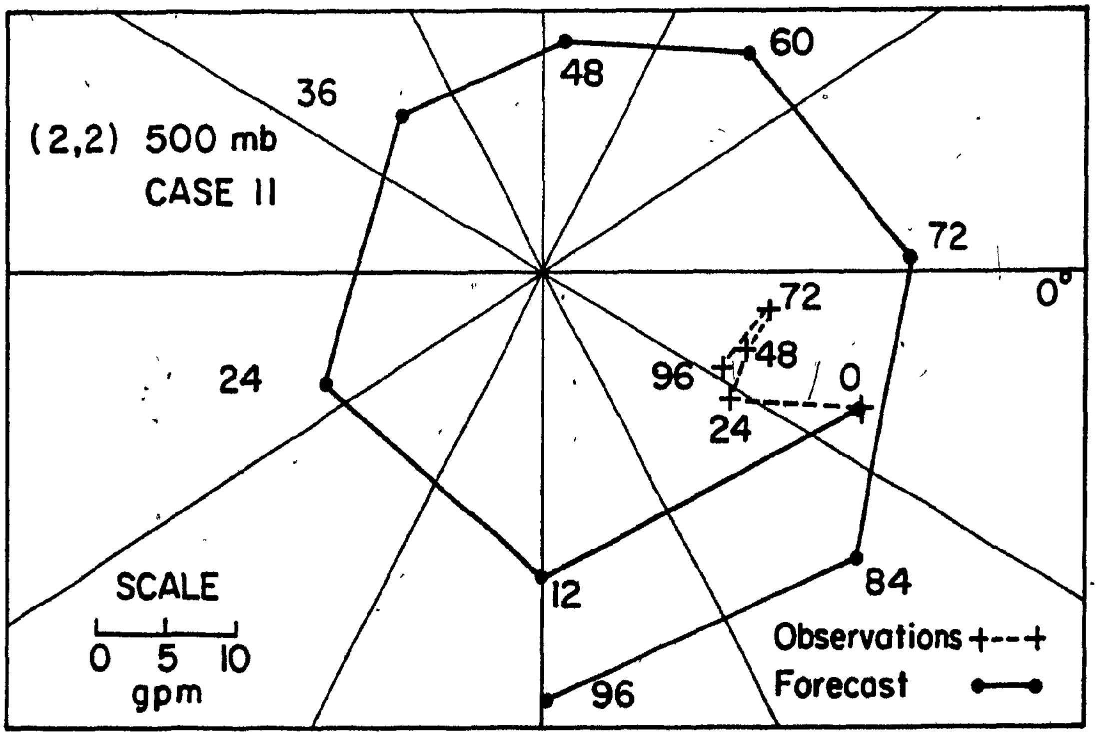

FIGURE (5.4) Same as Figure (5.3) except for coefficient (2,2).

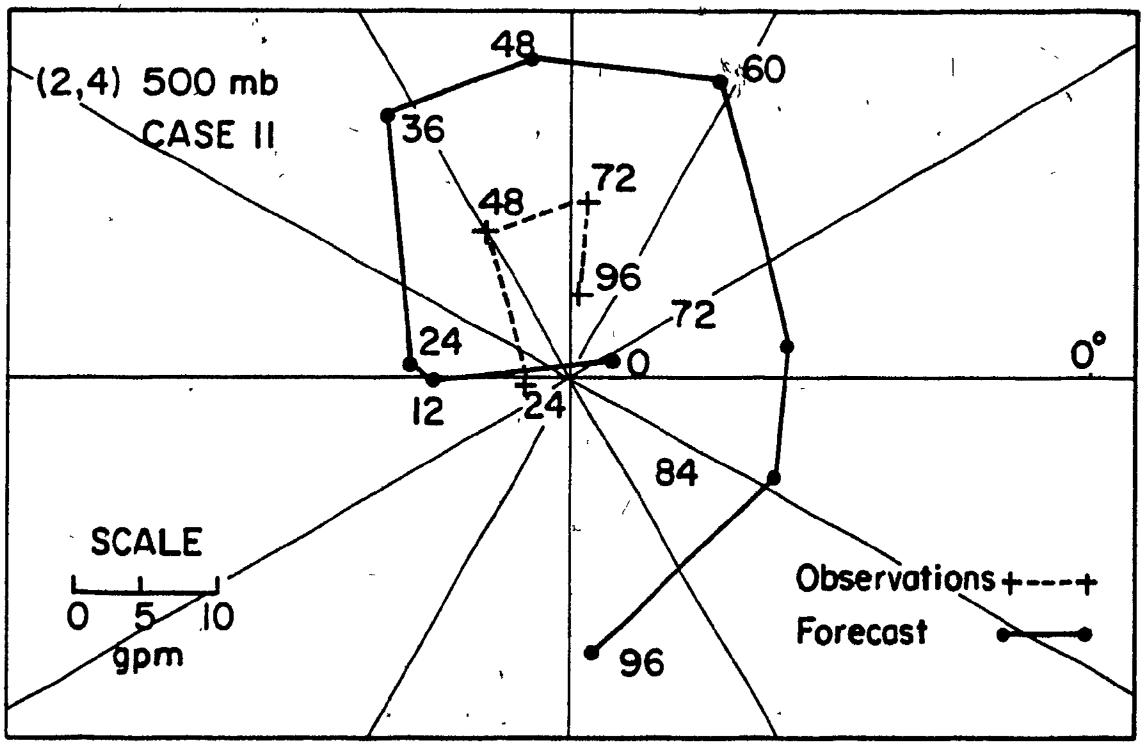

FIGURE (5.5) Same as Figure (5.3) except for coefficient (2,4).

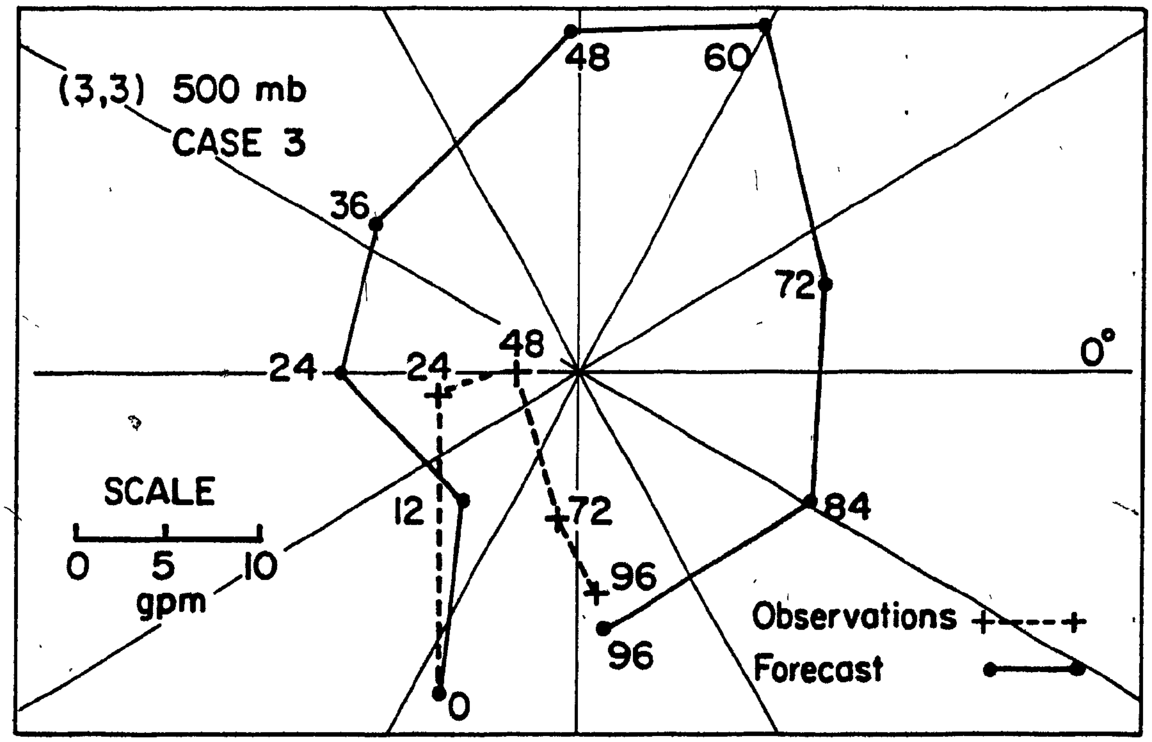

FIGURE (5.6) Same as Figure (5.3) except for coefficient (3,3).

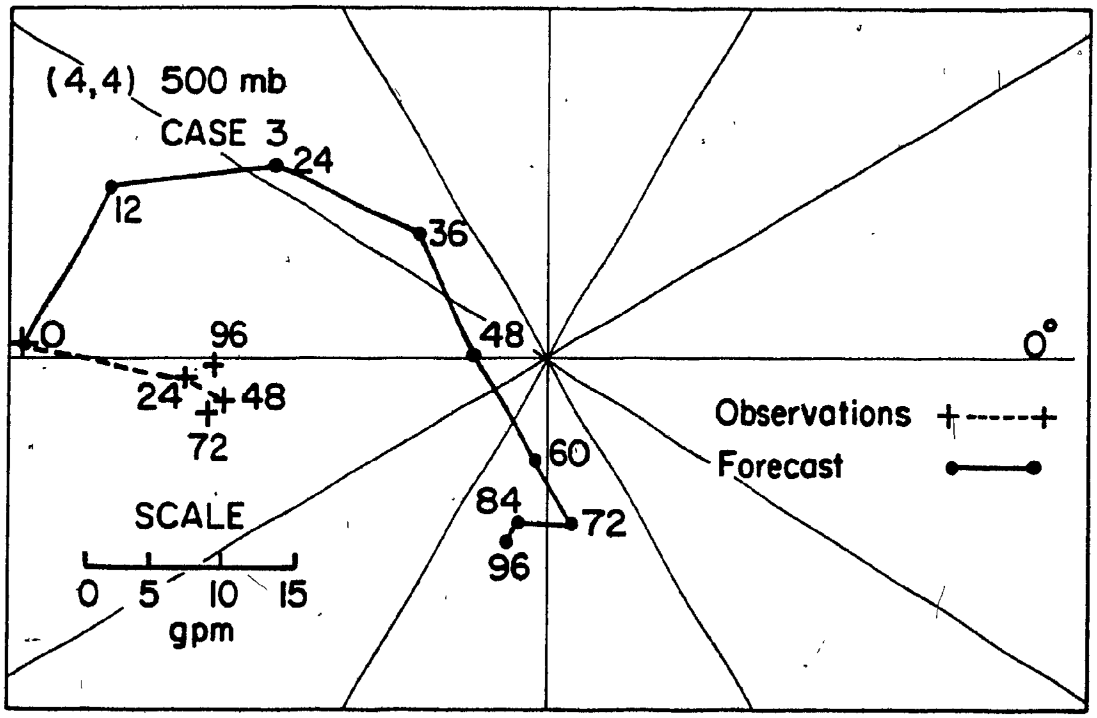

FIGURE (5.7) Same as Figure (5.3) except for coefficient (4,4).

It is evident especially from the harmonic dial of coefficient (1,1) that other transient components exist but are difficult to resolve due to the coarse sampling interval used (12 hours). If the dials are plotted with a time interval of 80 minutes, the existence of higher frequency components becomes evident. Figure (5.8) is a high resolution plot of Figure (5.3). High resolution dials for the other coefficients also show the existence of higher frequency components. A harmonic analysis was performed on the time series of the coefficients (1,1) and (2,2) with the results given in Table (5.2).

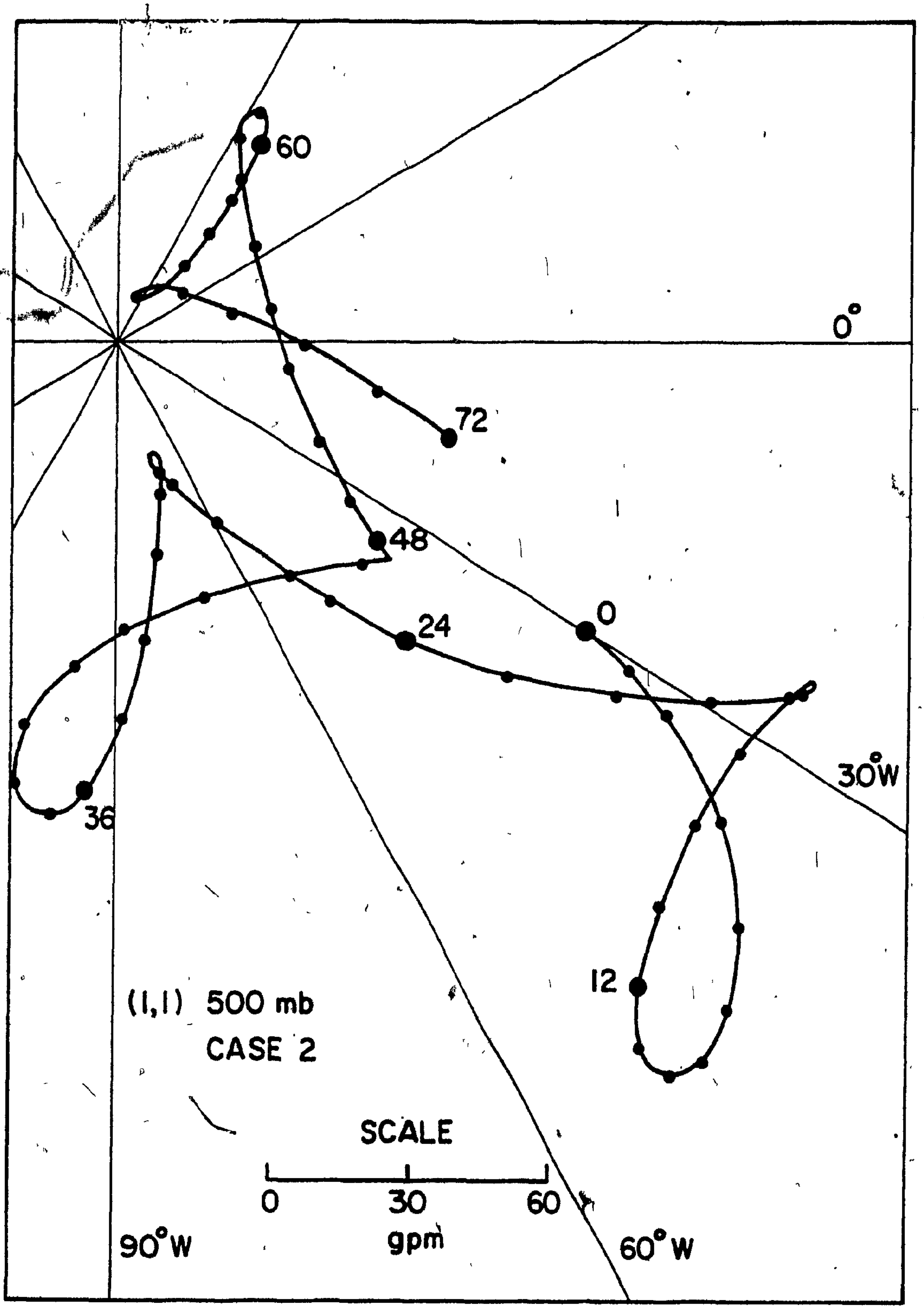

FIGURE (5.8) High time resolution harmonic dial of Figure (5.3). Small dots are placed at intervals of 80 minutes. Figures adjacent to the large dots give the time in hours from the initial time.

Height Field Coefficient	Wave	
	Period	Propagation
(1,1)	5 days	west
	33 hours	east
	13½ hours	west
(2,2)	3½ days	west
	17 hours	east
	11 hours	west

TABLE (5.2) The periods and directions of propagation of the forecast transient components of spherical harmonic coefficients (1,1) and (2,2) of the 500 mb height field.

Figure (5.9) gives the latitudinal structure of the three transient components of wavenumber one. The five day wave of wavenumber one has been observed in the real atmosphere by Madden and Julian (1972). The observed magnitude of the wave, however, is typically an order of magnitude less than that forecast by the model.

Following the development of Section (3.4), the structure of a transient component of a given zonal wave "m" can be written as

$$A_m = 2\sum_{n=m}^{m+R} A(m,n)\, P_n^m \cos(m\lambda - \delta_n^m - \omega t),$$

where A_m = amplitude of the transient component of wavenumber "m",

$A(m,n)$ = amplitude of the transient component in spherical harmonic coefficient (m,n),

δ_n^m = position of a ridge of the transient component at $t = 0$,

ω = frequency of the transient component.

Each of the non-zero spherical harmonic coefficients of wavenumber one was harmonically analysed to determine the amplitudes and initial phases of the 5 day, 33 hour, and the 13½ hour waves in order to determine their latitudinal structure. Significant amplitudes of each of the waves occurred only in coefficients (1,1) and (1,3); and, in addition, the phases of the waves were the same in both coefficients. Since the phases δ_n^m were independent of "n", the above becomes

$$A_m = \cos(m\lambda - \delta - \omega t)\, 2 \sum A(m,n) P_n^m .$$

Hence, the latitudinal structure, $A(\phi)$, of each of the three waves can be written as

$$A(\phi) = A(1,1) P_1^1 + A(1,3) P_3^1 .$$

The vertical structure of the forecast 5 day, 33 hour, and 13½ waves was determined and it showed that the phase was independent of height and that the amplitudes increased with height. Figure (5.10) gives the amplitude dependence on height of the 5 day wave. The other two waves are not included because they have a weak vertical amplitude structure.

Holton (1975) states that waves can be divided into two broad classes, external and internal. External waves have phase lines which are independent of height. For such waves, the energy density decays exponentially away from the levels of forcing. Internal waves have phase lines that tilt with height. This vertical tilt implies that such modes are able to transfer energy and momentum vertically.

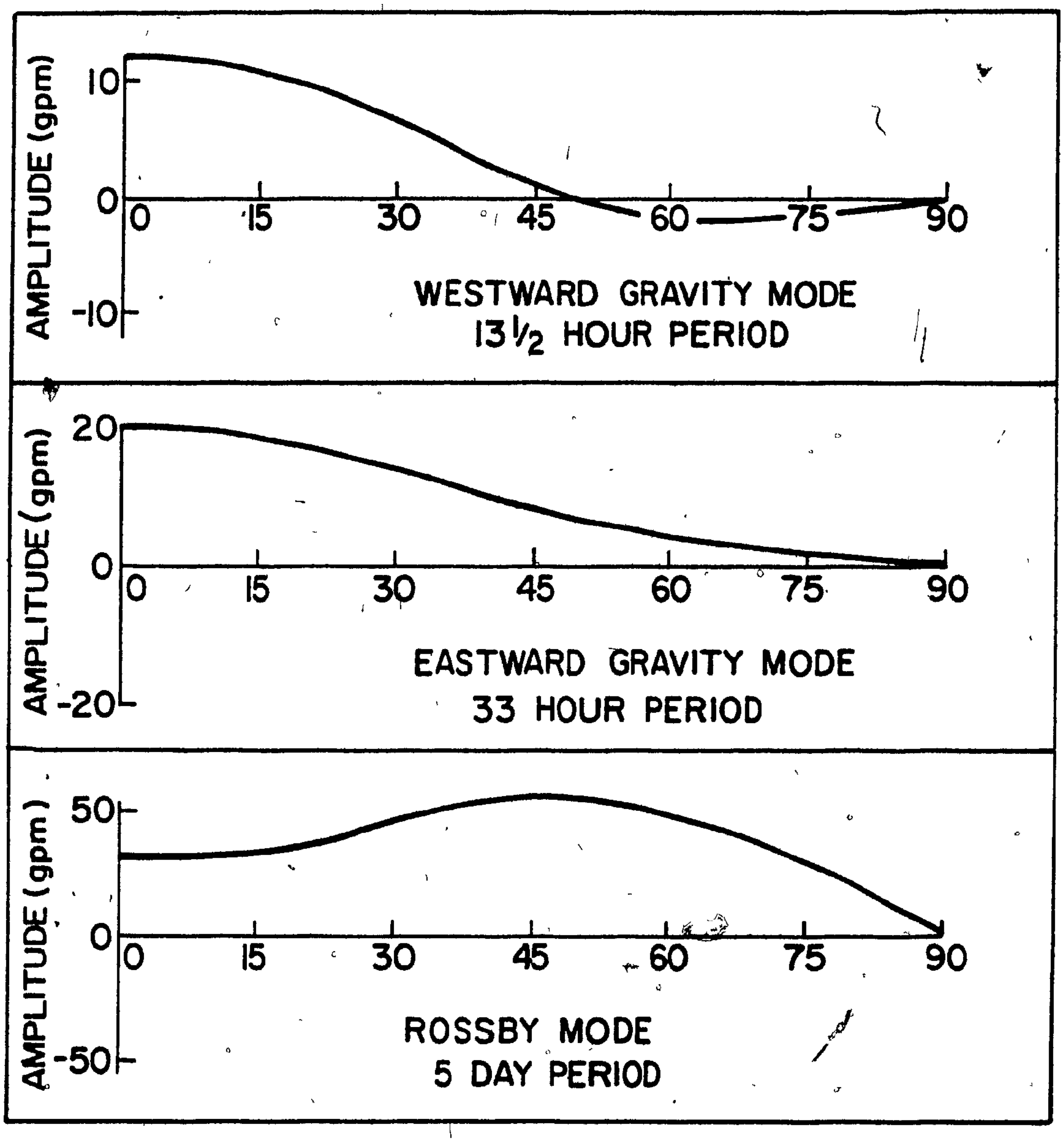

FIGURE (5.9) The latitudinal structure of the three external modes of wavenumber one for Case 3 at 500 mb. The abscissa is labelled in degrees of latitude.

The dependence of the average amplitude of these external modes on wavenumber can be inferred from Figure (4.5). If it is assumed that the external modes are completely removed by the surface pressure substitution, then the error reduction will be a measure of the average amplitudes of the external waves. Hence, they are strongest in wavenumber one and decrease with increasing wavenumber.

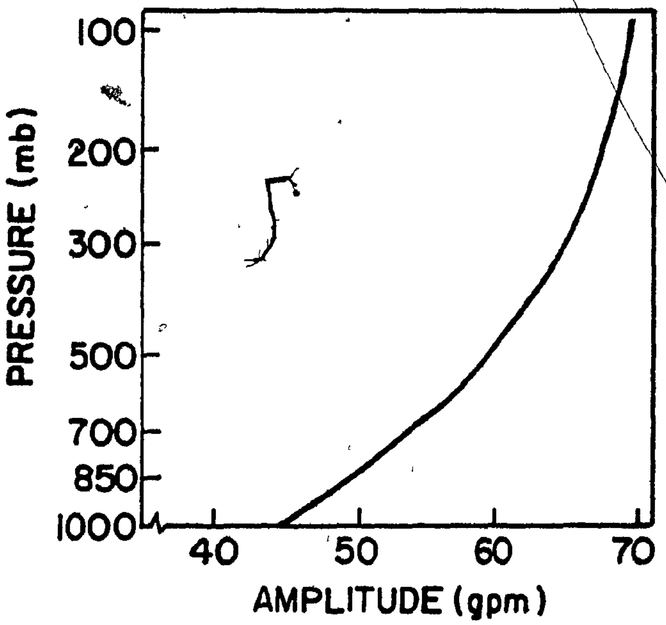

FIGURE (5.10) The vertical structure of the external Rossby mode.

In their paper, Madden and Julian also state that the horizontal structure of the 5 day wave is described by Laplace's Tidal Equations.

5.3 Laplace's Tidal Equations

Laplace's Tidal Equations describe the free motion of a thin layer of fluid of height H on the surface of a gravitating sphere which rotates with constant angular velocity Ω . The tidal equations are

$$\frac{\partial u}{\partial t} - 2\Omega v \cos\theta + \frac{1}{\sin\theta}\frac{\partial}{\partial\lambda}(gh) = 0, \quad (5\text{-}1)$$

$$\frac{\partial v}{\partial t} + 2\Omega u \cos\theta - \frac{\partial}{\partial \theta}(gh) = 0, \quad (5\text{-}2)$$

$$\frac{\partial h}{\partial t} + \frac{H}{\sin\theta}\left[\frac{\partial}{\partial\theta}\left(-v\sin\theta + \frac{\partial u}{\partial\lambda}\right)\right] = 0, \quad (5\text{-}3)$$

where u = zonal component of the fluid motion,

v = meridional component of the fluid motion,

t = time,

θ = colatitude,

h = perturbation amplitude of fluid height,

λ = longitude,

g = acceleration due to gravity.

Taylor (1936) showed that the above equations apply also to the free motions of a more general system in which the fluid is both stratified and compressible. In this case, a vertical structure equation defines an equivalent depth H which then allows equations (5-1) to (5-3) to be used.

If periodic solutions proportional to $\exp\{i(s\lambda - \sigma t)\}$ are desired, then the system of equations (5-1) to (5-3) can be written as

$$L(h) = \epsilon h, \quad (5\text{-}4)$$

where the linear operator L is

$$L \equiv \frac{1}{\alpha\sin\theta}\left[\frac{\partial}{\partial\theta}\left\{\frac{1}{\alpha^2-\cos^2\theta}\left(s\cos\theta - \alpha\sin\theta\frac{\partial}{\partial\theta}\right)\right\} + \frac{s}{\alpha^2-\cos^2\theta}\left(\frac{\alpha s}{\sin\theta} - \cos\theta\frac{\partial}{\partial\theta}\right)\right], \quad (5\text{-}5)$$

where $\epsilon = 4\Omega^2/gH$,

S = zonal wavenumber,

σ = frequency,

$\alpha = \sigma/2\Omega$.

Longuet-Higgins (1968) determined solutions of (5-4) over a wide range of the parameter ϵ. For positive equivalent depths, there are three classes of solutions - two gravity modes, one propagating eastward and the other propagating westward, and a Rossby mode propagating westward. The latitudinal structure of these eigenfunctions, which are termed Hough functions, shows that the energy tends to be concentrated in the equatorial regions.

For negative equivalent depths, which Longuet-Higgins shows are forced modes, there exist only two classes of solutions. One mode is eastward propagating and the other is westward propagating. In these cases, the energy is concentrated in the polar regions.

Figures (5.11) and (5.12) give the eigenfrequencies of the three lowest order symmetric free modes of the tidal equations for zonal wavenumbers one and three.

5.4 The Specific Nature of the External Modes

For an isothermal unbounded atmosphere at rest, there is a unique equivalent depth given by the vertical structure equation. The equivalent depth is

$$H = \frac{\gamma R T_0}{g}, \qquad (5\text{-}6)$$

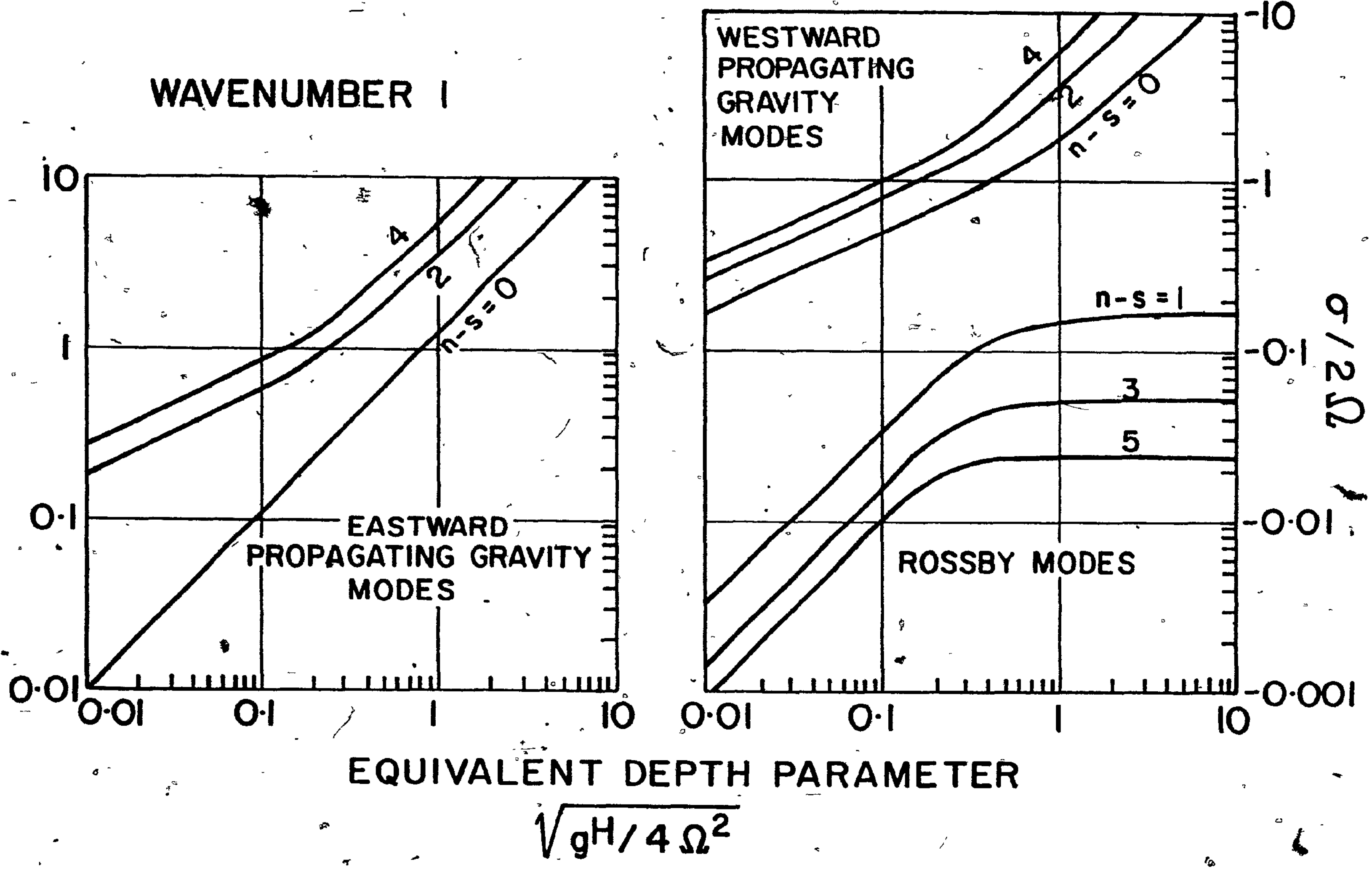

FIGURE (5.11) Eigenfrequencies of the three lowest order symmetric free modes of Laplace's Tidal Equations for wavenumber one. The order of the modes increases with increasing (n-s). From Longuet-Higgins (1968).

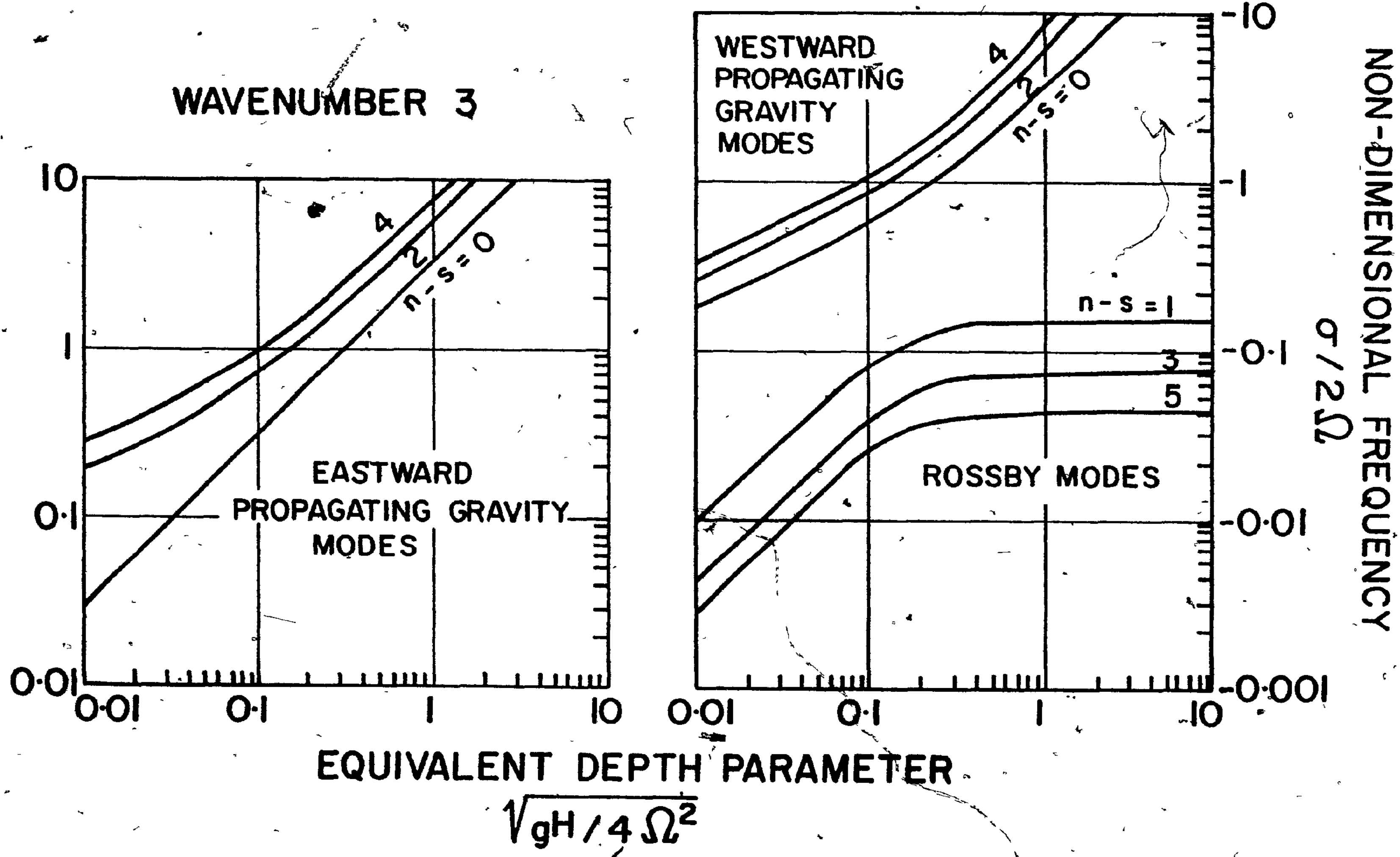

FIGURE (5.12) Same as Figure (5.11) except for zonal wavenumber three.

where H = equivalent depth,

γ = ratio of the specific heats for air,

R = gas constant for dry air,

T_0 = temperature,

g = acceleration due to gravity.

For a temperature of 300 K, the equivalent depth is 10.5 km which gives an equivalent depth parameter of 0.34. If Figure (5.11) is entered with this value, a period of five days is obtained for the Hough mode $S = 1$, $n = 2$. This mode is the lowest order symmetric Rossby mode.

The latitudinal structure of the above Hough function corresponding to an equivalent depth of 10.5 km is similar to the observed structure of the forecast 5 day wave (cf. Figure (5.9)).

The period of the eastward propagating gravity wave, obtained from Figure (5.11) with an equivalent depth of 10.5 km, is approximately 32 hours and the period obtained for the westward travelling gravity wave is about 14 hours. The latitudinal structure of both these modes agrees with the forecast latitudinal structure given in Figure (5.9). If the same equivalent depth is used to determine the periods of the modes for zonal wavenumbers two to four, periods very close to those given in Tables (5.1) and (5.2) result.

Because of the above, it is concluded that the major contributor to the planetary wave error in the short range period (0 to 48 hours) consists of spurious external modes - one Rossby wave and two gravity waves with an equivalent depth of approximately 10 km.

5.5 The Nature of the Medium Range Forecast Error

In Section (3.3), it was observed that the character of errors at 96 hours was considerably different from that observed at 36 hours. The planetary wave error, resulting from the external modes, reaches a maximum in the 36 to 48 hour period and then begins to decrease. Hence, another class of errors is responsible for the continued error growth after this period.

The latitudinal structure of the total error (defined in Section (3.2)) was examined for the set of 96 hour forecasts of zonal wavenumber one at 1000 mb. The results are given in Figure (5.13) together with comparative results for 36 hours. The 36 hour error curve strongly resembles the latitudinal structure of the external modes, showing the dominance of this error. At 96 hours, the error structure is completely changed. The error is a maximum at 70° N and the total error at 40° N has decreased in the period from 36 to 96 hours. Figure (5.14) gives the latitudinal dependence of the 96 hour 1000 mb height field error phases for zonal wavenumber one. At 70° N, where the total error is largest, there are two distinct clustering points. In more southerly latitudes, where the total error is smaller, the clustering is less pronounced. With the exception of two cases, there is a marked eastward or westward tilt with increasing latitude in the error phases. There does not appear to be any seasonal preference for a westward or eastward tilt of the phases.

Figure (5.15) shows the vertical structure of the 36 hour and the 96 hour total error for zonal wavenumber one at 70° N. The 96 hour curve shows an error minimum at 500 mb. Above this level, the errors increase rapidly with height, reaching a maximum at 100 mb. Figure (5.16) gives the vertical structure of the corresponding error phases. Even at 96 hours, the phases cluster at all levels, showing that the errors are very systematic. The typical wavenumber one error wave slopes westward with height to 300 mb and above this level slopes eastward with height.

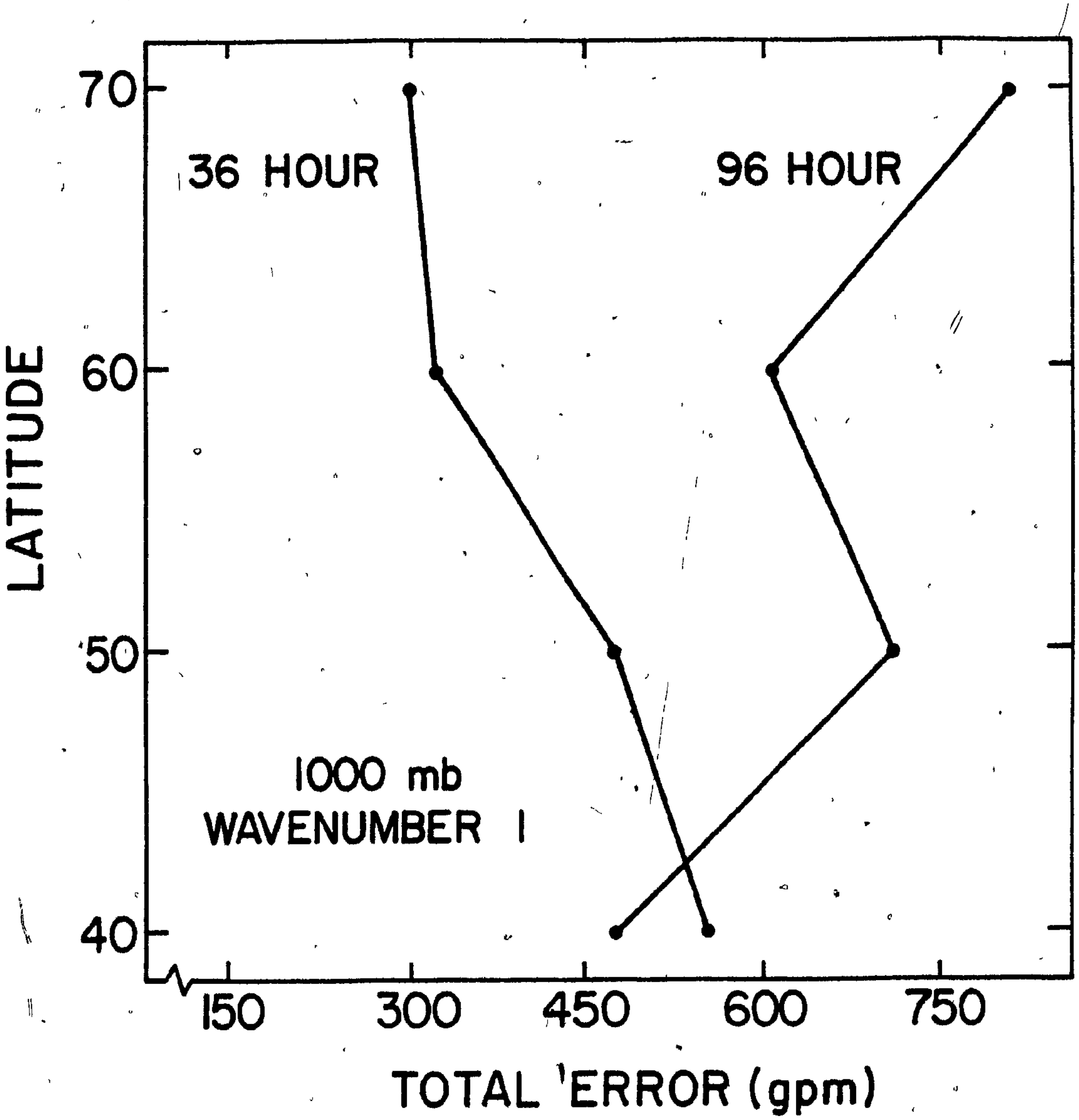

FIGURE (5.13) Latitudinal structure of the 36 hour and 96 hour total error for wavenumber one at 1000 mb.

Similar results exist for the remaining planetary waves. There is a trend for the latitudinal error maximum to move southward with increasing

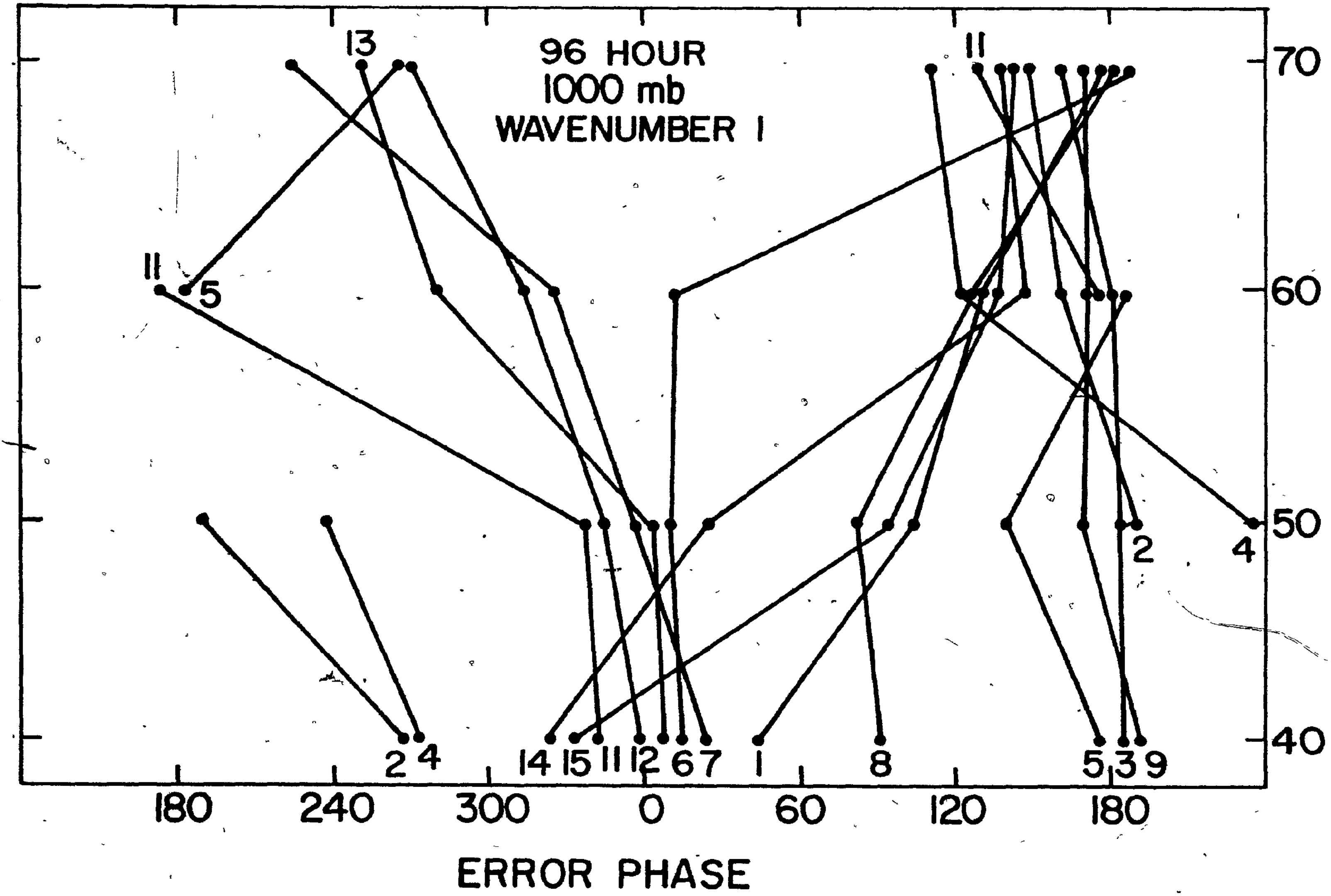

FIGURE (5.14) The latitudinal structure of the 96 hour error phases for wavenumber one at 1000 mb. Figures above or below the profiles are the case numbers.

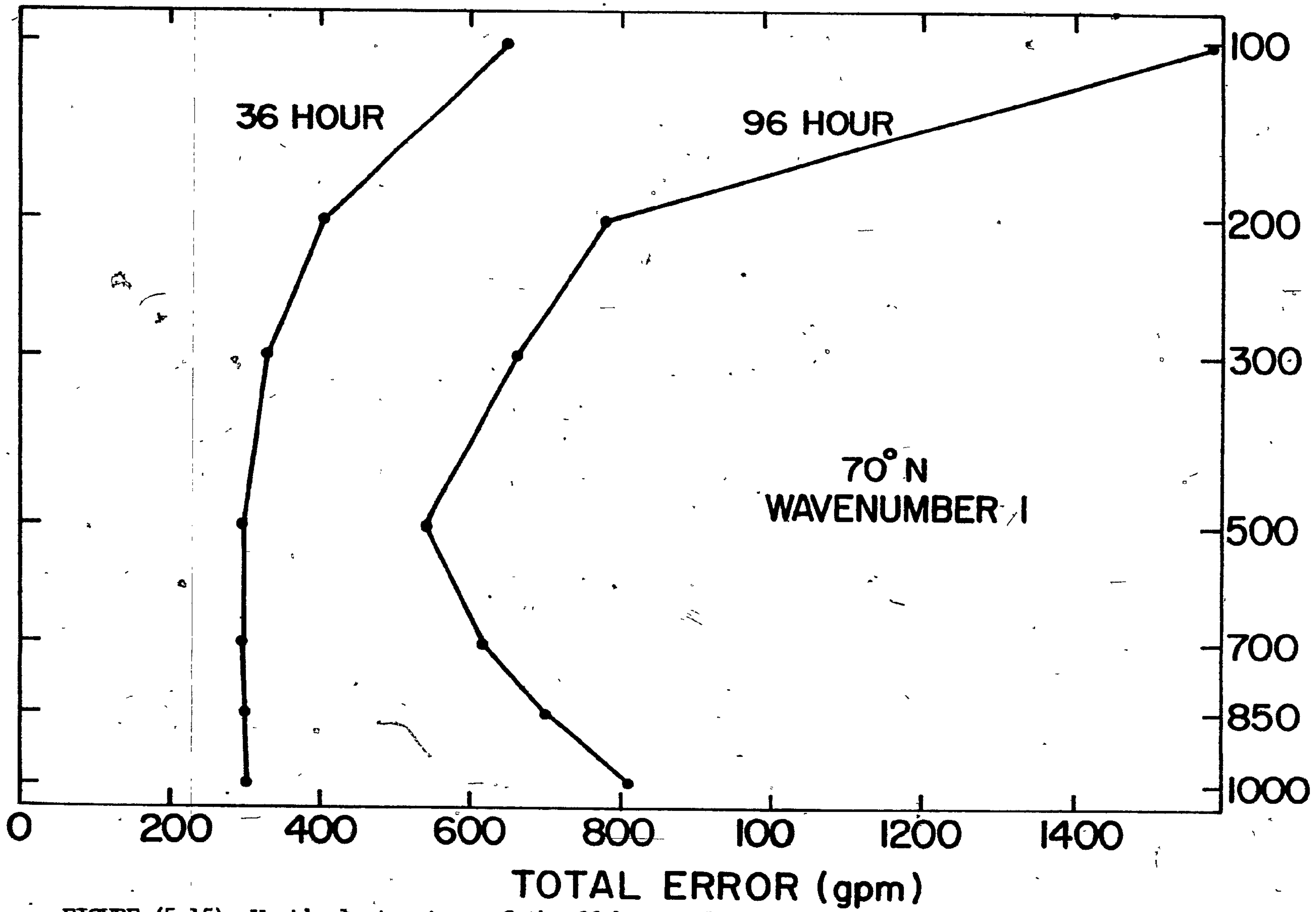

FIGURE (5.15) Vertical structure of the 36 hour and 96 hour error amplitudes for wavenumber one at 70° N.

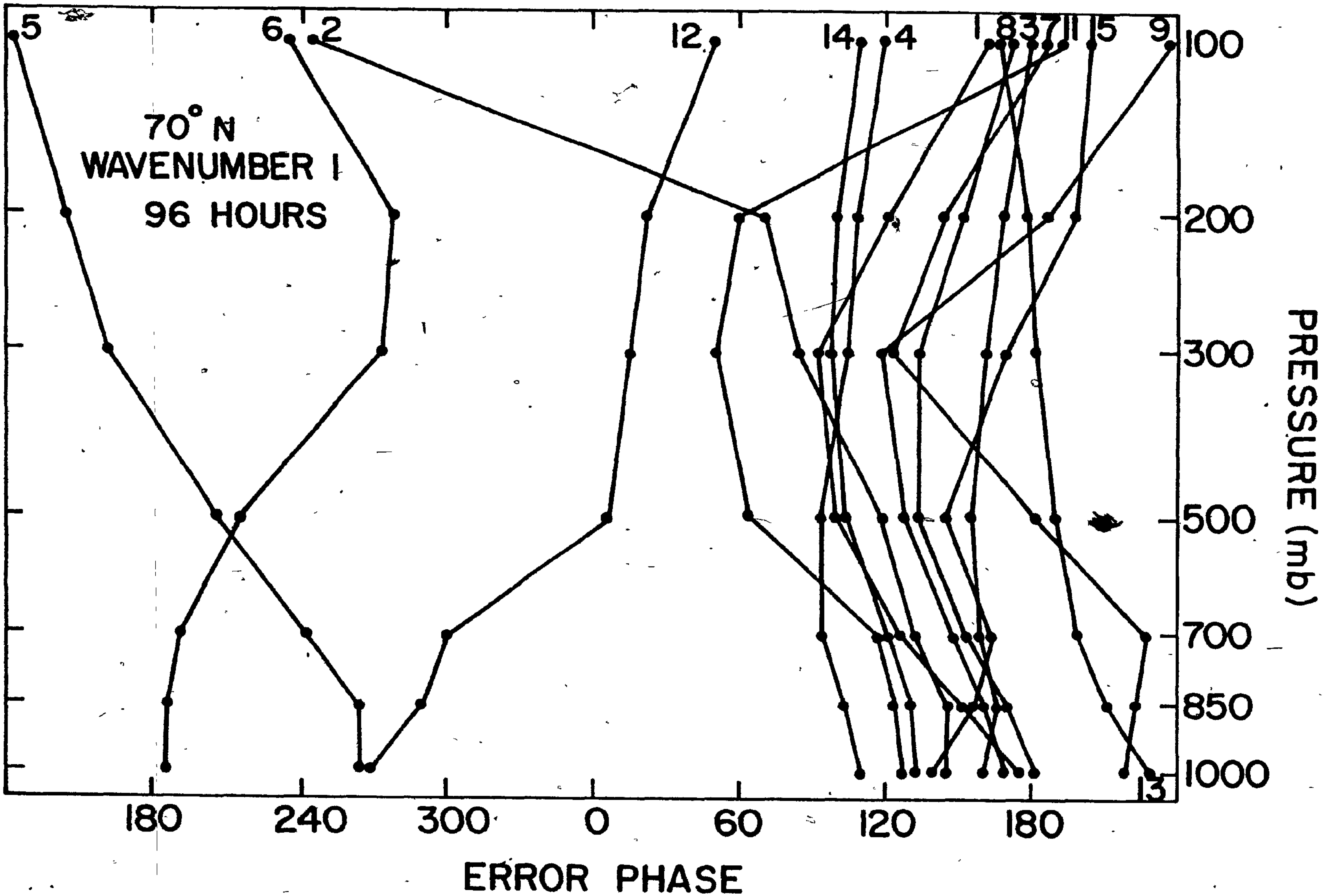

FIGURE (5.16) Vertical structure of the 96 hour error phases for wavenumber one at 70° N. Figures above each profile are the case numbers.

wavenumber, reaching 50° N for wavenumber five. The error maximum in the vertical, found at 100 mb in zonal wavenumber one, decreases in height with increasing wavenumber and a similar trend exists for the vertical error minimum. The wavenumber five profile has its maximum at 300 mb and its minimum at 850 mb. The systematic nature of the error pattern becomes less pronounced with increasing wavenumber.

5.6 Behavior of the Forecast Stationary and Transient Components of the Planetary Waves

When examining the spectral coefficients by means of harmonic dials, it was noticed that the forecast stationary components were considerably different from the observed stationary components. To investigate this effect more closely, a 240 hour forecast of case 3 was made. The phases and amplitudes of the stationary components obtained subjectively from the harmonic dials were compared to the observed stationary components. Figure (5.17) shows the results of the comparison for the coefficient (2,4) of the height field. From the diagram, it is evident that the phases of the forecast and observed stationary components do not differ greatly from each other. The forecast amplitudes, however, are only about one-half the observed values.

The incorrect forecast stationary components will cause observations to be incorrectly partitioned between stationary and transient parts. As a result, the model is able to generate an unnaturally large transient component.

The behavior of the forecast transient component of coefficient (1,1) of the 500 mb height field over a period of ten days is given in Figure (5.18). From this, it can be seen that the amplitude of the transient component

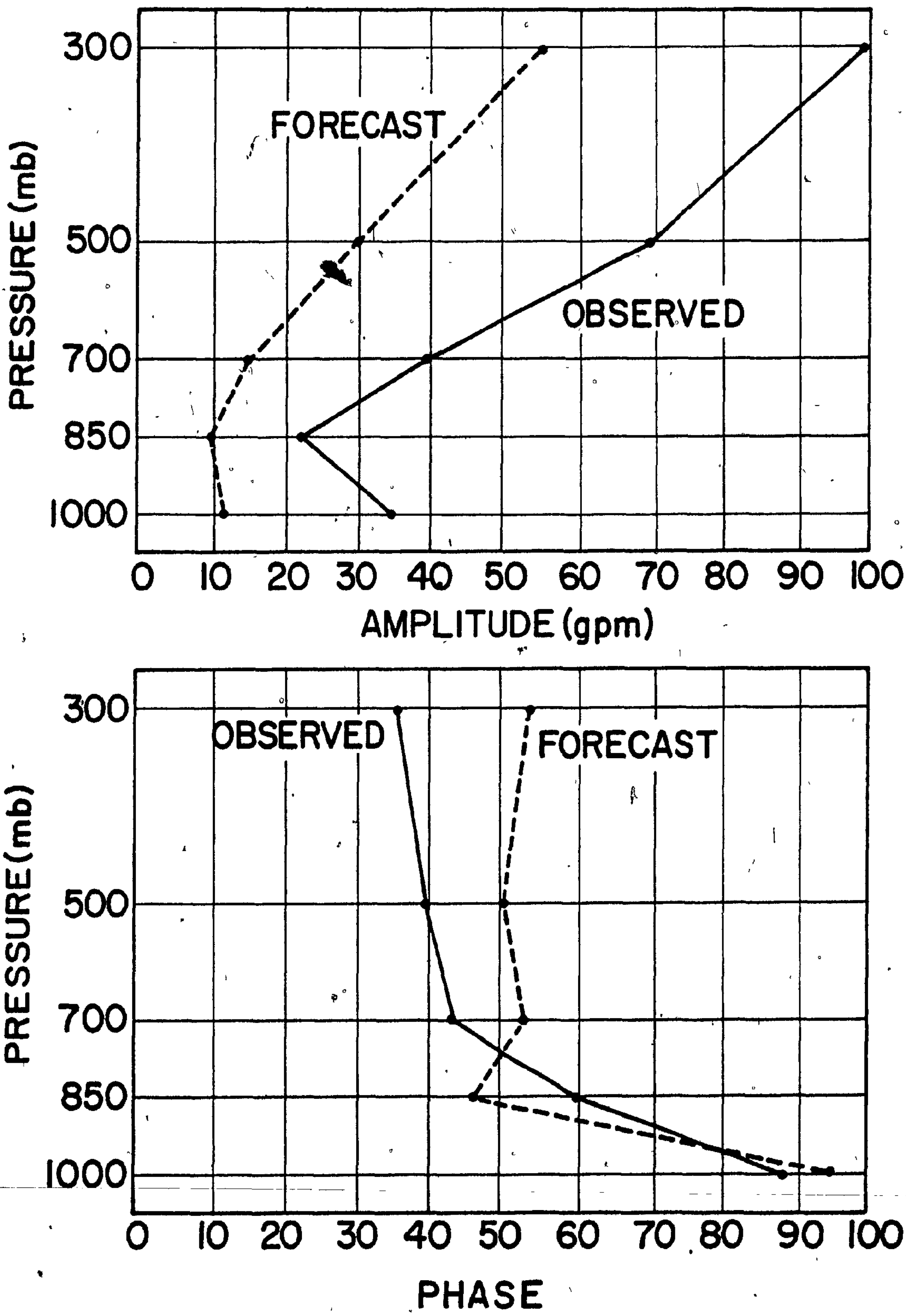

FIGURE (5.17) A comparison between the observed and forecast stationary components of spherical harmonic coefficient (2,4) of the height fields of Case 3.

decreases with time. This damping is larger than that which is caused by the model's time filter which can account for only a two percent decrease in amplitude in ten days.

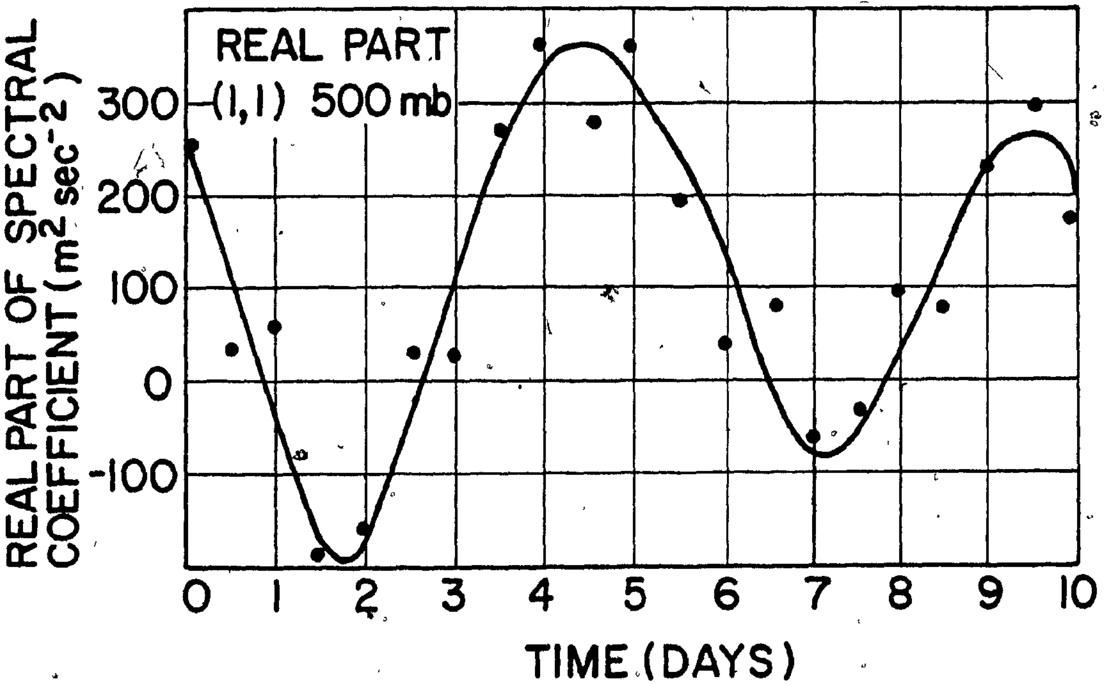

FIGURE (5.18). The behavior of the forecast transient component of spherical harmonic coefficient (1,1) of the 500 mb height field for Case 3.

5.7 Vertical Resolution and the Planetary Waves

A recent paper by Nakamura (1976) showed the effects of vertical resolution and the upper boundary on the stationary components of the planetary waves, using a model which utilized the quasi-geostrophic mid-latitude β -plane approximation and employed a dissipative layer near the upper boundary at 90 km. In the model, a long wave is forced by a given configuration of vertical velocity at the lower boundary. The vertical structure of the resulting wave was examined, using 356 equally spaced vertical levels from 1 km to 90 km. This high resolution solution was used as a control solution. Nakamura's experiments consisted of determining the steady state forced wave structures with various numbers and positions of the vertical levels and comparing the wave structure from the lower resolution models to that of the control solution. Figure (5.19) shows the control solution and a three level solution for a wave of 20,000 km length and 7,000 km width, using the mean winter zonal wind and temperature profiles. In general, the phases of the low resolution are fairly well reproduced by the low resolution model while the amplitudes are poor. The results for summer and spring and for various widths and lengths of the forced wave show that a low vertical resolution model cannot adequately reproduce the stationary components of the atmosphere (control solution). A similar investigation by Kirkwood (1976) showed the profound effect of the stratosphere wind structure on the stationary components of the planetary waves. In one experiment, with an eleven level low resolution model to simulate the structure of planetary waves with a mean summer wind profile, the uppermost computational level was located at 17 km, just below the region of easterly winds, which prevent the propagation of tropospheric planetary waves into the upper atmosphere (Charney and Drazin (1961)). The planetary waves were poorly modelled. However, when the wind profile was modified so that the uppermost level of the low resolution model was in the easterly winds, the waves were correctly reproduced.

To determine the effect of incorrectly modelled planetary wave stationary components on the error growth in atmospheric models, one can simply use the high resolution control solution as input data to a low resolution model. Since the low resolution model's stationary components are not the same as the high resolution model's stationary components, the low resolution model will produce spurious transient components which will cause an evolution from the initial state. The difference between the initial state and the low resolution model's state at any given time is the error resulting from erroneous stationary components.

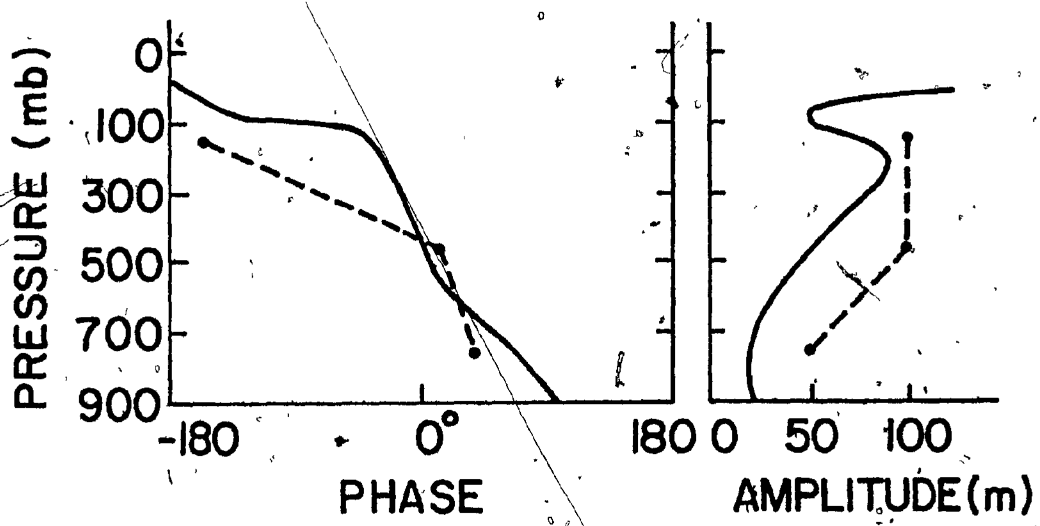

FIGURE (5.19) High resolution structure (solid lines) of a forced planetary wave compared to the low resolution structure (dashed lines). From Nakamura (1976).

Results of such experiments were also presented in Nakamura (1976) and in much more detail by Desmarais (1977). Figure (5.20) shows Nakamura's results for the control solution of Figure (5.19) applied to the three level model. It can be seen that, as the model evolves from the initial state to a state given by the low resolution model's stationary components, a damped external Rossby wave is produced with a period of about five days. His results also suggest that the short range forecast error is dominated by the external wave and that this mode becomes less important with time.

Desmarais' results for the 96 hour error in wavenumber one are given in Figure (5.21). In this case, a 101 level control solution is used as data for a six level low resolution model. It can be seen that the error structure is strikingly similar to that given in Figures (5.15) and (5.16).

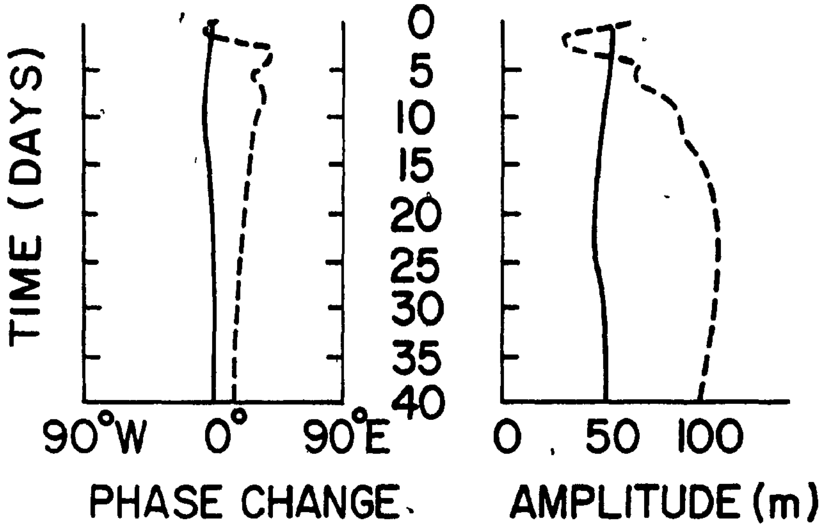

FIGURE (5.20) Evolution of a low resolution model (dashed lines) supplied with the steady state solution (solid lines) of the corresponding high vertical resolution or control model. From Nakamura (1976).

5.8 Seasonal Variation of the Planetary Wave Errors

To determine if there is any seasonal dependence on the magnitude of the external modes, the 36 hour error in the spherical harmonic coefficients (1,1), (2,2), and (3,3) of the 500 mb height field were plotted against the time of year. The results appear in Figure (5.22). In coefficient (1,1), there is a marked bi-modal distribution with maxima in February and August and minima in May and October. This bi-modal distribution is also present in coefficient (2,2) and less convincingly in coefficient (3,3). It must be remembered, as stated in Section (5.2), that the amplitudes of the external modes decrease with increasing wavenumber; and, as a result, the external modes contribute less to the errors in coefficient (3,3) than in (1,1).

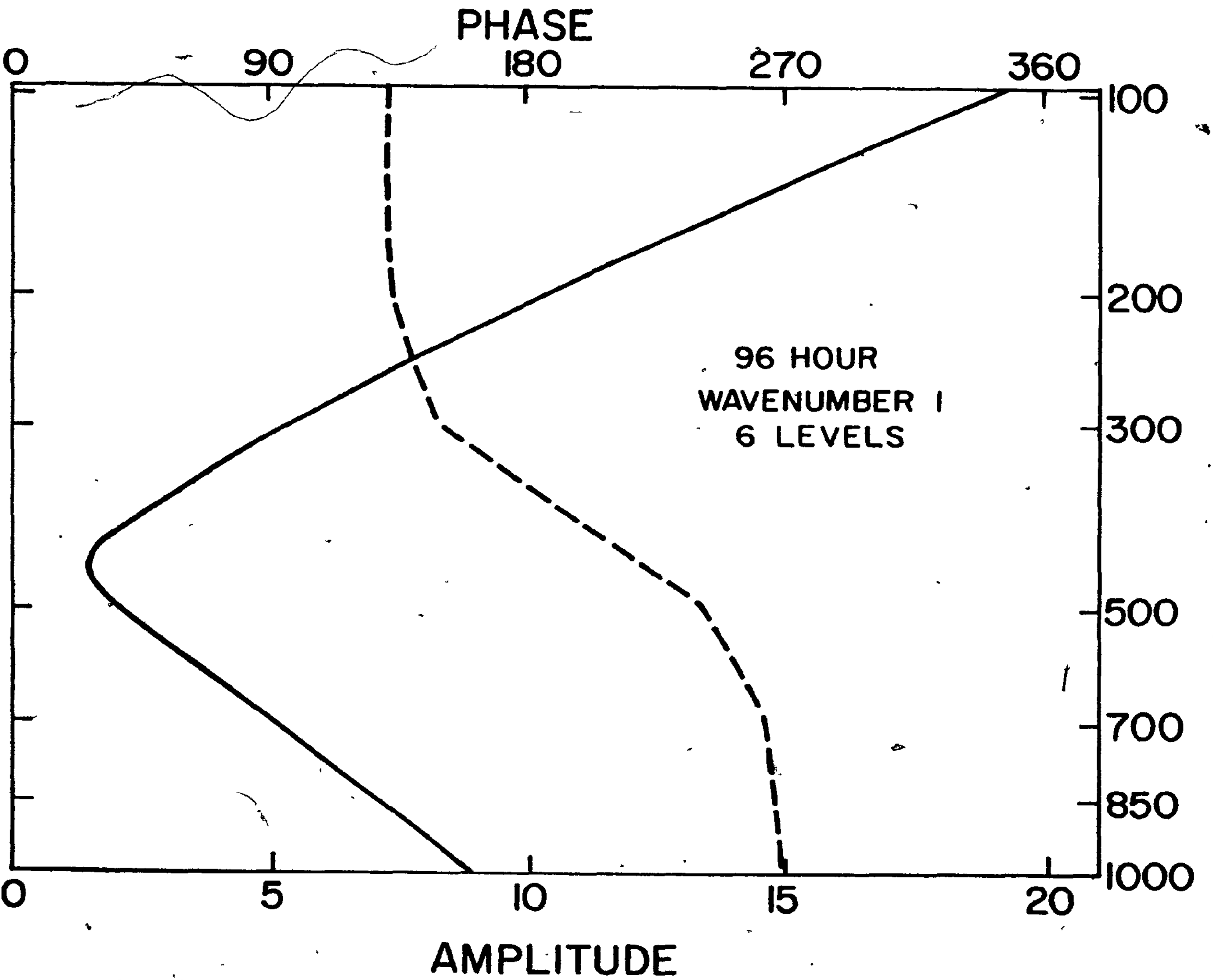

FIGURE (5.21) The 96 hour wavenumber one error structure from Desmarais' time-dependent vertical resolution experiments. The error amplitudes are in solid lines and the error phases in dash lines.

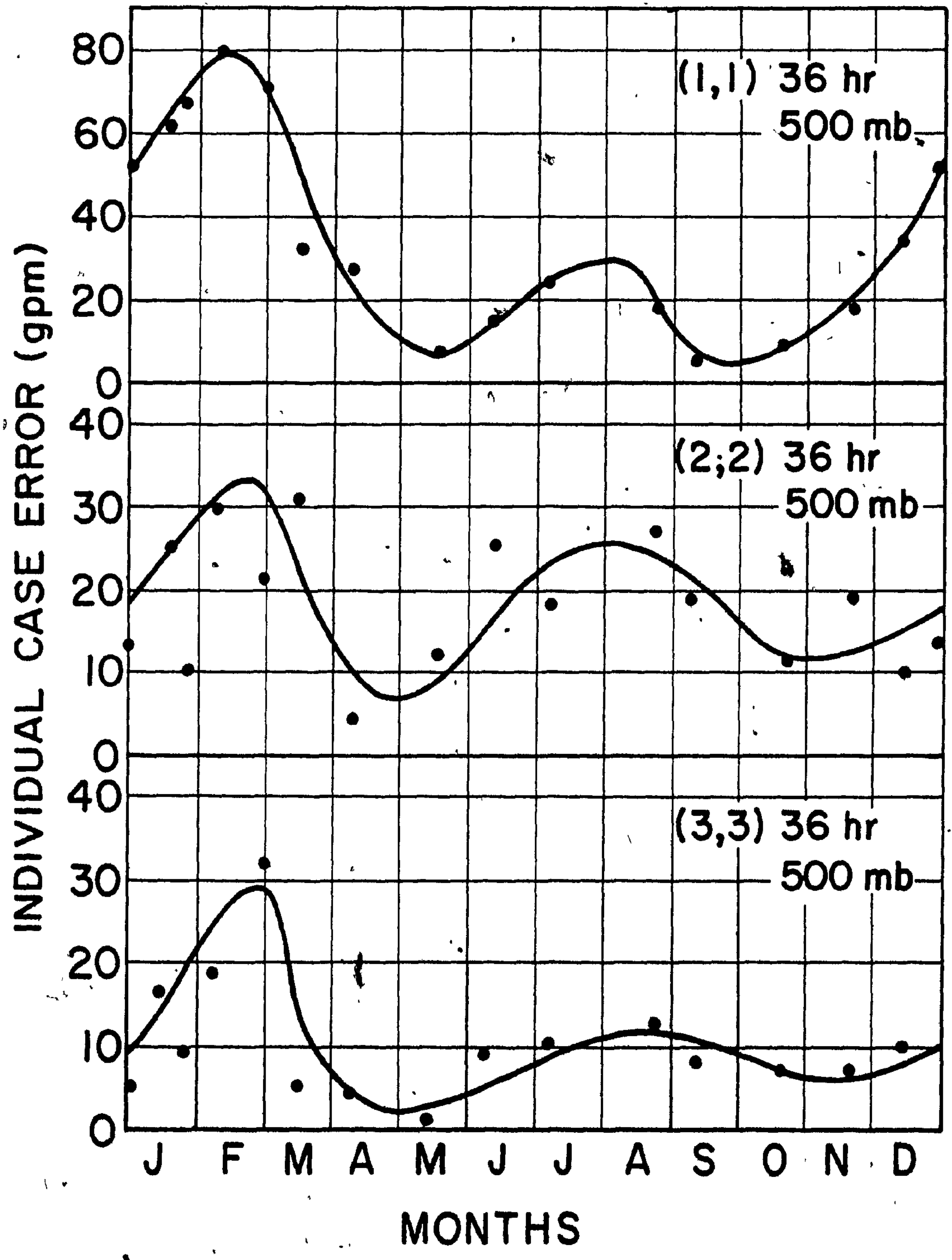

FIGURE (5.22) The seasonal dependence of the amplitudes of the 36 hour forecast error at 500 mb.

A possible explanation of the seasonal dependence of the external mode amplitudes is based on the model's pressure tendency equation

$$\frac{\partial q}{\partial t} = -\overline{D} - \overline{\vec{V}} \cdot \nabla q , \qquad (2.4)$$

where

$$\overline{(\ )} = \int_0^1 (\ )\, d\sigma .$$

The mean zonal wind regime of the stratosphere is strongly dependent on the seasons as shown in Figure (5.23) which gives the mean summer and winter profiles. In the model, the wind is decreased from the uppermost computational level to zero at $\sigma = 0$ which will result in a relatively small value of $\overline{\vec{V}}$. For the summer and winter profiles, it can be seen that large contributions to $\overline{\vec{V}}$ are present above the computational levels of the model. This will cause an error in the term $\overline{\vec{V}} \cdot \nabla q$ which will affect the surface pressure forecasts. Only in the spring and autumn, when relatively weak winds are present in the stratosphere, will the model's values of $\overline{\vec{V}}$ agree closely with the correct values of $\overline{\vec{V}}$. Hence, an external wave with a bi-modal distribution will result.

The error pattern for 96 hours shows no seasonal dependence. Since the model does not employ a radiative boundary condition or a "sponge layer", spurious reflections from the upper boundary, which affect the model's stationary components, are possible at any time of the year.

5.9 Conclusions

The most serious error in the present model is in the forecasts of the stationary components of the planetary waves. Vertical resolution studies showed the marked effect of vertical resolution on the stationary components of the planetary waves. The error pattern produced by a simple model, operating with incorrect stationary components resulting from insufficient vertical resolution, is almost identical to the error pattern produced by the spectral model used in this study. Hence, it is postulated that lack of vertical resolution and the upper boundary condition are responsible for large forecast errors in the planetary waves. This implies that the problem of planetary wave forecasts could be remedied by increasing the number of vertical levels in the model.

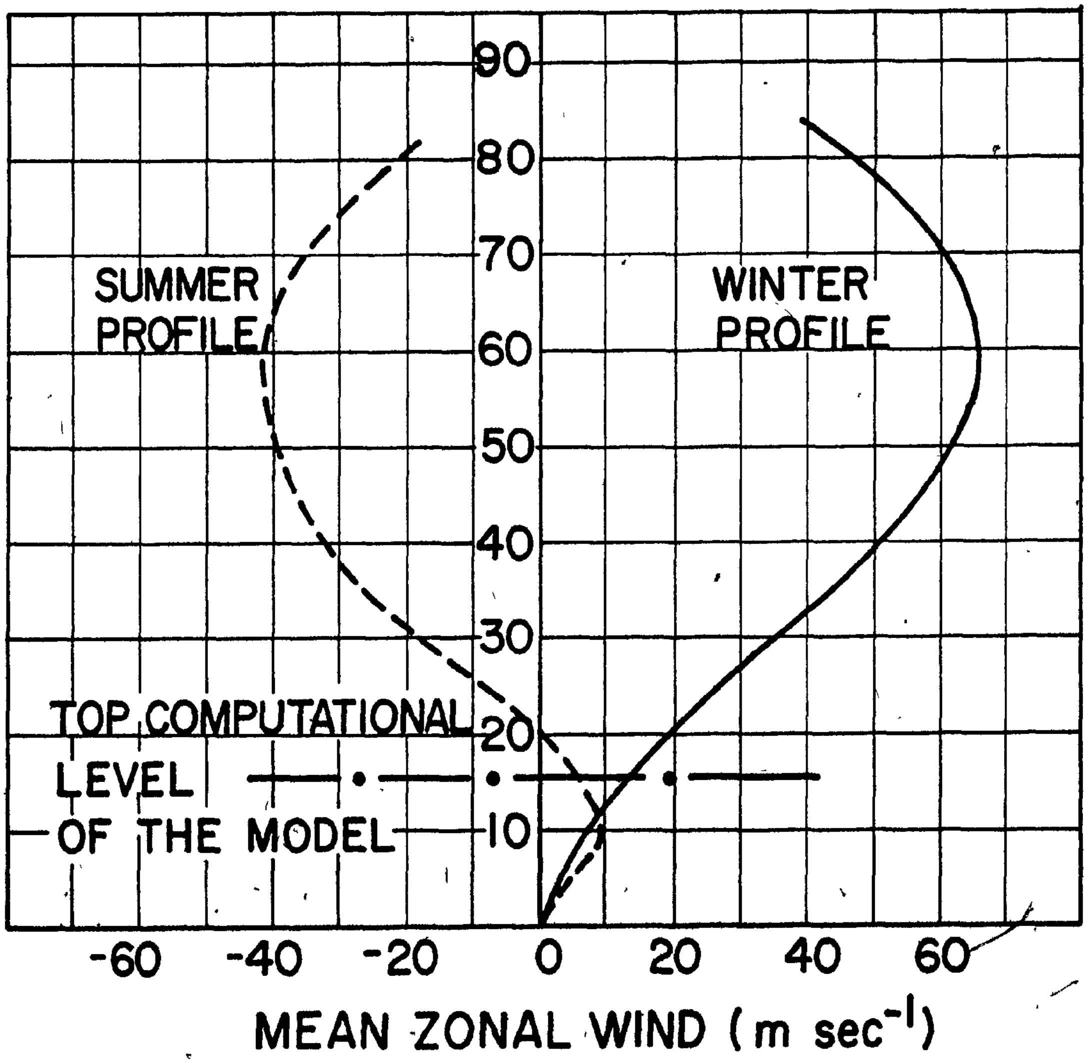

FIGURE (5.23) Mean summer and winter wind profiles with height. Heights are given in km.

Nakamura states that a resolution of one to two kilometers is required in the troposphere and two to three kilometers in the stratosphere. If this requirement is to be met, 40 to 50 vertical levels together with initial data are needed.

CHAPTER 6

SUMMARY AND CONCLUSIONS

6.1 Contributions to Knowledge

The original work, contained in this study, is first a full documentation of the planetary wave errors in an advanced numerical weather prediction model. Second is the identification of external gravity and Rossby modes as the major contributor to planetary wave error in short range (0-48 hours) forecasts. Third is a discussion of medium range forecast error and the hypothesis that it is due to an inadequate vertical structure and upper boundary condition.

6.2 Summary of the Error Character

It has been shown in this study that the planetary waves possess relatively large errors over the entire period of a 96 hour forecast. As demonstrated in Chapter 3, the errors are independent of the statistical method used in their computation, i.e. large errors exist in an absolute sense, in a relative sense, and in a comparison with persistence. The spectral model, used in this investigation, performs best in the range of wavenumbers from four to seven with decreasing performance at higher and lower wavenumbers.

The character of the error changes with time. In forecasts of short range, the error in the height field is dominated by three external modes (two gravity waves and one Rossby wave) which have a systematic nature. The error is monotonically increasing with height and has its largest contribution in the tropics and mid-latitudes. This error also has a marked seasonal dependence with maxima in the summer and winter and minima in the spring and fall.

For medium range forecasts (96 hours), the planetary wave error in the height field is internal in character. Even at this time length, the errors are noticeably systematic. The vertical structure of the error field, which is dependent on wavenumber, has a minimum at 700 to 500 mb and a maximum at 300 to 100 mb. The vertical structure of the phases shows that error field slopes westward with height below 300 mb and eastward with height above 300 mb. The meridional error distribution has a maximum amplitude in the polar regions with a weak northeast to southwest tilt of the phases.

The most serious short-coming of the model is the poor forecasts of the stationary components of the planetary waves. Generally, the phase structure of the wave is reasonably simulated but large errors in the amplitude structure are present. Studies by Nakamura (1976) and Kirkwood (1976) have shown that vertical resolution and structure have a profound effect on a model's ability to reproduce a planetary wave's stationary components.

The error growth produced, when atmospheric observations (having the correct stationary components) are used as data by a low resolution model having incorrect stationary components, can be studied using a simple model in the manner of Nakamura and Desmarais as outlined in Chapter 5. The great similarity between the error growth obtained by Desmarais, using a simple model, and that obtained by the author, using a complex model, suggests that the planetary wave errors in the Spectral Model are caused by inadequate vertical resolution and structure.

6.3 Suggestions for Further Work

The above hypothesis should be tested by incorporating a realistic stratosphere and mesosphere into numerical weather prediction models and by using a radiative upper boundary condition or dissipative layer to control spurious reflections from the upper boundary.

The need to improve the vertical structure of models raises the question of stratospheric data. At the present time, such data are relatively scarce and are not available for several hours after a given observation time. As a result, studies need to be undertaken to determine how much stratospheric data are necessary. For example, are observations a day or two old (or even climatology) sufficient? Will persistence in upper stratosphere and mesosphere greatly reduce the planetary wave error in the troposphere or must the high levels of the model be predicted?

The model's error statistics as a function of wavenumber should be extended to include all waves resolved by the model using a much larger sample.

The behavior of the model's stationary components should be studied in order to determine the climatology of the model.

BIBLIOGRAPHY

Charney, J. G. and A. Eliassen, 1949: A numerical method for predicting the perturbations of the middle latitude westerlies. Tellus, 1, 38-54.

__________ and P. G. Drazin, 1961: Propagation of planetary scale disturbances from the lower into the upper atmosphere. J. Geophys. Res., 66, 83-109.

Cressman, G. P., 1958: Barotropic divergence and very long atmospheric waves. Mon. Wea. Rev., 86, 293-297.

Daley, R., C. Girard, J. Henderson, and I. Simmonds, 1976: Short-term forecasting with a multi-level spectral primitive equation model - Part I - Model formulation. Atmosphere, 14, 98-115.

Deland, R. J. and K. W. Johnson, 1968: A statistical study of the vertical structure of travelling planetary-scale waves. Mon. Wea. Rev., 96, 12-22.

Desmarais, J.-G., 1977: Simulation Temporillè des Ondes Longues Atmosphériques. M.Sc. Thesis, Dept. of Meteor., McGill University, Montréal.

Eliasen, E., 1958: A study of the long atmospheric waves on the basis of zonal harmonic analysis. Tellus, 10, 206-215.

__________ and B. Machenhauer, 1965: A study of the fluctuations of the atmospheric planetary flow patterns represented by spherical harmonics. Tellus, 17, 220-238.

Ellsaesser, H. W., 1966: Evaluation of spectral versus grid methods of hemispheric numerical weather prediction. J. Appl. Meteor., 5, 246-262.

Haurwitz, B., 1940: The motion of atmospheric disturbances on a spherical earth. J. Marine Res., 3, 254-267.

Holton, J. R., 1975: The dynamic meteorology of the stratosphere and mesosphere. Meteorological Monographs, Vol. 15, No. 37, Amer. Meteor. Soc., 216 pp.

Kirkwood, E., 1976: Stationary Long Waves in a Bounded Pressure Co-ordinate Model. M.Sc. Thesis, Dept. of Meteor., McGill University, Montréal.

Leith, C. E., 1974: Spectral statistical-dynamical forecast experiments. Report Intern. Symp. on Spectral Methods in Numerical Weather Prediction, GARP Programme on Numerical Experimentation, Rep. No. 7.

Longuet-Higgins, M. S., 1968: The eigenfunctions of Laplace's tidal equations over a sphere. Phil. Trans. Roy. Soc. London, A262, 511-607.

Lorenz, E. N., 1969: The predictability of a flow which possesses many scales of motion. Tellus, 21, 289-307.

Madden, R. A., and P. A. Julian, 1972: Further evidence of global-scale five-day pressure waves. J. Atmos. Sci., 30, 935-940.

Martin, D. E., 1958: An investigation of systematic errors in the barotropic forecasts. Tellus, 10, 451-465.

Miyakoda, K., R. F. Strickler, C. J. Nappo, P. L. Baker, and G. D. Hembree, 1971: The effect of horizontal grid resolution in an atmospheric circulation model. J. Atmos. Sci., 28, 481-499.

__________, G. D. Hembree, R. F. Strickler and I. Shulman, 1972: Cumulative results of extended forecast experiments. I. Model performance for winter cases. Mon. Wea. Rev., 100, 836-855.

Nakamura, H., 1976: Some problems in reproducing planetary waves by numerical models of the atmosphere. J. Meteor. Soc. Japan, 54, 129-146.

Orszag, S. A., 1970: Transform method for calculation of vector coupled sums: application to the spectral form of the vorticity equation. J. Atmos. Sci., 27, 890-895.

Phillips, N. A., 1957: A coordinate system having some special advantages for numerical forecasting. J. Meteor., 14, 184-185.

Robert, A., 1966: The integration of a low order spectral form of the primitive meteorological equations. J. Meteor. Soc. Japan, 44, 237-245.

__________, J. Henderson and C. Turnbull, 1972: An implicit time integration scheme for baroclinic models of the atmosphere. Mon. Wea. Rev., 100, 329-335.

Smagorinsky, J., 1953: The dynamical influence of large-scale heat sources and sinks on the quasi-stationary mean motions of the atmosphere. Quart. J. Roy. Meteor. Soc., 79, 342-366.

__________, 1969: Problems and promises of deterministic extended range forecasting. Bull. Amer. Meteor. Soc., 50, 286-311.

Taylor, G. I., 1936: The oscillations of the atmosphere. Proc. Roy. Soc., A156, 318-326.

Wolff, P. M., 1958: The error in numerical forecasts due to retrogression of ultra-long waves. Mon. Wea. Rev., 86, 245-250.